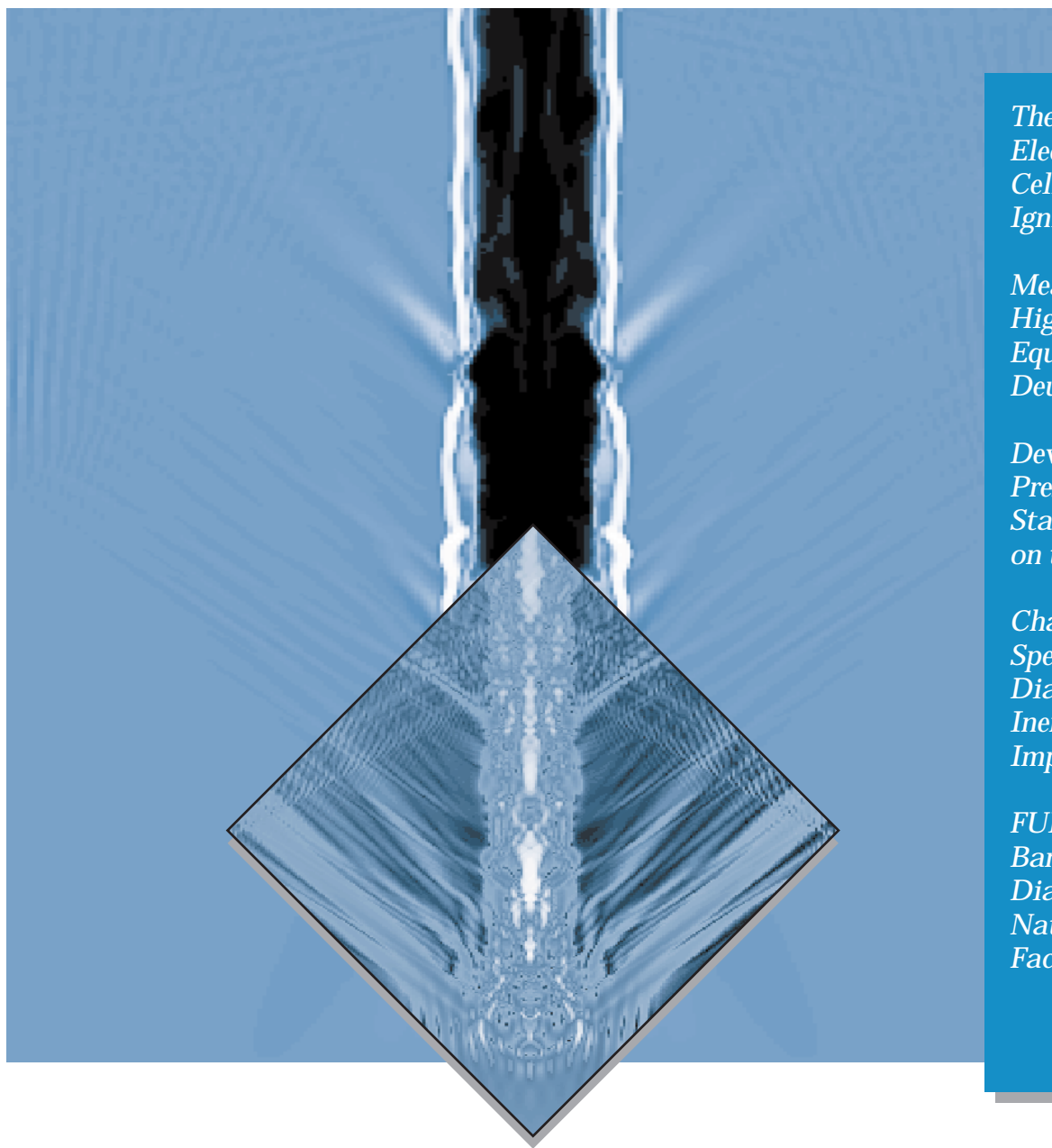


INERTIAL CONFINEMENT FUSION

Lawrence
Livermore
National
Laboratory

ICF Quarterly Report

April-June 1998, Volume 8, Number 3



*The Plasma
Electrode Pockels
Cell for the National
Ignition Facility*

*Measurements of the
High-Pressure
Equation of State of
Deuterium*

*Developing High-
Pressure, Solid-
State Experiments
on the Nova Laser*

*Charged-Particle
Spectroscopy: a New
Diagnostic for
Inertial Fusion
Implosions*

*FUDGE: a High-
Bandwidth Fusion
Diagnostic for the
National Ignition
Facility*

Propagation of Realistic Beams in Underdense Plasma

The Cover: In the fast ignitor concept, channeling of intense laser light through underdense plasma to the overdense regime is crucial. Prior to the ignition pulse, the channel is created by a hole-boring pulse. This hole-boring pulse is modeled using the F3D code. When a 30-ps, full-width-at-half-maximum, unaberrated, $f/3$ laser beam with 3 TW of input power is propagated through 400 μm of tenth-critical-density plasma, a channel forms, as shown in the image on the cover. The effect of the plasma on the beam is depicted in the diamond inset. Approximately 70% of the light is contained within the channel. The remainder of the beam is sprayed out of the channel by filamentation. For more details, see the article on p. 120.

On the Web:

<http://lasers.llnl.gov/lasers/pubs/icfq.html>

UCRL-LR-105821-98-3
April-June 1998

Printed in the United States of America
Available from
National Technical Information Service
U.S. Department of Commerce
5285 Port Royal Road
Springfield, Virginia 22161
Price codes: printed copy A03, microfiche A01.

This document was prepared as an account of work sponsored by an agency of the United States Government. Neither the United States Government nor the University of California nor any of their employees makes any warranty, express or implied, or assumes any legal liability or responsibility for the accuracy, completeness, or usefulness of any information, apparatus, product, or process disclosed, or represents that its use would not infringe privately owned rights. Reference herein to any specific commercial products, process, or service by trade name, trademark, manufacturer, or otherwise, does not necessarily constitute or imply its endorsement, recommendation, or favoring by the United States Government or the University of California. The views and opinions of authors expressed herein do not necessarily state or reflect those of the United States Government or the University of California and shall not be used for advertising or product endorsement purposes.

The ICF Quarterly Report is published four times each fiscal year by the Inertial Confinement Fusion/National Ignition Facility and High-Energy-Density Experimental Science (ICF/NIF/HEDES) Program at the Lawrence Livermore National Laboratory. The *ICF Quarterly Report* is also on the Web at <http://lasers.llnl.gov/lasers/pubs/icfq.html>. The journal summarizes selected current research achievements of the LLNL ICF/NIF/HEDES Program. The underlying theme for this program's research is defined within DOE's Defense Programs missions and goals. In support of these missions and goals, the ICF/NIF/HEDES Program advances research and technology development in major interrelated areas that include fusion target theory and design, target fabrication, target experiments, and laser and optical science and technology.

While in pursuit of its goal of demonstrating thermonuclear fusion ignition and energy gain in the laboratory, the ICF/NIF/HEDES Program provides research and development opportunities in fundamental high-energy-density physics and supports the necessary research base for the possible long-term application of inertial fusion energy for civilian power production. ICF technologies continue to have spin-off applications for additional government and industrial use. In addition to these topics, the *ICF Quarterly Report* covers non-ICF funded, but related, laser research and development and associated applications. We also provide a short summary of the quarterly activities within Nova laser operations, Beamlet laser operations, and the NIF laser design and construction.

LLNL's ICF/NIF/HEDES Program falls within DOE's national ICF Program, which includes the Nova and Beamlet (LLNL), OMEGA (University of Rochester Laboratory for Laser Energetics), Nike (Naval Research Laboratory), and Trident (Los Alamos National Laboratory) laser facilities. The Particle Beam Fusion Accelerator and Saturn pulsed-power facilities are at Sandia National Laboratories. General Atomics, Inc., develops and provides many of the targets for the above experimental facilities. Many of the *Quarterly Report* articles are coauthored with our colleagues from these other ICF institutions.

Questions and comments relating to the technical content of the journal should be addressed to the ICF/NIF/HEDES Program Office, Lawrence Livermore National Laboratory, P.O. Box 808, Livermore, CA, 94551.

Work performed under the auspices of the U.S. Department of Energy by Lawrence Livermore National Laboratory under Contract W-7405-Eng-48.

INERTIAL CONFINEMENT FUSION

ICF Quarterly Report

April–June 1998, Volume 8, Number 3

In this issue:

Foreword iii

The Plasma Electrode Pockels Cell for the National Ignition Facility (*M. A. Rhodes*) 89

The plasma electrode Pockels cell (PEPC) is one of the important enabling technologies that will make NIF possible. The PEPC, proven viable in a high-energy pulsed laser (Beamlet), has evolved from a plastic-housing, single-aperture device to a metal-housing, four-aperture module for NIF.

Measurements of the High-Pressure Equation of State of Deuterium (*P. M. Celliers*) 94

Using the Nova laser, we have compressed liquid deuterium samples by driving a strong shock wave in the sample. Using x-ray radiography and velocity interferometry, we have measured the shock velocity and the fluid velocity in the compressed material. The resulting data provides an experimental determination of the equation of state of dense hydrogen along the principal Hugoniot up to 300 GPa.

Developing High-Pressure, Solid-State Experiments on the Nova Laser (*D. H. Kalantar*) 101

An x-ray drive is being developed to shock-compress thin metal foils to megabar pressures in the solid state in order to study the effects of material strength at high compression. Details of experiments using Cu foils, stability theory, and the design for an experiment using Al foils are presented.

Charged-Particle Spectroscopy: a New Diagnostic for Inertial Fusion Implosions (*T. W. Phillips*) 109

A novel diagnostic technique for laser fusion implosions has been developed by a collaboration of LLNL, MIT, and University of Rochester scientists. This technique employs a permanent magnet spectrometer and permits the use of various detectors to measure the spectra of charged, energetic nuclear reaction products emitted during the fusion implosion. From these spectra properties of the fusion plasma (such as yield, fuel and ablator areal densities), ion temperature, and implosion asymmetry may be determined.

FUDGE: a High-Bandwidth Fusion Diagnostic for the National Ignition Facility (*M. J. Moran*) 116

This article provides a brief overview of issues associated with bang time, burn history measurements on the NIF. A technique is proposed to make these measurements based on Compton scattering initiated by the 16.7-MeV DT fusion gamma ray. Finally, a prototype instrument is described with particular emphasis on the system performance based on realistic assumptions for operations on the NIF.

Scientific Editor
Michael H. Key

Publication Editor
Jason Carpenter

Designer
Pamela Davis

Technical Editors
Cindy Cassady
Steve Greenberg
Robert Kirvel
Al Miguel

Classification Editor
Roy Johnson

Art Staff
Norm Calderon-Zablocki
Clayton Dahlen
Pamela Davis
Sandy Lynn
Kathy McCullough

Propagation of Realistic Beams in Underdense Plasma (*D. E. Hinkel*)**120**

The effect of beam structure on propagation through underdense plasma is examined in two different examples. First, it is shown that the distribution of intensities within a laser beam affects how the beam deflects in the presence of transverse flow, where the beam deflection rate scales linearly with intensity and plasma density and inversely with plasma temperature. Next, the effect of beam structure on channel formation by very intense laser beams is studied, and it is shown that a diffraction-limited beam with 3 TW of input power forms a channel through 400 μm of tenth-critical-density plasma, whereas when this beam is phase aberrated, channel formation does not occur.

Program Updates**A-1****Publications and Presentations****B-1**

FOREWORD

The construction of the National Ignition Facility (NIF) and preparations for its use are at present the dominant activities in LLNL's ICF/NIF Program. The work of the Nova laser will be completed and the facility shut down after a final six-month operation in FY 1999. The planning for ignition with NIF is being carried out on a national basis, and ongoing science and diagnostic development is being transferred elsewhere, notably to the Omega laser facility at the University of Rochester. This *Quarterly Report* reflects these trends by reporting scientific work at Nova and associated theory which is both of intrinsic interest and relevance to NIF. The report presents a key aspect of new laser technology developed for NIF and discusses design and testing at Omega of new ICF diagnostic instruments for NIF.

A key aspect of new laser technology, which is essential for the reduction of cost per unit of laser energy required to make the NIF an affordable project, is presented in "The Plasma Electrode Pockels Cell for the National Ignition Facility" on p. 89. The 40-cm-aperture plasma electrode Pockels cell (PEPC) developed for NIF has enabled the NIF beams to use high energy-extraction efficiency in a multipass amplifier by providing a means of switching the beam out of a recirculation cavity at full aperture. Conventional Pockels cells use a metal ring electrode to apply a field to the crystal and are limited to small apertures. In the PEPC, a uniform conducting plasma is formed over the surface of the crystal so the voltage can be applied uniformly over the aperture by a plasma electrode that is transparent to laser light and immune to laser damage. This electro-optical engineering project is typical of the advanced laser engineering that has enabled the construction of the NIF.

"Measurements of the High-Pressure Equation of State of Deuterium" on p. 94 presents scientific work that received the American Physical Society prize for Excellence in Plasma Physics in 1998. This study of the equation of state of shock-compressed liquid deuterium gives new insight into very basic dense-matter physics, showing an unexpectedly high compressibility in the region of one-megabar pressure; this challenges theoretical understanding and could be attributed to a change of state from molecular liquid to liquid metal. Elegant experimental measurements, based on radiography and Doppler interferometry, determine with high precision the velocity of the shock front and of the shock pusher in order to define the equation of state.

"Developing High-Pressure, Solid-State Experiments on the Nova Laser" on p. 101 reports a new line of study of the Rayleigh-Taylor (RT) instability in ablatively accelerated targets. At multi-megabar pressures, shocked matter is generally in the liquid state; with carefully shaped drive pulses in hohlraums, however, nearly isentropic compression can be achieved. Accelerated matter may therefore retain solid properties even with a high degree of compression. The strength of the solid then becomes a factor in the growth of the RT instability, which may be reduced to a lower level than for a liquid. Experiments with copper have tested the effect in a regime where detailed modeling shows it to be small. This work has pointed the way to future experiments with aluminum targets and with perturbations of shorter wavelength, where it is predicted to be significant.

The topic of development of new diagnostics is introduced in "Charged-Particle Spectroscopy: a New Diagnostic for Inertial Fusion Implosions" on p. 109. This article discusses a new device for charged-particle energy spectroscopy developed at Omega and suitable for the NIF. The goal is to study implosions using the charged particles from fusion reactions to give data on the yield, the areal density of both fuel and pusher, and the symmetry of implosions. A clever solution is presented using a combination of magnetic deflection and energy-proportional response of etched tracks in CR39 plastic (or charge collection on a CCD pixel) to uniquely identify protons, tritons, and alpha particles and measure their energy. Background signals from neutrons are a problem, but a solution giving good signal-to-noise ratio is found. Results from implosions at Omega demonstrate the success of the project.

“FUDGE: a High-Bandwidth Fusion Diagnostic for the National Ignition Facility” on p. 116 looks further into the future with a design for time-resolved measurement of the fusion burn rate at the NIF. This article shows why the established method for recording the rate of neutron emission fails at the NIF scale because of the larger spread of neutron time of flight. In its place, a novel method is proposed of time-resolving the flux of 16.7-MeV gamma rays, which are produced in a minor branch of the DT fusion reaction. In this scheme, Compton electrons are produced by the photons and magnetically analyzed to select those originating from the 16.7-MeV photons. Visible-light Cherenkov emission from the selected electrons is then detected with a fast channel plate to complete the measurement. Untried pending availability of large fusion yields at NIF, the new diagnostic promises to be an important source of information on fusion ignition at the NIF.

“Propagation of Realistic Beams in Underdense Plasma” on p. 120 shows how sophisticated analytic theory can give insight into a very complex aspect of laser–plasma interactions: the deflection of high-intensity laser light in a transversely flowing plasma. The light pressure (actually the ponderomotive pressure) creates channels in the plasma where there are local intensity maxima, and the laser light is self-focused towards the density minima of the channels; the channels are swept downstream by the flow, and the light is therefore refracted in the direction of flow. This academically interesting process is a practical problem in the gas-filled hohlraum targets to be used for ignition at the NIF. The analytical model gives insight into more detailed numerical simulations, which offer a solution to the beam deflection through beam smoothing by induced spatial incoherence.

Michael H. Key
Scientific Editor

THE PLASMA ELECTRODE POCKELS CELL FOR THE NATIONAL IGNITION FACILITY

M. A. Rhodes

P. Bilotft

C. Ollis

S. Fochs

Introduction

This article describes the design and prototype testing of a plasma electrode Pockels cell (PEPC) that will be used as part of an optical switch in the laser portion of the National Ignition Facility (NIF). To reduce costs and maximize performance, the laser architecture for NIF is based on a multipass power amplifier. A key component in this laser design is an optical switch that “closes” to trap the optical pulse in an amplifier cavity (for four gain passes) and then “opens,” letting the optical pulse escape. This switch includes a Pockels cell that provides voltage control of the laser beam’s polarization and a reflecting-transmitting polarizer. Such optical switches are common in many types of lasers, such as Q-switched and regenerative lasers.

The NIF’s 40- × 40-cm beam size, its square shape, and its 5-J/cm² energy density, however, require using an optical switch of unprecedented size. Conventional Pockels cells that are presently available commercially do not scale to such large apertures or to the square shape required for close packing. Our optical switch is based on a plasma electrode Pockels cell (PEPC) technology that has been proven on the Beamlet laser.¹ In FY98 we finalized a design for the NIF’s PEPC and validated it by testing prototypes.

The Plasma Electrode Pockels Cell Design

As has been done with a number of other NIF components, the PEPC is designed as a line replaceable unit (LRU)—the smallest subarray of apertures that will be installed or removed from a NIF beamline. The PEPC LRU is a 4 × 1 module (four apertures high by one aperture wide); an engineering model is shown in Figure 1.

Altogether, 48 of these modules, comprised of an operational core mounted in an L-shaped support frame, will be needed to provide optical switching for NIF’s 192 beamlines.

The operational part of the PEPC LRU has a midplane sandwiched between a pair of housings, with various other components attached to the housings. The midplane is a glass sheet with four apertures cut out from it. In each aperture, we have potted a 40- × 40- × 1-cm KDP crystal plate with a high-grade silicone rubber. The KDP crystals are electro-optic elements; voltage applied across them controls the PEPC’s switching action.

The housings are the main structural element of the PEPC, and their design is the key to its proper operation. A major design feature is to have all the vacuum and electrical interfaces at the top and bottom of the housings. This is critical for achieving the close inter-beam spacing required for economical laser construction. The housings are made from Al with a hard-anodized coating, which provides insulation to keep them from shorting out the plasma current. This construction technique is a major departure from the plastic housing used for Beamlet’s PEPC.

Other components in the operational core include anodes, cathodes, windows and window retainers, vacuum baffles, plumbing, gauges, and gas flow controllers. The windows are made of fused silica and rest on O-rings. During operation, because the interior of the PEPC is under vacuum, the windows are held in place by atmospheric pressure. However, when the vacuum system is off, the windows are held in place by retainer rings.

The plasma discharges that form the plasma electrodes are produced between sets of anodes and cathodes. These discharges span two full apertures. Each LRU has four cathodes (negative electrodes for the

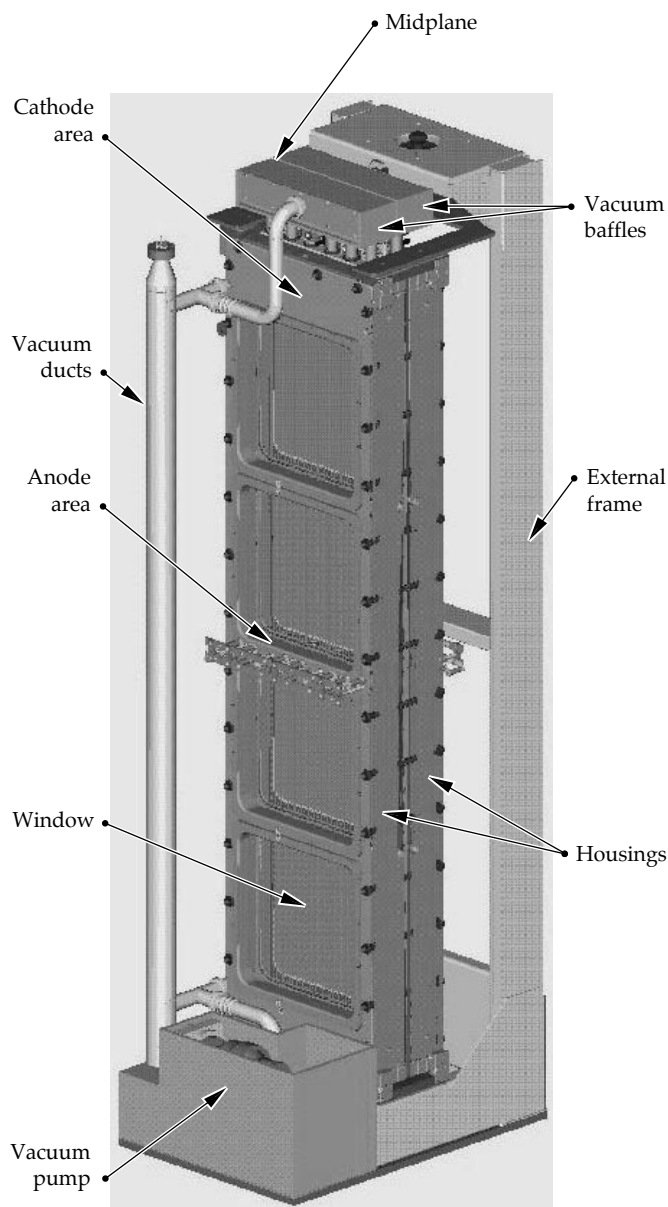


FIGURE 1. Engineering model of the PEPC module for NIF. (08-00-1198-2240pb01)

plasma discharge) mounted within recesses at the top and bottom of the housings. We use planar magnetron cathodes; one for each of the four plasma quadrants. High-field permanent magnets confine the plasmas near the cathode surfaces. This lowers the operating pressure and discharge voltage required and provides good discharge uniformity.

Because cathode sputtering is inevitable and we must control the sputtered material deposited onto optical surfaces, we use cathodes with graphite covers. This assures us that any sputtered material is carbon. Then, by using He mixed with 1% O as an operating gas, the sputtered carbon reacts with the oxygen to produce CO and CO₂. Both of these reaction products are

gases, so they are simply pumped away by the vacuum system.

Each discharge also uses a set of six positive electrodes (anodes). During development, we found that segmenting the anodes improved the discharge uniformity by helping to counteract the plasma's natural tendency to pinch. We assure that an equal fraction of the plasma current arrives at each of the anode segments by using appropriate ballast resistors.

The PEPC's vacuum and gas system provides the high-vacuum environment required for producing the plasmas. The vacuum system provides a base pressure of around 5×10^{-5} torr. The working gas is fed in with a feedback-controlled, mass-flow controller. The gas system is set up to maintain a constant operating pressure of 65 mtorr, rather than a constant flow.

The entire PEPC LRU is pumped by a turbomolecular-drag pump, which is backed by a suitable roughing pump. The interior of the housing is pumped through holes in the cathodes. These holes lead to pump-out tubes that penetrate the housing ends and connect to an insulated vacuum baffle, which provides electrical isolation between the two housings when the 17-kV switch-pulses are applied. The baffle prevents plasma electrons from flowing to the grounded vacuum structure during the switching pulses, while still allowing a high vacuum conductance.

Each LRU is driven by a set of pulse generators. Four plasma pulse generators (PPGs) and two switch pulse generators (SPGs) are used, which are not really part of the LRU. In NIF, they will be installed near the LRUs and connected to them by appropriate cables. Each PPG delivers a 1.2-kA current pulse through a plasma channel. Some current is also supplied to conductors that run along the sides of the housing. The current in these conductors produces a magnetic field that helps attract the plasma to the edges of the crystals. The switch pulsers supply a nearly rectangular-shaped, 17-kV, high-voltage pulse across the midplane. The highly conductive plasmas assure that this voltage is uniformly applied across the entire crystal surface.

The external support for mounting the operational portion of the PEPC LRU is an "L" shaped frame. A kinematic mounting system is also attached to this frame. The other side of these mounts will be attached to the NIF periscope structure. At the bottom of the support frame is an interface plate, through which pass all the electrical, gas, cooling, vacuum, diagnostic, and control interfaces.

Prototype Testing and Validation of the NIF PEPC Design

To test and validate our design, we built two prototypes—a "mechanical" prototype (Figure 2) and an "operational" prototype² (Figure 3). In this way, we



FIGURE 2. The “mechanical” prototype of the NIF PEPC; used to test the external frame design and the kinematic mounts. (08-00-1198-2241pb01)



FIGURE 3. The “operational” prototype of the NIF PEPC; used to verify full electro-optic operation. (08-00-1198-2242pb01)

were able to test the external frame and operational core designs independently and simultaneously.

The mechanical prototype consists of a pair of real PEPC housings with a “dummy” midplane (no KDP) and “dummy” windows (Al and acrylic). The frame is the actual NIF design, as are the kinematic mounts. A vacuum system was included, but no gas system (as of this writing). We used the mechanical prototype for vibration testing and to test other mechanical aspects of the LRU, including its handling, kinematic repeatability, and interfaces.

The mounting repeatability results are excellent. The performance requirement is to reproducibly place the LRU to within ± 1 mm. Measurements show that the LRU locates itself to within ± 0.025 mm, forty times better than required.

The operational prototype uses a full set of NIF PEPC optics, including eight fused-silica windows and four rapid-growth³ KDP crystals. These elements will have antireflection (AR) coatings in NIF, but the prototype does not. We know from our Beamlet PEPC experience that the switching performance is not affected by AR-coated optics.

There is no external frame in the operational prototype and, because we do not have sufficient vertical clearance to test it in the vertical NIF orientation, we have to position the assembled housing horizontally. Nevertheless, the prototype allows us to test the actual electro-optic switching operation of the 4×1 PEPC.

The 4×1 PEPC was evaluated with the apparatus shown schematically in Figure 4. The output coupler of a 10-ns pulsed 1.064- μm laser is relay-imaged with a beam-expanding telescope to the plane of the KDP crystals. The beam is shaped into a square cross section and is also passed through a polarizer to ensure that the PEPC is exposed to linearly polarized light.

We use a system of beam splitters (not shown) to produce four identical full-aperture beams. After passing

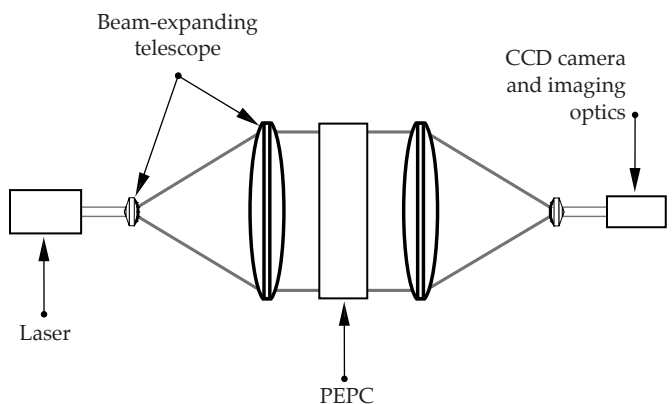


FIGURE 4. A schematic diagram of the optical system used to evaluate the operational prototype. This system allows all four apertures to be simultaneously tested. (08-00-1198-2243pb01)

through the cell and an analyzing polarizer, the four beams are each relay-imaged to a CCD camera. We determined the PEPC's performance by measuring the extinction ratio (ER). We did this by comparing the CCD image with and without the PEPC operating. The NIF requirements are that the average ER for each aperture must be greater than 100, while the worst spot can have an ER no lower than 50.

When the ER is 100, 99% of the light is in the proper polarization; an ER of 50 corresponds to having 98% of the light correctly polarized. Put another way, if the ER is 50 on some part of the aperture, a 2% amplitude modulation is introduced into the beam.

In NIF, shaped optical pulses of up to 20 ns in duration pass through the PEPC four times on a normal shot. The temporal relationship among these four passes and the switch-pulse is shown in Figure 5.

To fully validate the operation, we must measure the performance at each of the four times. Pass One occurs before the switch-pulse starts and the ER averages more than 1000 for each aperture. The minimum ER for each aperture is about 200, easily meeting the NIF requirement. The results for Pass Three are shown in Figure 6. Here, the PEPC is rotating the beam polarization by 90°. This corresponds to a cavity-closed condition. The average and minimum ERs all easily meet the NIF requirements. The data for Pass-Two timing are indistinguishable from the Pass-Three results. In fact, we have to advance the optical pulse more than 160 ns before we notice a significant reduction in the ER. Finally, the results for Pass Four, or the switch-out

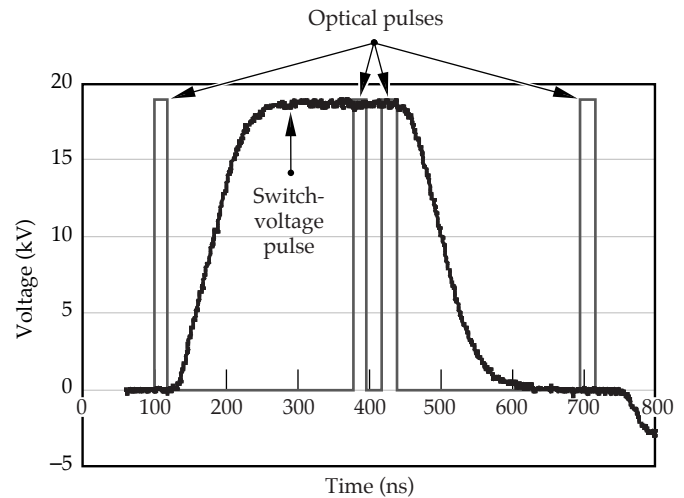
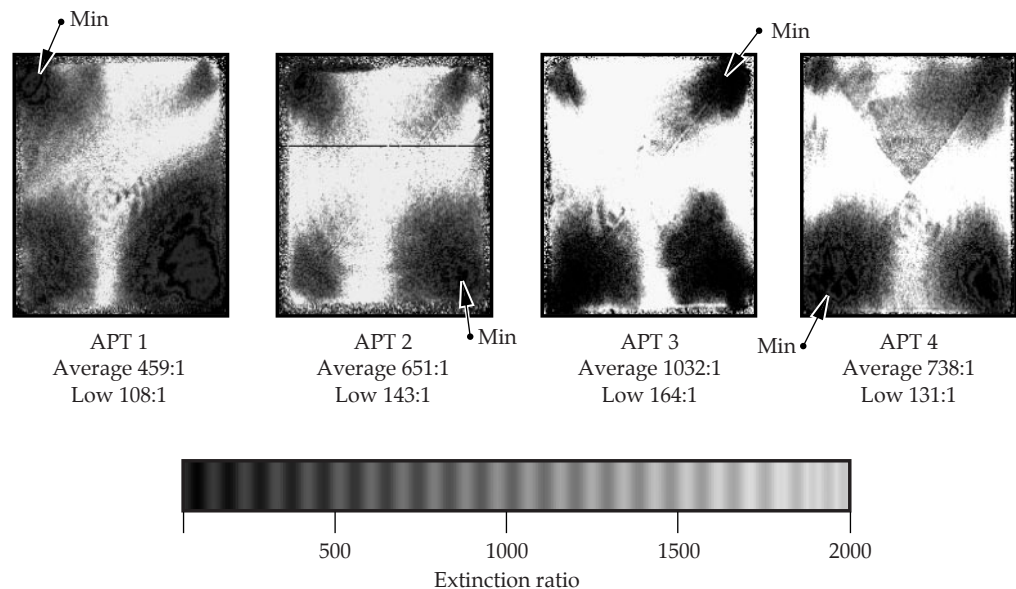


FIGURE 5. Diagram showing the temporal relationship between the voltage pulse applied to the PEPC and the four-times-per-NIF-shot optical pulse that traverses the PEPC. (08-00-1198-2244pb01)

timing, are shown in Figure 7. Again, the average and minimum ERs easily meet the NIF requirement.

These results are not isolated "best results" data. The PEPC system fires every four seconds in the lab and the shot-to-shot results are very reproducible. We have taken series of 100 shots and found the ER variation to be less than 10%. After prolonged use (over 20 minutes of continuous firing), we see a slight degradation in the ER due to the heating up of the KDP crystals from the discharges.

FIGURE 6. Optical data for Pass-Three timing after the voltage pulse has been applied to the cell; the amplifier cavity is "closed." The Pass-Three ERs for all four apertures (APT 1, 2, 3, 4) are much better than the NIF requirements. (08-00-1198-2245pb01)



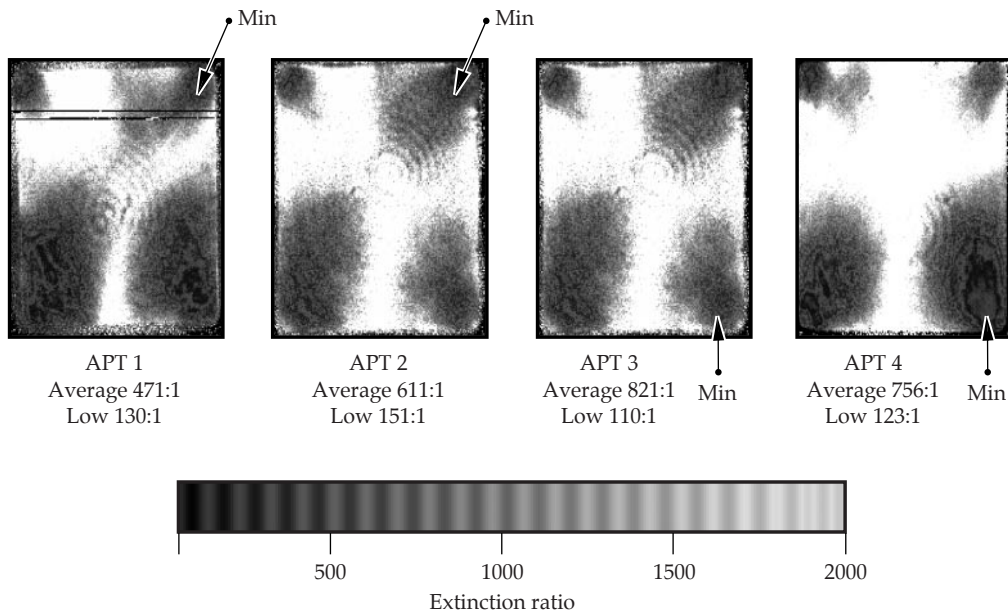


FIGURE 7. Optical data for Pass-Four timing after the voltage pulse to the cell has ended; the amplifier cavity at this time will be “open.” The high-energy laser pulse will now be switched out of the amplifier cavity. The Pass-Four ERs for all four apertures (APT 1, 2, 3, 4) are much better than the NIF requirements. (08-00-1198-2246pb01)

Conclusion

We have designed a four-aperture plasma electrode Pockels cell for use in the NIF. This device is the active part of a successful optical switch for a multipass laser amplifier design. We have proven the optical performance of our design by building and operating a full-size operational prototype. Furthermore, the mechanical aspects of our design have been simultaneously proven with a mechanical prototype containing no active optical elements. Both the optical performance and the kinematic mounting system for locating the entire structure meet or exceed the NIF requirements by wide margins.

Notes and References

1. M. A. Rhodes, B. Woods, J. J. De Yoreo, D. Roberts, and L. J. Atherton, *Appl. Op.* **34**, 5312–5325 (1995).
2. M. A. Rhodes, S. Fochs, and C. D. Boley, “Plasma Pockels Cell Based Optical Switch for the National Ignition Facility,” *International Conference on Plasma Science*, San Diego, CA, May 19–22, 1997.
3. N. P. Zaitseva, J. J. De Yoreo, M. R. Dehaven, R. L. Vital, K. E. Montgomery, M. Richardson, and L. J. Atherton, *J. Cryst. Growth* **180**, 255 (1997).

MEASUREMENTS OF THE HIGH-PRESSURE EQUATION OF STATE OF DEUTERIUM

<i>P. M. Celliers</i>	<i>G. W. Collins</i>	<i>A. Ng*</i>
<i>K. S. Budil</i>	<i>L. B. Da Silva</i>	<i>R. J. Wallace</i>
<i>R. Cauble</i>	<i>M. E. Foord</i>	<i>S. V. Weber</i>
	<i>D. M. Gold</i>	

Introduction

Hydrogen is the simplest and most abundant element in the universe, yet at high pressure, it is one of the most difficult to understand. Having only a single electron, it shows characteristics of both the Group I alkalis and the Group VII halogens.¹ At low pressure, hydrogen isotopes are halogenous, covalent, diatomic molecules that form insulators. With increasing pressure, the isotopes transform into alkali metals. Whereas most theories predict <300 GPa for the insulator-metal transition pressure along the 0-K isotherm,² static experiments at even higher pressures have not shown evidence of metallization.³ Evidence of high conductivity was observed at an unexpectedly low pressure (140 GPa) at finite temperature (3000 K) where the isotope is in a molecular fluid phase.⁴ There is no accepted theoretical description of the transformation of hydrogen from an insulator into a conducting atomic fluid at high pressures and high temperatures. This regime of high density and extreme pressure is fundamentally difficult to address theoretically. It is a dynamic, strongly correlated, partially degenerate composite of H_2 , H , H^+ , and electrons as well as other components, such as H_3 , where no simple approximation is available.

Accurate knowledge of the thermodynamic properties of dense fluid hydrogen isotopes is required for demonstrating inertial confinement fusion (ICF) in the laboratory.⁵ In the initial stages of an ICF implosion, a layer of deuterium-tritium (DT) fuel is compressed and accelerated through a sequence of progressively stronger shocks with amplitudes from around 80 to

5000 GPa (0.8 to 50 Mbar). Design of this hydrodynamic process critically depends on the high-pressure equation of state (EOS) of the DT fuel. Figure 1a shows a diagram of the principal Hugoniot⁶ calculated from an established and widely used theoretical model (SESAME)⁷ and the Hugoniot prediction from a more recent theory by Ross.^{8,9} The more recent theory predicts a substantially higher density for shock amplitudes around 100 GPa. Fuel compression and acceleration begins with a single shock around 80 GPa. Subsequent shocks compress and accelerate the fuel further beginning from thermodynamic states originating along the single shock compression curve, i.e., the principal Hugoniot. The initial 80-GPa shock amplitude is situated in the region of greatest theoretical uncertainty in our understanding of the hydrogen EOS. This uncertainty produces practical consequences for ICF capsule design. For example, the additional compression around 100 GPa predicted with the recent Ross theoretical model influences the subsequent compression history of the fuel layer enough to lead to significantly different (higher) predictions of the capsule yield. Thus, accurate knowledge of the EOS of hydrogen is of considerable practical importance for ICF.

Evaluation of the competing theoretical models requires new experimental data along the principal Hugoniot into the few-100-GPa regime. In addition to the ICF application, the metallic transition and its effects on the EOS at pressures near 100 GPa are integral to models of many hydrogen-bearing astrophysical objects,¹⁰ including Jovian planets,¹¹ extrasolar giant planets,¹² brown dwarfs,^{13,14} and low-mass stars.¹⁵ Figure 1b shows the phase space of hydrogen¹⁶ in the vicinity of the finite-temperature, insulator-metal transition; its location relative to the principal shock Hugoniot; and the compression isentropes of Jupiter and Saturn. This region of phase space is experimentally accessible

*Department of Physics and Astronomy, University of British Columbia, Vancouver, Canada

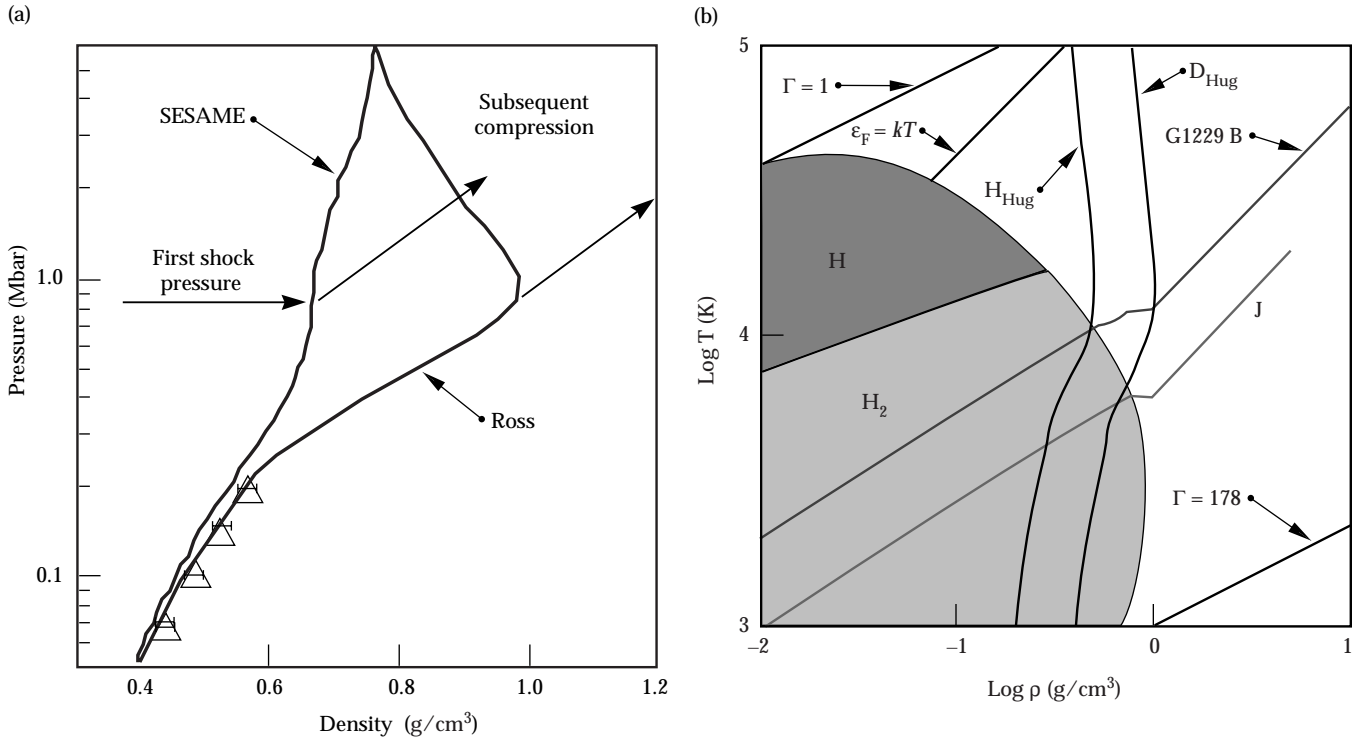


FIGURE 1. (a) Theoretical shock Hugoniot curves and initial paths for subsequent compression. The large, principal Hugoniot compression predicted by Ross implies that the fuel layer is compressed 50% more than that obtained from earlier models. The triangular points represent shock data from gas-gun experiments carried out in the 1980s. (b) Model phase diagram of hydrogen¹⁶ in the regime of the fluid-metal-insulator phase transition. $\Gamma = e^2(4\pi/3n)^{1/3}/kT$ is a measure of the interparticle correlation strength, where n is the particle density; a value of $\Gamma > 1$ signifies strong coupling between the fluid constituents and a commensurate lack of simplifying assumptions that enable theoretical calculations. The Fermi energy is ϵ_F ; for temperatures $kT < \epsilon_F$, matter is partially degenerate. The regions identified as H_2 and H are mainly molecular and atomic hydrogen respectively; outside these regions, hydrogen is primarily an ionized fluid. “J” is a model isentrope for Jupiter; “G1229 B” is an isentrope for brown dwarf G1229 B.¹⁴ “ H_{Hug} ” and “ D_{Hug} ” are model hydrogen and deuterium Hugoniot.^{6,9} (50-00-1198-2192pb01)

from the principal shock Hugoniot, but meaningful measurements along the Hugoniot in this regime have, until recently, been unattainable due to lack of a sufficiently powerful shock driver. Using the Nova laser at Lawrence Livermore National Laboratory, we have accessed this regime by shocking liquid D_2 to pressures at and above the metallic transition, where we measured the thermodynamic properties of the shocked state.

At high pressures, both molecular dissociation and ionization can be activated through high-density as well as thermal effects. Early EOS models either did not include these effects or predicted that their consequences for the EOS would be small.^{7,17} More recent theories predict that significant modifications to the EOS can occur either through a continuous dissociative transition^{8,9} or a first-order phase transition^{18–20} from the molecular to the metallic phase. In view of this theoretical situation, reliable experimental data have become valuable as a guide to theory. Shock-wave experiments using light gas guns have produced Hugoniot data on D_2 (initial density $\rho_0 = 0.17 \text{ g/cm}^3$) up to 23 GPa ($\rho = 0.58 \text{ g/cm}^3$ and $T = 0.39 \text{ eV}$), below

the transition.^{8,21} Recently, radiographic measurements were made on the Hugoniot of liquid deuterium near 100 GPa employing a strong shock driven by an intense laser beam.²² The few data indicated that the shock density of the isotopes at 100 GPa was much greater than had been predicted by established EOS theories.^{7,17} The reason was attributed to the effects of high-density-produced molecular dissociation.²²

Here, we report further measurements on the deuterium EOS, which extend the earlier compression data. In addition to our principal x-radiographic diagnostic, we have measured shock velocity and shock-front reflectivity with an optical probe, and thereby have obtained independent measurements of the shock trajectories. The new data set, obtained with two independent diagnostics, is internally self-consistent and corroborates the earlier data. We have also observed high optical reflectivities, characteristic of metallic conduction. This observation further corroborates the recent model predictions that the high compressibility is accompanied by transformation of the fluid into a conducting state.

Laser-Driven Shock Experiment

We used the Nova laser²³ to shock liquid deuterium to pressures between 22 and 340 GPa, which is a wider range of pressure than that in earlier experiments. In addition, we verified that this range spans the metal–insulator phase boundary. For each experiment, the shock wave pressure P and density ρ were determined from measurements of the shock speed U_s and the particle velocity behind the shock U_p using the Hugoniot relations $P = \rho_0 U_s U_p$ and $\rho = \rho_0 U_s / (U_s - U_p)$. Liquid D_2 at 20 K was contained in a 1.5- or 1.0-mm-diam, 0.45-mm-long cylindrical cell machined into a Cu block, as shown in Figure 2. One end of the cell was sealed with an Al or Be disk that acted as a pusher; the outside of each pusher was coated with 20 μm of either a polystyrene or Be ablator. The pushers were 180 to 250 mm thick with an rms surface roughness of 30 nm for Al and 90 nm for Be. X-ray-transmitting windows consisting of 5- μm -thick Be foils allowed us to perform radiography transverse to the shock direction through the sides of the cell. We also viewed the sample from behind through a 0.5-mm-thick sapphire window. A spatially smoothed Nova laser beam ($\lambda_L = 527 \text{ nm}$) with an intensity of 10^{13} to $3 \times 10^{14} \text{ W/cm}^2$ irradiated the ablator for 5 to 10 ns. The ablator served to minimize production of high-energy x rays in the laser plasma. Several laser-spot-size configurations were used over the course of the shots, from a $400 \times 600\text{-}\mu\text{m}$ elliptical spot to a 1-mm-diam

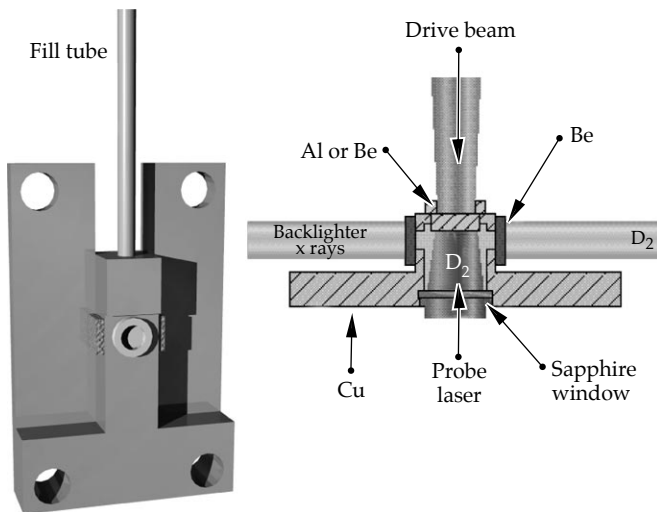


FIGURE 2. Sketch of the cryogenic cell used to contain the sample for the experiment. X-ray-transparent beryllium windows on the sides allowed for side-on x-ray shadowgraphic probing of the shock front. A probe beam transmitted through the rear sapphire window allowed for optical probing of the shock front. (50-00-1198-2193pb01)

circular footprint. The rapidly heated ablator drove a shock wave into the metal pusher. Ideally, when the shock wave reached the rear of the pusher, the pusher– D_2 interface released into the D_2 at the speed U_p while the shock wave propagated ahead at the speed U_s .

X-Ray Radiography

Using transverse radiography, we tracked the positions of the shock front and the pusher– D_2 interface as a function of time to obtain measurements of U_s and U_p for each experiment. The radiography source was a laser-heated Fe foil located 12 cm from the cell. X rays from the Fe backlighter passed through the cell and into a Kirkpatrick–Baez microscope (bandpass of $800 \pm 50 \text{ eV}$) and then into a streak camera. The streak camera slit subtended a strip 300 μm long by 5 μm wide at the target. The slit image was magnified 82 times with a spatial resolution of 3 μm at the object plane. 2D hydrodynamic simulations showed that edge rarefactions would attenuate the shock wave around its periphery. However, the simulations indicated that the shock wave would remain spatially uniform and temporally steady in the center of the shock wave for sufficient time to obtain accurate data.

The earlier experiments used only Al pushers to obtain a maximum pressure of 210 GPa (Ref. 22). Here, we extended the measurements to higher pressure using Be pushers, which have a lower density than Al. The significance of higher pressure is that on the Hugoniot above the metal–insulator transition regime, the compression must eventually approach a value of four.⁶ Failure to exhibit this effect would call the experimental methodology into question. Because Be is relatively transparent to keV-energy x rays produced in the laser plasma (and thus more likely to allow preheating of the D_2 sample), we inserted an x-ray-blocking layer of 1- μm -thick Au between the ablator and pusher. The Au did prevent preheating of the D_2 , but it also caused shock-wave reverberations in the pusher that were not completely damped by the time the shock wave released into the D_2 . The higher-pressure shock waves achieved using Be exhibited more temporal variation immediately after release than those produced with Al, resulting in larger uncertainties in measurements of U_s and U_p .

Figure 3 shows a streak radiograph of shock-compressed D_2 with a Be pusher. The pusher is opaque to backlighter x rays, so the interface is the boundary between the light and dark regions. At $t = 0$, the shock wave crosses the interface, and the interface surface begins to move. By 3 ns, the interface is moving at the final speed U_p . Grazing incidence refraction of the backlighter at the density jump across the shock front

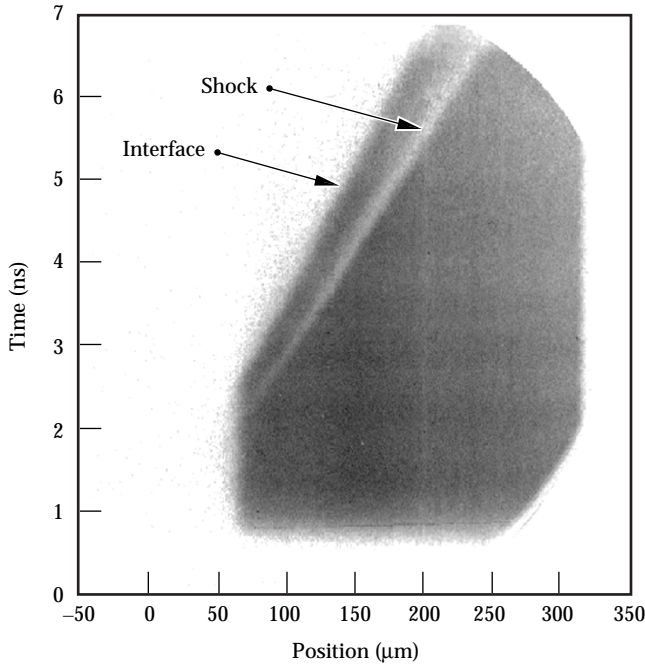


FIGURE 3. Transverse streak transmission radiograph of a D_2 EOS target with a Be pusher at a laser intensity of $7.6 \times 10^{13} \text{ W/cm}^2$. Shock release into the D_2 is at $t = 0$. The image shows a shock decelerating until $t = 3 \text{ ns}$, at which time it becomes steady where the slopes of the interface and shock are U_p and U_s , respectively. (50-00-1198-2194pb01)

occurs at angles larger than the acceptance angle of the microscope, so that the shock front is visible as a dark line propagating ahead of the interface. The slope of this line is U_s . Absolute uncertainties in U_s and U_p were determined from uncertainties in sweep speed (0.3%), magnification (0.5%), and point selection and deviation of the trajectories from linearity (1%).

Velocity Interferometry

The sapphire window at the back of the cell admitted a probe laser. In the original experiments,²² the probe was used in a Michelson interferometer configuration, imaging the rear of the pusher through the unshocked D_2 . The interferometer monitored the surface position for evidence of radiative heating of the target. The demonstrated lack of sample preheat allowed us to use laser-driven shock waves for EOS measurements.²⁴

For these experiments, the probe laser ($\lambda_p = 1.064 \mu\text{m}$) was used for velocity interferometry, a technique that measures the Doppler shift of light reflected from a moving surface.^{25,26} This kind of experimental arrangement is a standard tool available at many shock research facilities and is known as a velocity interferometer system for any reflector (VISAR). The reflected beam was imaged

onto the slit of a streak camera after passing it through the interferometer. The recorded fringe shift is directly proportional to the Doppler shift and, therefore, to the velocity of the reflecting surface. Figure 4a shows an example recording of a streaked interferogram from our VISAR system. This particular experiment intentionally produced a decaying shock that decelerated as it propagated. For negative times on the scale in Figure 4a, the recording shows the reflection from the Al pusher surface prior to the emergence of the shock into the deuterium sample. For positive times, light was reflected from the shock front. The drive-beam focal spot was slightly nonuniform, and therefore produced a spatial variation in the breakout time at the pusher–deuterium interface, which is readily observable in the image. When the shock emerged from the Al interface, the reflected intensity dropped simultaneously with a shift of the fringe pattern.

Figure 4b shows the spatial variation of the fringe intensity across the target at a single moment around $t = 2 \text{ ns}$ during the experiment. We extract ϕ from a fit of the observed fringe intensity I to a sinusoidal function: $I(x,t) = A(x,t) + B(x,t) \sin \phi(x,t)$. The measured velocity²⁵ is $U_s = \lambda_p \phi(t) / 4\pi\tau(1 + \delta)$, where τ ($= 75 \text{ ps}$) is a delay time set by the configuration, $\phi(t)$ is the phase, and δ is a small correction associated with the interferometer.

Figure 4c shows how the fitted fringe phase varies with time in the center of the recorded image. From these data, we obtain a continuous record of phase, and therefore shock velocity as a function of time. The initial phase shift at $t = 0$ is ambiguous because the streak camera cannot resolve the fringe motion quickly enough during the 75 ps (τ) in which the fringes shift to the new phase. A shift of one fringe is $7 \mu\text{m/ns}$ with a resolution of <0.1 fringe. With high sensitivity, the initial shift can be several fringes, whereas the recording determines only the fractional part of the fringe shift. We resolved the ambiguity by comparing the velocimetry data with the radiograph of the shock trajectory. At shock breakout, the raw phase shift was -0.23 ± 0.05 fringes; the true phase shift was 2.77 ± 0.05 fringes, giving a shock speed of $18.9 \pm 0.3 \text{ km s}^{-1}$. In the absence of an independent diagnostic, this ambiguity can also be resolved by splitting the reflected light and recording data from two velocity interferometers with different sensitivities.

In Figure 5, we have integrated the extracted velocity to determine the shock trajectory (position as a function of time). We compare this with a streaked radiograph of the shock trajectory recorded simultaneously. Both trajectories agree within the $\pm 3\text{-}\mu\text{m}$ uncertainty of the radiographic measurement. In this example, the position inferred from the VISAR record after 6 ns is more accurate (we

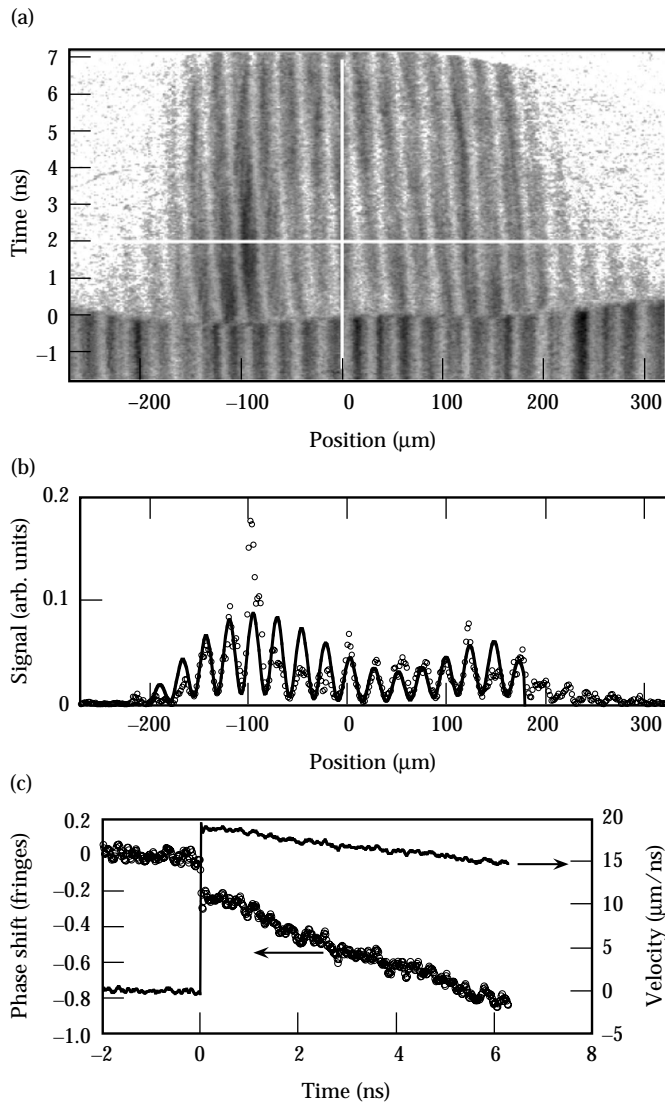


FIGURE 4. (a) Example of a streaked VISAR interferogram recorded for a decaying shock front. The initial phase shift is 2.77 fringes to the right, followed by a continuous shift to the left (deceleration) of ~ 0.7 fringes after 6 ns. (b) Interferogram intensity as a function of position x measured (symbols) and fitted (curve) at $t = 2$ ns [see the horizontal line in (a)]. (c) Raw phase at $x = 0$ (open circles) extracted from a series of fits similar to (b) for all times, and velocity (solid curve) obtained after applying an integer offset of +3 fringes to the raw phase data. The initial phase offset for $t < 0$ was subtracted. (50-00-1198-2195pb01)

estimate about $\pm 0.2 \mu\text{m}$) because the integration averages out random fluctuations in the phase, leaving systematic errors as the dominant contribution. This measurement also confirms unambiguously that the Doppler-shifted optical reflection originated directly from the shock front. Other possible choices for the initial fringe offset (e.g., 1.77 or 3.77 fringes) do not produce trajectories that correlate with any other moving surface or interface in the experiment.

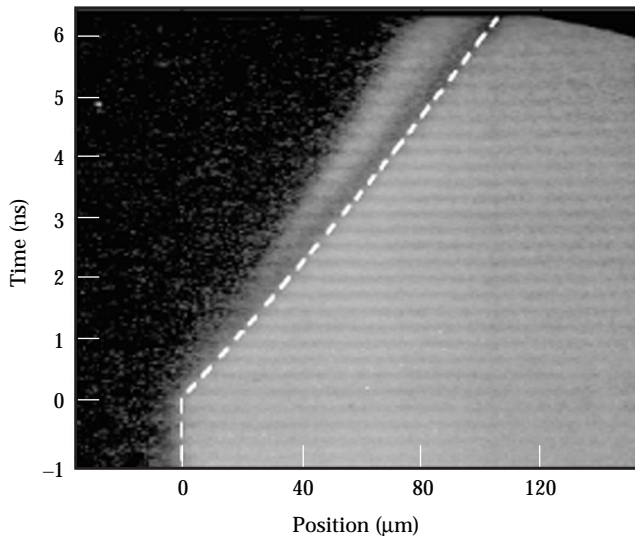


FIGURE 5. Streaked radiograph of the propagating shock front measured simultaneously with the record in Figure 4. The dashed curve shows the trajectory calculated from the measured velocity record in Figure 4c by integrating the velocity. The trajectory inferred from the velocity measurement lies within the resolution limit of the radiograph ($\pm 3 \mu\text{m}$) for the entire trajectory in the recording (up to 6 ns). (50-00-1198-2196pb01)

The agreement between two completely independent experimental techniques strengthens our confidence in the validity of the data produced by either diagnostic.

Optical Reflectivity

In addition to U_s , the interferometer also supplied instantaneous measurements of the (single-wavelength) reflectivity of the shock front. The optical reflectivity as a function of shock amplitude at the probe wavelength, 1064 nm, is plotted in Figure 6. At low shock pressures (20 GPa), the reflectivity is a few percent. However, at pressures greater than 55 GPa, the measured reflectivities are around 60%, characteristic of a metal. Because the temperature of the shocked D_2 is ~ 0.75 eV, much less than the ionization potential, the high reflectivity must be due to free electrons produced by a combination of density and thermal effects. The temperature is much less than the Fermi energy ϵ_F (~ 15 eV), so that the electron fluid is Fermi-degenerate. Because of this fact, the velocity distribution of the charge carriers depends mainly on density, and electron conduction is weakly temperature dependent. In plasma physics, such an ionization mechanism is referred to as pressure ionization. With respect to condensed matter terminology, ionized fluids with Fermi-degenerate conducting electrons are usually referred to as liquid metals. This is the most appropriate term to describe the high-pressure ionized fluid at pressures greater than 55 GPa.

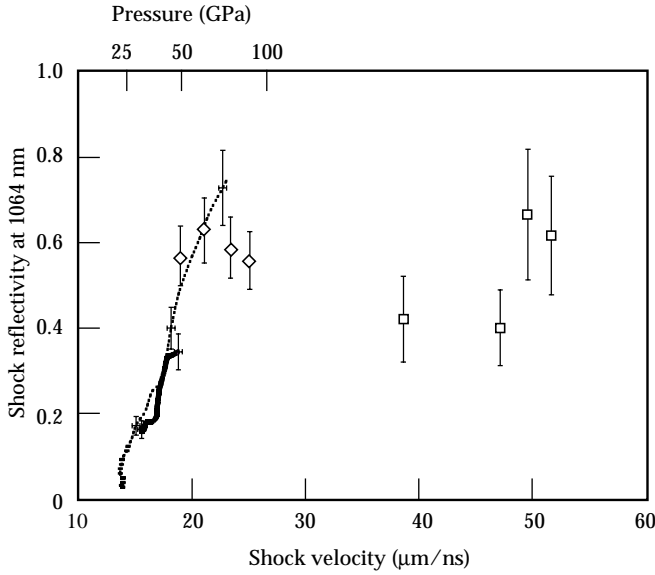


FIGURE 6. Reflectivity at 1064 nm of the shock front in liquid deuterium for shock speeds from 13.4 to 53 $\mu\text{m/ns}$. The open symbols are single-point measurements observed at the moment of shock breakout from the pusher–deuterium interface: diamonds are from experiments with Al pushers, squares are with Be pushers. The solid curves were extracted from two decaying-shock experiments. Indicated pressures were determined from Hugoniot data.²² (50-00-1198-2197pb01)

Shock Compression Results

At the lowest compression, the laser data agree with gas-gun results^{8,21} (Figure 7). The most striking feature is the pronounced compressibility observed at the same pressure at which D_2 becomes metallic. At 100 GPa, the SESAME⁷ D_2 Hugoniot density is 0.68 g/cm^3 ($\rho/\rho_0 = 4$), whereas the data show a density of 1.0 g/cm^3 ($\rho/\rho_0 = 5.88$), an increase of 47%. The softer EOS is similar to the models of Saumon–Chabrier^{16,18} and Ross.^{8,9} All of these models use minimization of the free energy of a mixture of molecular, atomic, and ionic species to determine species concentrations and establish the thermodynamics of the mixture. The methods, and in particular the interspecies potentials, are different in each case. Ross uses the expedient of a term determined by gas-gun shock-wave data. The Monte Carlo simulations¹⁹ are the closest to *ab initio*, i.e., an integration of the interactions of a finite set of individual nuclei and electrons. They show a high compression but at a low pressure. The high-temperature ACTEX model²⁷ also predicts a high shock density. However, the paths to higher pressure of these latter models lie to the low-density side of the data. A Hugoniot calculated from data produced by tight-binding molecular dynamics,²⁸ like SESAME, predicts only slight effects of dissociation and ionization.

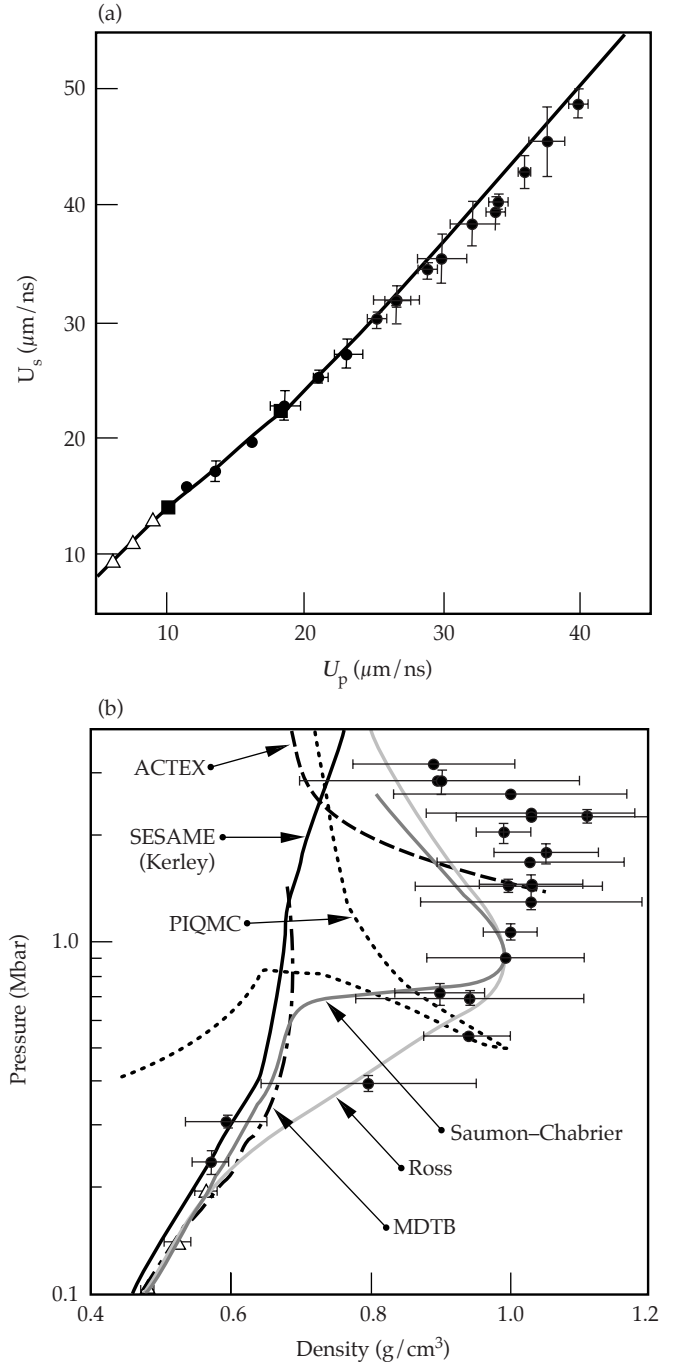


FIGURE 7. Hugoniot data presented as (a) measured U_s vs U_p and (b) inferred pressure vs density. Gas-gun data (triangles) are shown.^{8,21} The EOS model of Ross^{8,9} is shown as the light gray line. Other theoretical Hugoniots in (b) are from the widely used SESAME tabular EOS (black solid),⁷ the hydrogen EOS of Saumon and Chabrier that is used extensively in modeling of low-mass stellar objects (gray),¹⁶ the ACTEX theory that is known to be accurate at high temperatures (dash),²⁷ path integral quantum Monte Carlo simulations (dots),¹⁹ and tight-binding molecular dynamics simulations (dot dash).²⁸ (50-00-1198-2198pb01)

Above the turnaround on the Hugoniot, D_2 is a fully dissociated, partially ionized metallic fluid, so that as the pressure increases, the shock density is expected to move closer to that of an ideal gas.⁶ This trend was unclear in the original experiments. Here, the compression data above 200 GPa show a trend toward the ideal gas compression (Figure 7b).

Summary

Our data offer an independent assessment of the EOS of hydrogen isotopes on both sides of the metal–insulator phase transition. We have shown that hydrogen is ~50% more compressible at the transition than some theories predict.^{7,17,28} The question remains as to whether this transition is continuous. The flattened Hugoniots for two EOS models^{18,19} are the result of the Hugoniot passing through a predicted first-order phase transition from the molecular to the metallic state (Figure 7b). The other methods assume a continuous transformation. There is no evidence in the Hugoniot data for a first-order phase transition; both shock trajectories and reflectivity display a continuous variation from 25 to 70 GPa. Although there are significant uncertainties in the data, they suggest that the metal–insulator transition is continuous along the Hugoniot.

Acknowledgments

The authors thank N. W. Ashcroft, D. M. Ceperley, G. Chabrier, Y. M. Gupta, A. U. Hazi, N. C. Holmes, J. D. Johnson, G. I. Kerley, W. J. Nellis, M. Ross, F. J. Rogers, D. Saumon, T. Tajima, and D. A. Young for highly informative discussions and J. R. Asay, B. A. Hammel, J. D. Kilkenny, and L. G. Wiley for advice and support.

Notes and References

1. N. W. Ashcroft, *Phys. World* **8**, 43 (July, 1995).
2. E. Wigner and H. B. Huntington, *J. Chem. Phys.* **3**, 764 (1935); C. Friedli and N. W. Ashcroft, *Phys. Rev. B* **16**, 662 (1977); T. W. Barbee et al., *Phys. Rev. Lett.* **62**, 1150 (1989); H. Chacham and S. G. Louie, *Phys. Rev. Lett.* **66**, 10963 (1991).
3. J. H. Eggert et al., *Phys. Rev. Lett.* **66**, 671 (1991); C. Narayana, H. Luo, J. Orloff, and A. L. Ruoff, *Nature* **393**, 46 (1998).
4. S. T. Weir, A. C. Mitchell, and W. J. Nellis, *Phys. Rev. Lett.* **76**, 1860 (1996).
5. S. W. Haan et al., *Phys. Plasmas* **2**, 2480 (1995); J. D. Lindl, *Phys. Plasmas* **2**, 3933 (1995); S. Nakai and H. Takabe, *Rep. Prog. Phys.* **59**, 1071 (1996).
6. The Hugoniot is the locus of density, pressure, and energy states in a material following passage of a single shock. It is a well-defined curve on the EOS surface. The compression (ratio of shocked to unshocked density) generally increases with pressure and approaches a value of 4 for an ideal gas in the high-pressure limit. The ratio can be greater than 4 when accounting for endothermic processes, such as molecular excitations, dissociation, or ionization. At pressures above the region where these processes are complete, the compression must approach the ideal gas limit. EOSs for hydrogen isotopes are identical, except for a scale factor in density.
7. G. I. Kerley, *A Theoretical Equation of State for Deuterium*, Los Alamos National Laboratory, Report LA-4776 (1972); G. Kerley, *J. Chem. Phys.* **73**, 460 (1980).
8. N. C. Holmes, M. Ross, and W. J. Nellis, *Phys. Rev. B* **52**, 15835 (1995).
9. M. Ross, *Phys. Rev. B* **58**, 669 (1998).
10. H. M. Van Horn, *Science* **252**, 384 (1991).
11. R. Smoluchowski, *Nature* **215**, 691 (1967); W. B. Hubbard, *Science* **214**, 145 (1981); G. Chabrier, D. Saumon, W. B. Hubbard, and J. I. Lunine, *Astrophys. J.* **391**, 817 (1992); W. J. Nellis, M. Ross, and N. C. Holmes, *Science* **269**, 1249 (1995).
12. D. Saumon et al., *Astrophys. J.* **460**, 993 (1996).
13. D. Saumon, W. B. Hubbard, G. Chabrier, and H. M. Van Horn, *Astrophys. J.* **391**, 827 (1992).
14. W. B. Hubbard et al., *Phys. Plasmas* **4**, 2011 (1997).
15. G. Chabrier and I. Baraffe, *Astron. Astrophys.* **327**, 1039 (1997).
16. D. Saumon, G. Chabrier, and H. M. van Horn, *Astrophys. J. Suppl. Ser.* **99**, 713 (1995).
17. M. Ross, F. H. Ree, and D. A. Young, *J. Chem. Phys.* **79**, 1487 (1983).
18. D. Saumon and G. Chabrier, *Phys. Rev. A* **44**, 5122 (1991); *Phys. Rev. A* **46**, 2084 (1992); *Phys. Rev. Lett.* **62**, 2397 (1989).
19. W. R. Magro, D. M. Ceperley, C. Pierleoni, and B. Bernu, *Phys. Rev. Lett.* **76**, 1240 (1996); B. Militzer, W. Magro, and D. Ceperley, *Proc. International Conf. Strongly Coupled Coulomb Systems*, G. J. Kalman, K. B. Blagoev, and J. M. Rommel, Eds. (Plenum, New York, 1998).
20. H. Reinholz, R. Redmer, and S. Nagel, *Phys. Rev. E* **52**, 5368 (1995).
21. W. J. Nellis et al., *J. Chem. Phys.* **79**, 1480 (1983).
22. L. B. Da Silva et al., *Phys. Rev. Lett.* **78**, 483 (1997).
23. E. M. Campbell, *Laser Part. Beams* **9**, 209 (1991).
24. Y. M. Gupta and S. M. Sharma, *Science* **277**, 909 (1997).
25. L. M. Barker and R. E. Hollenbach, *J. Appl. Phys.* **43**, 4669 (1972).
26. P. M. Celliers et al., *Appl. Phys. Lett.* **73**, 1320 (1998).
27. F. J. Rogers, *Astrophys. J.* **310**, 723 (1986); F. J. Rogers, F. J. Swenson, and C. A. Iglesias, *Astrophys. J.* **456**, 902 (1996).
28. T. J. Lenosky, J. D. Kress, and L. A. Collins, *Phys. Rev. B* **56**, 5164 (1997).

DEVELOPING HIGH-PRESSURE, SOLID-STATE EXPERIMENTS ON THE NOVA LASER

<i>D. H Kalantar</i>	<i>A. A. Hauer*</i>	<i>J. S. Wark^{††}</i>
<i>E. A. Chandler</i>	<i>M. A. Meyers[†]</i>	<i>S. V. Weber</i>
<i>J. D. Colvin</i>	<i>K. O. Mikaelian</i>	<i>L. G. Wiley</i>
<i>D. M. Gold</i>	<i>B. A. Remington</i>	

Introduction

In a classical fluid model, when a light fluid accelerates a heavier fluid, the interface is Rayleigh–Taylor (RT) unstable. As a result, any mass modulation at the embedded material interface is unstable and can grow when accelerated. However, when a material is in the solid state, the strength of the material can counter the effect of the RT instability. The parameters that define whether a material is stable or unstable and undergoes instability growth in the solid state depend on the wavelength and amplitude of the modulation, acceleration history, foil thickness, and material properties, such as yield stress and shear modulus.

Solid-state instability growth will occur in the plastic flow regime. Plastic behavior is described by a semi-empirical constitutive model¹ that has been developed for phenomena that occur at strain rates $<10^5 \text{ s}^{-1}$. Such plastic flow has been characterized either microscopically by the theory of lattice dislocations, or macroscopically by an effective lattice viscosity.² The best approach to describe the plastic flow of a material may depend on the specifics of a particular experiment. Neither approach has been well tested experimentally at pressures over 1 Mbar or strain rates $>10^8 \text{ s}^{-1}$.

Analytically, stability boundaries can be defined, as described by Lebedev et al.^{3,4} Such boundaries can be used to determine whether material strength is sufficient to inhibit plastic deformation, completely stabilizing growth of a modulation. Outside the stability boundary, the material may undergo plastic deformation, and the modulated interface may grow. Such deformation and growth have been demonstrated by Barnes et al.⁵ using Al plates with a preimposed

surface modulation, where the plates are driven with a high-explosive drive, and by Lebedev et al.^{3,4} using Al and Ti plates in similar experiments.

We are conducting experiments on the Nova laser⁶ to study the plastic flow of metals at high pressure and very high strain rates (10^7 to 10^8 s^{-1}). Our experiments are designed to compress Cu foils by a factor of 1.5 to 2.0 with staged shocks reaching peak pressures of about 3 Mbar. The RT instability is the observable “probe” in such experiments, with departures from classical (liquid) behavior characterizing the material-strength properties at high pressure and compression.

In this paper, we present details of the hohlraum target design and x-ray drive characterization for the Cu foil experiment. We also present calculations of the material state with this drive, and results from preliminary instability growth experiments using Cu foils with a preimposed modulation. With an accurate determination of the actual drive history, the Cu foil is calculated to melt on decompression, but the instability growth is calculated to be similar for Cu both as a solid and a fluid. We discuss the stability boundaries for solid-state plastic flow for the Nova experiments and conclude with a discussion of an improved experimental design using an Al foil, where the foil remains solid throughout the experiment, and strength effects should be considerably enhanced.

Experimental Details

The hydrodynamics experiments are conducted using an x-ray drive created in a cylindrical Au hohlraum. This x-ray drive accelerates a metal foil payload by ablation of a brominated polystyrene ablator layer. A preimposed sinusoidal modulation is located on the metal foil at the embedded interface. The growth of the RT-unstable interface is then diagnosed by face-on x-ray radiography using a gated x-ray framing camera.⁷

^{*}Los Alamos National Laboratory, Los Alamos, NM

[†]University of California at San Diego, La Jolla, CA

^{††}Department of Physics, Clarendon Laboratory, University of Oxford, Oxford, UK

Figure 1 shows the target geometry. The hohlraum (Figure 1a) is cylindrically symmetric with internal shielding to prevent hard x rays from preheating the Cu foil due to M-band emission coming from the laser spots on the inner hohlraum wall. The hohlraum is 3.44 mm in diameter and 5.75 mm long. The laser entrance holes are 1.2 mm in diameter, and the holes in the internal shields are 1.6 mm in diameter.

The hydrodynamics package shown in Figure 1b is mounted on the side of the hohlraum. It consists of a 20- μ m-thick brominated polystyrene [CH(Br)] foil pressed in contact with the metal foil. The CH(Br) ablator has a 3% atomic Br fraction to enhance opacity to soft x rays. We typically use 18- to 19- μ m-thick, oxygen-free, high-conductivity Cu foils that have been rolled and then machined to have a sinusoidal modulation.

Eight Nova beams generate an x-ray radiation environment in the two laser-heated cavities of the target. Reemitted x rays that pass through the holes in the internal shields heat the central (x-ray-heated) cavity and ablate material from the CH(Br) ablator, launching a series of shocks into the package. Without the internal shields, the 2- to 4-keV Au M-band component of the spectrum of emission from the laser plasmas would be absorbed throughout the full volume of the package, potentially preheating the Cu foil and causing it to melt and decompress. With internal shielding, the x rays incident on the ablator are generated by re-emission from the regions of the wall that are not directly illuminated by the laser beams. The spectrum of these x rays is nearly Planckian, without a significant M-band component.

The x-ray drive ablates the brominated plastic, launching a series of shocks into the metal foil, compressing and accelerating it away from the hohlraum. We diagnose the growth of the perturbed, unstable,

embedded interface by x-ray radiography using a large-area (0.7-mm-diameter focal spot) backlighter. The backlighter is generated with two additional Nova beams aligned to a separate Fe backlighter foil generating He_α x rays at 6.7 keV. A 2- to 3-ns, square laser pulse shape was used for these backlighter beams, and delays relative to the drive beams ranged from 5 to 14 ns.

X-Ray Drive Measurement

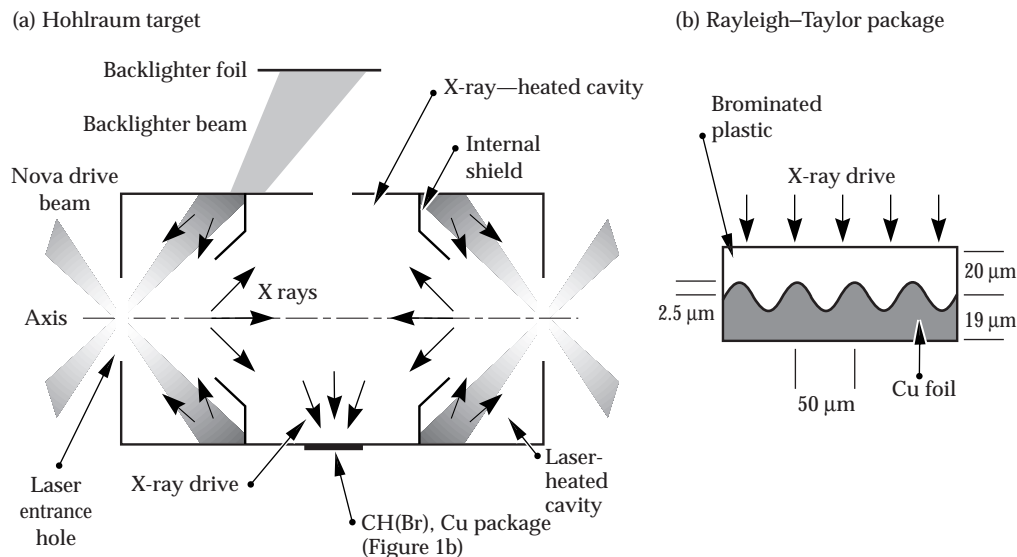
The laser pulse shape is designed to generate an x-ray drive that launches two shocks, compressing the Cu foil to a peak pressure of about 3 Mbar while maintaining the metal foil in the solid state. This pulse shape is shown in Figure 2. It has a peak-to-foot intensity ratio of about 30. We have characterized the x-ray drive using the Dante diagnostic⁸ and side-on foil trajectories.

The Dante diagnostic is a filtered array of absolutely characterized x-ray diodes. The diodes are positioned to view the spectral soft-x-ray emission from the inner wall of the central section of the hohlraum through a Be-lined diagnostic hole. With the high-contrast shaped laser pulse, only the lowest energy channels of the Dante detected signals, starting at about 1.0 ns. The absolute signal levels from these diodes were used to estimate the Planckian drive temperature, which started at about 15 eV and rose to 40 eV at 3.5 ns. At temperatures greater than 40 eV, enough channels recorded signals that a spectral unfold could be performed. The measured radiation temperature rose from 40 eV at 4.0 ns to 90 eV at the end of the laser pulse at 6.5 ns, and then slowly decayed as energy was lost into the hohlraum walls and through the laser entrance holes.

The measured drive temperature in Figure 2 is shown along with the laser pulse shape. Note that the

FIGURE 1. (a) Schematic of the internally shielded hohlraum and geometry for face-on radiography. (b) Modulated foil package mounted on the side of the hohlraum.

(08-00-1198-2247pb01)



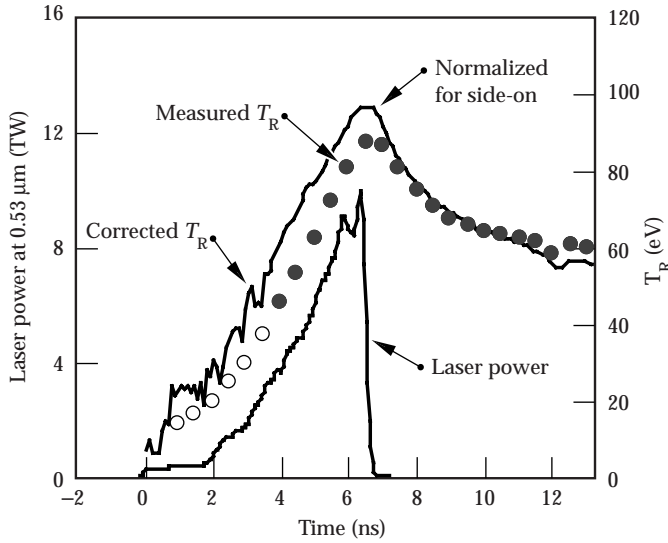


FIGURE 2. Laser pulse shape and x-ray drive temperature for the low-isentrope drive. (08-00-1198-2248pb01)

Dante measures the reemission from the wall of the hohlraum at the midplane. The package experiences the x-ray drive that is incident on the wall, the incident flux temperature T_I , which is related to the measured reemission flux temperature T_R by the albedo⁹ α of the wall according the equation:

$$T_I = T_R / \alpha^{1/4} \quad (1)$$

We performed a full simulation of the hohlraum target using the LASNEX computer code,¹⁰ including the laser power incident in the laser-heated regions, to estimate the drive temperature at the package. This resulting corrected drive is shown in Figure 2. As a consistency check for the low-temperature foot portion of the pulse, we analytically solve the power-balance prescription from Rosen and Lindl.¹¹ We consider the power flow in the laser-heated and x-ray-heated cavities of the internally shielded hohlraum. The laser power that enters the laser-heated cavities is equal to the sum of the losses through the laser entrance hole, losses into the wall, and power flow into the x-ray-heated cavity. Similarly, the power flow into the x-ray-heated cavity is equal to losses to the hohlraum wall and losses out to the laser-heated cavities. Incorporating the temporal scaling of the wall albedo from high-power, 1-ns drive experiments, we estimate that the temperature of the foot at 1 ns is about 24 eV. The LASNEX-simulated drive is in good agreement with this scaling at 20 to 25 eV.

The peak portion of the drive was verified with a side-on foil trajectory measurement. For this measurement, we mounted a package consisting of 22- μm

CH(Br) with 13- μm Cu on the side of the hohlraum. We recorded an x-ray shadow image of the foil as it was accelerated away from the hohlraum using a high-magnification (55 \times), x-ray streaked imager (Figure 3). To match the overall motion of the foil, the albedo-corrected drive is reduced in the simulations by only about 2% in radiation temperature T_R for times $t > 5$ ns. This adjustment is interpreted as a correction due to the uncertainty in the opacity of the ablator at low drive temperatures, and in the initial Dante drive measurement itself.

Using the simulated x-ray drive in the hohlraum, we modeled the conditions in the foil package with 1D LASNEX. Figure 4 shows the calculated temperature and pressure at the embedded ablator-Cu interface. The x-ray drive ablatively launches two shocks into the copper. The first shock arising from the low foot is about 0.4 Mbar in the Cu, and the second is 3 Mbar. Subsequent reflected shocks maintain the high pressure until about 8 ns. At about this time, the material

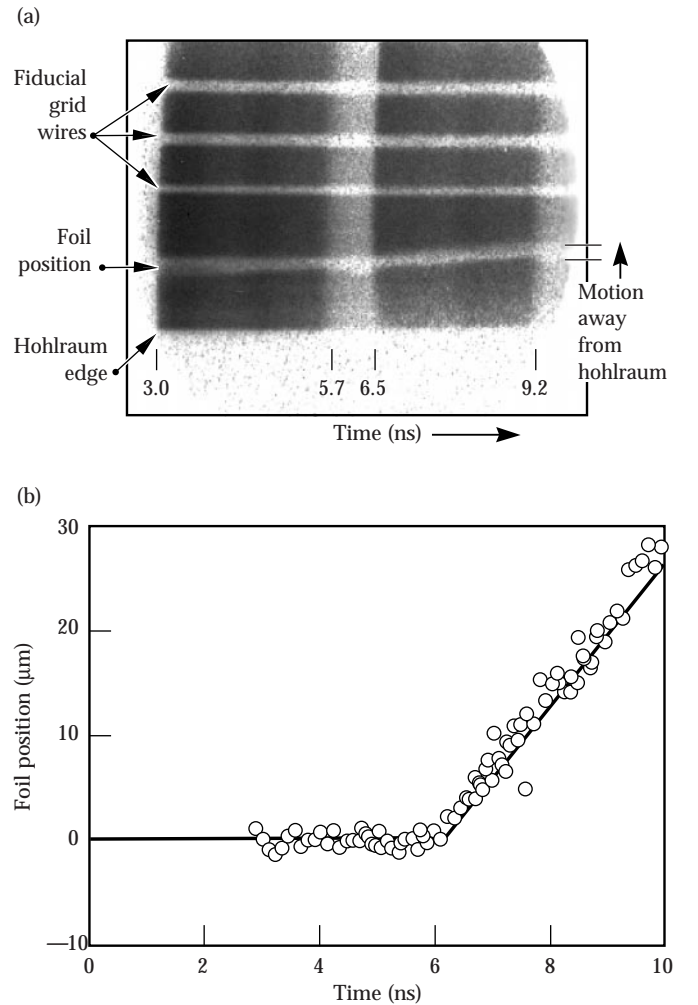


FIGURE 3. Side-on trajectory measurement for x-ray drive characterization. (a) Streaked data. (b) Measured trajectory of the rear surface of the target. (08-00-1198-2249pb01)

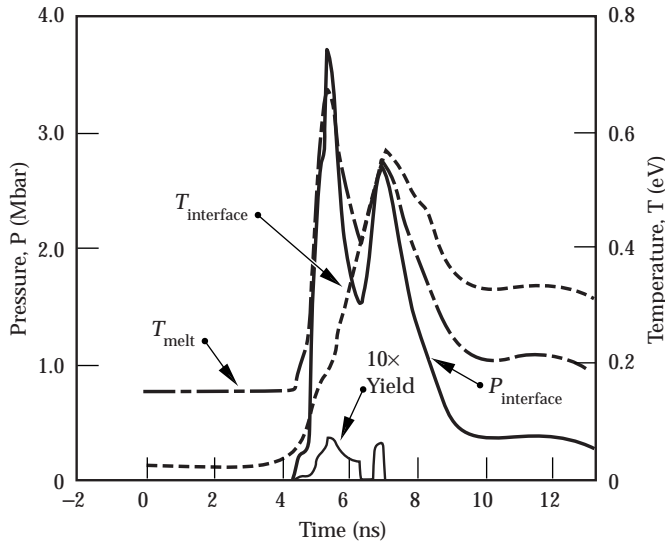


FIGURE 4. Pressure and temperature calculated at the CH(Br)-Cu interface with the low-isentrope drive. (08-00-1198-2250pb01)

temperature at the interface exceeds the melt temperature, which we calculate by the Lindemann law

$$T_m = T_{mo} \exp[2a(1 - 1/\eta)] \eta^2(\gamma_0 - a - 1/3), \quad (2)$$

where T_{mo} is the melt temperature at constant volume, η is the compression of the sample, γ is the Grüneisen gamma, and a is the coefficient of volume dependence of γ as defined by Steinberg et al.¹

The low-isentrope drive is calculated to keep the foil very near an adiabat throughout the experiment. Figure 5 shows the internal energy at the Cu interface plotted as a function of density (compression) from $t = 0$ to $t = 15$ ns. Note that this trajectory is sensitive to the temperature of the foot of the shaped drive pulse. If the albedo correction for the foot is incorrect, the timing of the first shock may be incorrect. In particular, if the foot drive is much lower,

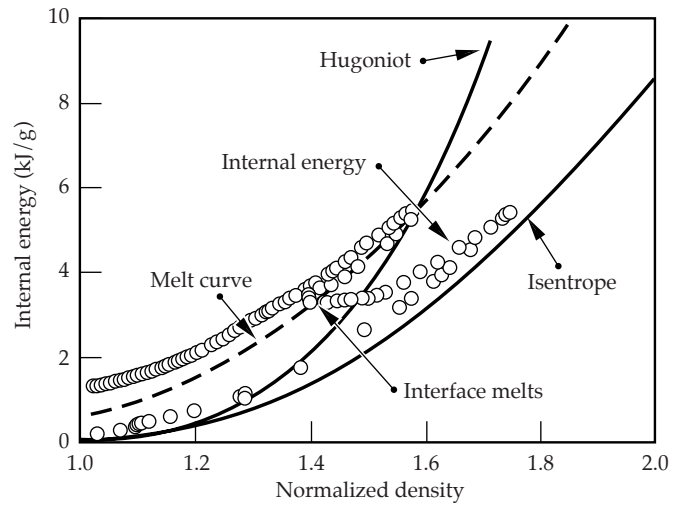


FIGURE 5. Internal energy trajectory of Cu at the CH(Br)-Cu interface for the low-isentrope x-ray drive. (08-00-1198-2251pb01)

then the second shock may catch up before it reaches the interface, placing the metal foil on a higher adiabat and potentially melting it. For the case of the actual drive, the shocks overlap about half way through the foil, melting the back side. The interface then melts with the rarefaction. Adjusting the level of the foot to be somewhat higher is one way to keep the temperature at the interface below the melt curve for longer times, as discussed later.

Experiments to characterize the foot drive were done using both active shock breakout^{12,13} and dynamic Bragg diffraction techniques^{14,15} to measure shock timing. For the active shock breakout measurement, we used a displacement Michelson interferometer to measure motion of the back surface of a 17- μ m-thick, Al flat target mounted on the side of the hohlraum. Motion of the back surface due to the shock transit and breakout through the foil is evident by a shift in the fringe pattern, as shown in Figure 6. Streaked interferometer data are shown in Figure 6a,

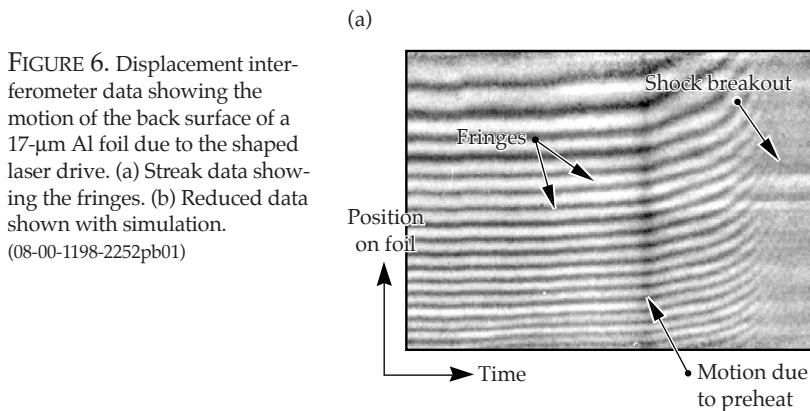


FIGURE 6. Displacement interferometer data showing the motion of the back surface of a 17- μ m Al foil due to the shaped laser drive. (a) Streak data showing the fringes. (b) Reduced data shown with simulation. (08-00-1198-2252pb01)

and the analyzed position as a function of time for the back surface is shown in Figure 6b. This measurement was done with an interferometer that operates at a wavelength of 400 nm, so a full fringe shift corresponds to one-half wavelength ($0.2\ \mu\text{m}$) of motion at the back surface.

The interferometer data show motion that may be due to the breakout of the elastic precursor wave or to some amount of preheat at the back surface of the Al foil, and then the rapid motion and disappearance of fringes as the main shock breaks out. We show simulated position as a function of time for the back surface with some imposed preheat to illustrate how this measurement is affected by low preheat levels.

For the case of Bragg diffraction, we used a CH(Br) ablator with a $40\text{-}\mu\text{m}$ -thick Si crystal as a surrogate for the Cu foil mounted on the side of the hohlraum. A V backlighter generated x rays at 5.3 keV, diffracting off the crystal through the brominated plastic ablator. When the shock transits the ablator and reaches the interface, it compresses the Si lattice. This is observed as a shift in the Bragg diffraction angle of the backlighter x rays. Figure 7 shows data obtained using this technique with a square laser pulse shape.^{14–16} The estimated shock strength in the Si for this experiment was 350 kbar, compared to the calculated 650-kbar first shock strength in Cu for this shaped x-ray drive. Note that the presence of the diffraction signal under shock compression is consistent with the assumption that the Si remains solid under compression.

Instability-Growth Experiments

Sinusoidal modulations with amplitudes of 1.0 to $2.5\ \mu\text{m}$, and wavelengths of 20 and $50\ \mu\text{m}$, were machined in the Cu foils. A $20\text{-}\mu\text{m}$ thickness of brominated plastic ablator was pressed onto the modulated foils, and then the package was mounted over a hole in the side of the hohlraum. The x-ray drive ablatively launched a series of shocks to compress and accelerate the metal foil away from the side of the hohlraum.

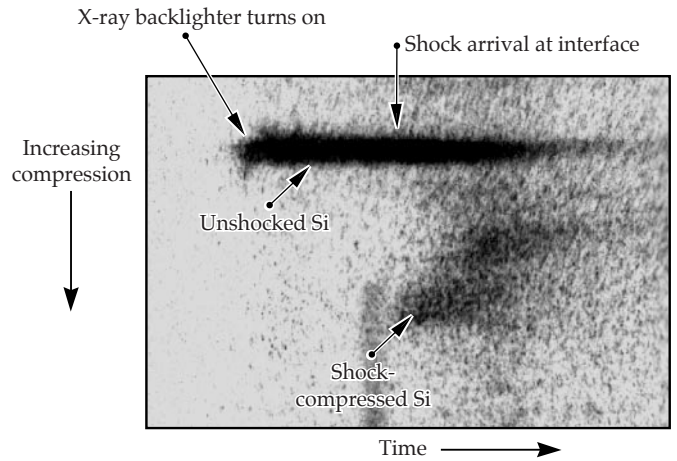


FIGURE 7. Streaked diffraction pattern from the CH(Br)-Si embedded interface showing a shift in the diffraction peak at the time the shock reaches the interface. (08-00-1198-2253pb01)

We recorded radiographic images of the foil using 6.7-keV Fe x rays. Up to 16 images were recorded on four independently timed microchannel-plate striplines on each laser shot, using a flexible x-ray imager¹⁷ with a 230-ps gate pulse. The modulation amplitude in optical depth was calculated by Fourier analysis at each time. The Fourier amplitude was normalized to the initial contrast in optical depth, which we measured on a separate shot.

Figure 8a shows the instability growth factors for $\lambda = 50\ \mu\text{m}$, $2.5\text{-}\mu\text{m}$ -amplitude modulations; Figure 8b shows the growth factors for $\lambda = 20\ \mu\text{m}$, $1.0\text{-}\mu\text{m}$ -amplitude modulations. In these experiments, the ablator-metal interface moved only about $40\ \mu\text{m}$ during the time the measurements were made, and the overall growth factors were small, which means the modulation remained nearly linear. As a result, when we normalize the measurements with the initial (measured) contrast at that wavelength (x-ray mean-free-path and instrument resolution function), the instrument resolution (modulated transfer function ≈ 0.65 at $8\times$ instrument

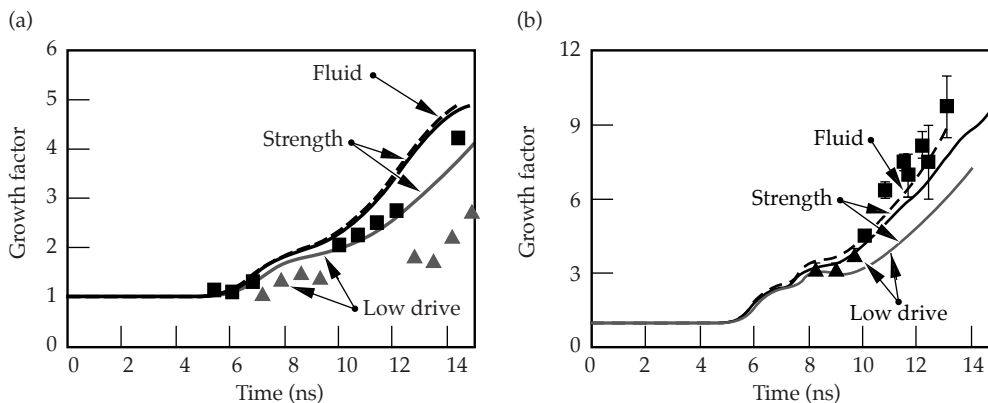


FIGURE 8. Instability growth factors for (a) $50\text{-}\mu\text{m}$ and (b) $20\text{-}\mu\text{m}$ wavelength modulation at the embedded CH(Br)-Cu interface. LASNEX simulations were done with and without strength. (08-00-1198-2254pb01)

magnification for $\lambda = 50 \mu\text{m}$, and 0.6 at $12\times$ for $\lambda = 20 \mu\text{m}$) is removed from the measurement.

Figure 8 also shows the growth factors simulated with LASNEX using both a fluid model, and the constitutive material strength model described by Steinberg et al. Separate calculations are shown in Figure 8 for experiments where the peak portion of the laser pulse shape was reduced by about 20% (indicated on the figure by “low drive”) because the growth is sensitive to the actual drive history. The difference between the fluid and material strength simulations for $\lambda = 20 \mu\text{m}$ and $50 \mu\text{m}$ is small. For the $50\text{-}\mu\text{m}$ wavelength case, the simulations are nearly identical. For the $20\text{-}\mu\text{m}$ wavelength case, material strength leads to about 20% less growth, but the difference due to variation in the laser power history for the different shots is about this order, making it difficult to confirm that reduced growth is due to the material strength at $\lambda \geq 20 \mu\text{m}$ with these Cu foils.

By extending the simulations to shorter-modulation wavelengths, $\lambda < 20 \mu\text{m}$, we observed a greater effect due to material strength. The calculated growth factors for a range of wavelengths from 5 to $50 \mu\text{m}$ are shown in Figure 9, plotted after the interface moved a distance of $20 \mu\text{m}$. The enhanced difference between fluid and strength modeling at $\lambda \leq 20 \mu\text{m}$ suggests that with some modifications we should be able to observe the effect of strength stabilization in the Nova experiments. Measuring perturbation growth factors at $\lambda = 5$ to $10 \mu\text{m}$ with gated pinhole imaging is problematic because of reduced exposure levels and diffraction effects with apertures smaller than $5 \mu\text{m}$. As a result, this experiment would be improved with a design in which longer wavelengths would be stabilized.

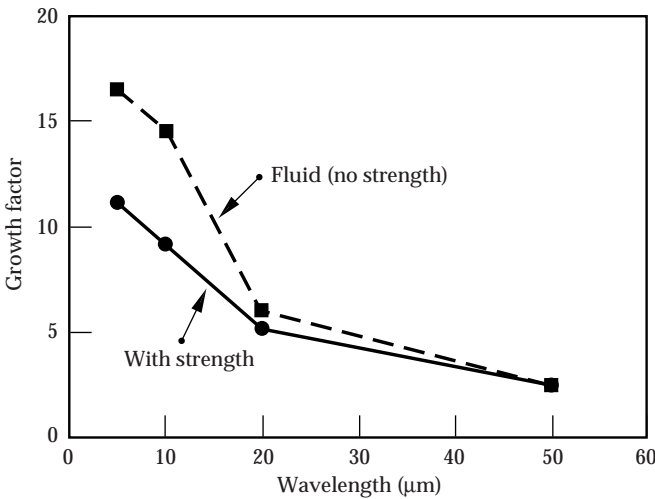


FIGURE 9. Growth factor as a function of wavelength for a modulated Cu foil, plotted after the interface moved a distance of $20 \mu\text{m}$. (08-00-1198-2255pb01)

Strength Stabilization

The pressure-enhanced yield strength and shear modulus are given in the strain-rate-independent constitutive model by Steinberg et al. as

$$Y(P, T) = Y_0 \left[1 + \beta (\epsilon + \epsilon_i) \right]^n \times \left[1 + \left(\frac{Y_P}{Y_0} \right) \frac{P}{\eta^{1/3}} - \left(\frac{G_T}{G_0} \right) (T - 300) \right] \quad (3a)$$

and

$$G(P, T) = G_0 \left[1 + \left(\frac{G_P}{G_0} \right) \frac{P}{\eta^{1/3}} - \left(\frac{G_T}{G_0} \right) (T - 300) \right], \quad (3b)$$

where Y is the yield strength, G is the shear modulus, ϵ is the strain, and η is the compression. In this formulation, the pressure P and temperature T dependence and the effect of work hardening β are included. The initial value for yield strength is $Y_0 = 1.2 \times 10^{-3}$ Mbar, and the initial value for shear modulus is $G_0 = 0.477$ Mbar for a Cu foil.

At a shock pressure of 3 Mbar, the Cu foil is compressed by about a factor of >1.5 , at which point the yield strength is 50 kbar, enhanced by a factor of about 40 over the nominal value Y_0 . The shear modulus is about 3.6 Mbar. Under these conditions, the yield strength is exceeded by more than one order of magnitude, putting the foil into the plastic flow regime and allowing for instability growth in the solid state.

Estimates can be made as to whether the modulation on the Cu package grows or not, based on a stability boundary analysis assuming steady-state conditions. The Miles criterion, based on linear theory,¹⁸ assumes a modulation amplitude η_0 much smaller than the wavelength. It establishes that for a semi-infinite slab with a modulated surface, the modulation is stable if its wavelength is shorter than the cut-off wavelength

$$\lambda_\infty = 4\pi G / \rho g, \quad (4)$$

where g is the acceleration. Including the finite thickness of the foil, Lebedev et al. extend the Miles theory and predict this cutoff is at

$$\lambda_c = \frac{2\lambda_\infty}{1 + \sqrt{1 + 8\sqrt{3}c^2/gH}}, \quad (5)$$

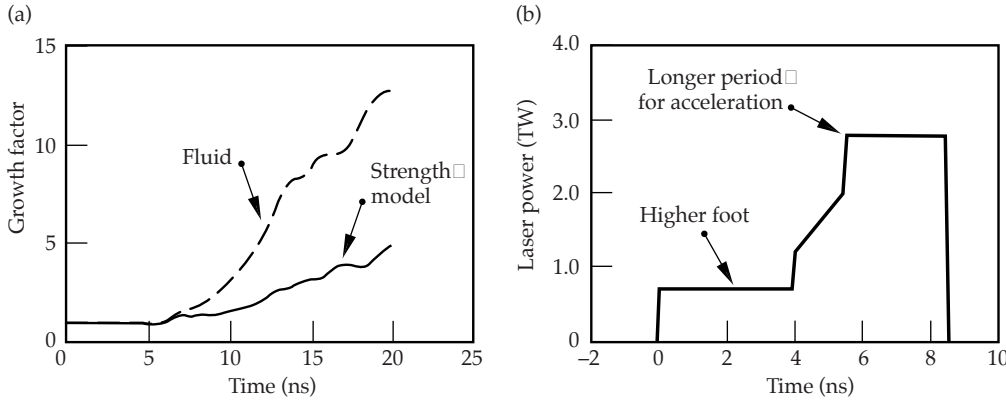


FIGURE 10. (a) Growth factor as a function of time, calculated for a modulated Al foil with a perturbation wavelength $\lambda = 20 \mu\text{m}$ and initial amplitude of $0.5 \mu\text{m}$. Simulations were done with and without material strength. (b) Laser pulse shape for the Al instability experiment. (08-00-1198-2256pb01)

where c is the speed of the shear wave, and λ_∞ corresponds to the Miles cutoff wavelength, Eq. 4. For the conditions of this experiment, $\lambda_c = 30 \mu\text{m}$. Therefore, at $\lambda = 20 \mu\text{m}$, which is below the cutoff wavelength, perturbations with very small initial amplitude under steady-state conditions should not grow.

We observed, however, that the $\lambda = 20 \mu\text{m}$ modulation grows in both the experiment and the simulation. Growth results because the amplitude exceeds the critical amplitude given by Lebedev et al. This amplitude cutoff is given by the expression

$$\eta_c = \eta_c(\text{Drucker}) \left[1 - 0.86 e^{(2\pi H / \sqrt{3\lambda})} \right] \times \left[\left(1 - e^{(-2\pi H / \sqrt{3\lambda})} \right)^2 - \left(\frac{\lambda}{\lambda_\infty} \right)^2 \right], \quad (6)$$

where

$$\eta_c(\text{Drucker}) = \frac{2Y}{\rho g} \quad (7)$$

is the wavelength-independent critical amplitude threshold to instability growth from Drucker.¹⁹ For these experiments, at $\lambda = 20 \mu\text{m}$, the amplitude threshold is $<1 \mu\text{m}$, which is much too small to diagnose by x-ray backlighting using a hard-x-ray backlighter at 6.7 keV.

To design an experiment in a regime with a much greater reduction in growth due to material strength, we must consider a material with a lower density and a larger value for the derivative of the yield strength with pressure to maximize the effect of strength on the RT instability growth. Aluminum is one such metal, with a pressure derivative of the yield strength that is a factor of 2 larger than that for Cu. For 7075

(or 6061) Al, which has an initial yield strength of 4.2 kbar, we calculated the growth of $20\text{-}\mu\text{m}$ wavelength with and without strength using an initial amplitude of $0.5 \mu\text{m}$. The case with strength grows less than a factor of 2, whereas the fluid case shows a growth factor of about 5 at $t = 12 \text{ ns}$ (Figure 10a). Note that to time the shocks so that they do not overlap in the metal foil, the foot portion of the drive is raised and lengthened (Figure 10b). With this design, the peak pressure in the Al is 1.4 Mbar, and the foil is calculated to remain solid throughout, as indicated by a plot of the internal energy trajectory in Figure 11.

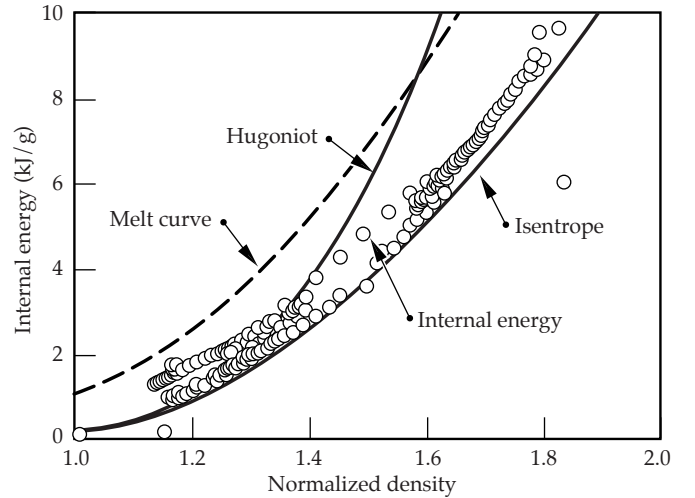


FIGURE 11. Internal energy trajectory calculated for an Al foil at the CH(Br)-Al interface. The modified drive is expected to shock the foil without melting it. (08-00-1198-2257pb01)

Summary

We have developed an x-ray drive to shock-compress metal foils in the solid state using an internally shielded hohlraum with a high-contrast shaped laser pulse. We used a combination of Dante measurements, side-on foil trajectories, and shock-timing measurements to develop an understanding of the x-ray drive. Hydrodynamic experiments that are designed to study growth of the RT instability in the plastic-flow regime have been started. Measurements of initial 20- to 50- μm wavelengths and 1- to 2.5- μm amplitude perturbations are presented and compared with simulations in this paper. For this experiment, the growth of the instability in fluid and solid states were calculated to be nearly the same. Analytic stability analysis is consistent with the instability growing in the plastic-flow regime. However, by redesigning the experiment to use an Al foil, the foil will remain in the solid state throughout, and the effect of material strength may be enhanced considerably, allowing us to conduct experiments on either side of the stability boundary.

Acknowledgment

We acknowledge the technical support of the Nova Operations and Target Fabrication groups at Lawrence Livermore National Laboratory.

Notes and References

1. D. J. Steinberg, S. G. Cochran, and M. W. Guinan, *J. Appl. Phys.* **51**, 1498 (1980).
2. L. C. Chhabildas and J. R. Asay, *J. Appl. Phys.* **50**, 2749 (1979).
3. A. I. Lebedev, P. N. Nizovtsev, and V. A. Rayevsky, in *Proceedings of the 4th International Workshop on the Physics of Compressible Turbulent Mixing*, 29 March–1 April, 1993 (Cambridge University Press, Cambridge, England, 1993), p. 81.
4. A. I. Lebedev, P. N. Nizovtsev, V. A. Rayevsky, and V. P. Soloviov, in *Proceedings of the 6th International Workshop on the Physics of Compressible Turbulent Mixing*, 17–21 June, 1997 (I.U.S.T.I./C.N.R.S., Marseille, France, 1997).
5. J. F. Barnes, P. J. Blewett, R. G. McQueen, K. A. Meyer, and D. Venable, *J. Appl. Phys.* **45**, 727 (1974).
6. E. M. Campbell, J. T. Hunt, E. S. Bliss, D. R. Speck, and R. P. Drake, *Rev. Sci. Instrum.* **57**, 2101 (1986).
7. P. M. Bell, J. D. Kilkenny, G. Power, R. Bonner, and D. K. Bradley, in *Ultra-high Speed and High Speed Photography, Photonics, and Videography '89* (SPIE, Bellingham, WA, 1989), *Proc. SPIE*, Vol. 1155, pp. 430–444.
8. H. N. Kornblum, R. L. Kauffman, and J. A. Smith, *Rev. Sci. Instrum.* **57**, 2179 (1986).
9. R. L. Kauffman, H. N. Kornblum, D. W. Phillion, C. B. Darrow, B. F. Lasinski, L. J. Suter, A. R. Thiessen, R. J. Wallace, and F. Ze, *Rev. Sci. Instrum.* **66**, 678 (1995).
10. G. B. Zimmerman and W. L. Kruer, *Comments Plasma Phys. Controlled Fusion* **2**, 51 (1975).
11. J. Lindl, *Phys. Plasmas* **2**, 3933 (1995).
12. K. S. Budil, P. Celliers, G. W. Collins, L. B. Da Silva, R. Cauble, R. J. Wallace, G. Chiu, and A. Ng, in *Inertial Confinement Fusion Quarterly Report 7(1)*, UCRL-LR-105821-97-1 (1997); copies available from the National Technical Information Service, Springfield, VA.
13. G. W. Collins, P. Celliers, L. B. Da Silva, R. Cauble, D. Gold, M. Foord, K. S. Budil, R. Stewart, N. C. Holmes, M. Ross, B. A. Hammel, J. D. Kilkenny, R. J. Wallace, and A. Ng, *Phys. Plasmas* **5**, 1864 (1998).
14. Q. Johnson, A. Mitchell, R. N. Keeler, and L. Evans, *Phys. Rev. Lett.* **25**, 1099 (1970).
15. J. S. Wark et al., *Phys. Rev. B* **35**, 9391 (1987).
16. D. H. Kalantar et al., accepted for publication in *Rev. Sci. Instrum.* (to appear in Jan 1999).
17. K. S. Budil et al., *Rev. Sci. Instrum.* **67**, 485 (1996).
18. J. W. Miles, Technical Report No. GAMD-7335, General Dynamics, San Diego, CA (1966).
19. D. C. Drucker, *Ingenieur-Archiv* **49**, 361 (1980).

CHARGED-PARTICLE SPECTROSCOPY: A NEW DIAGNOSTIC FOR INERTIAL FUSION IMPLOSIONS

T. W. Phillips

*R. D. Petrasso**

M. D. Cable

T. C. Sangster

*D. G. Hicks**

*F. H. Se'guin**

*C. K. Li**

*J. M. Soures***

Introduction

The prospect of ignition in inertially confined fusion (ICF) targets challenges our ability to diagnose fuel conditions within the implosion. A collaboration of efforts at Lawrence Livermore National Laboratory (LLNL), Massachusetts Institute of Technology (MIT), and the University of Rochester (UR) is developing the technique of charged-particle spectroscopy to help meet the challenge. This diagnostic technique will

measure signals sensitive to the yield, areal density (fuel and core), and asymmetry of implosions.¹ Such measurements will help guide the achievement of fusion pellet ignition. Table 1 illustrates the variety of fusion reaction products that can be measured by the technique of charged-particle spectroscopy to provide a detailed picture of conditions in the fusion implosion.

Depending on the yield and density attained in compression, various charged-particle reaction products will

TABLE 1. Nuclear reactions and reaction products from fusion reactions.

Reaction type	Reactions	Observed ^a in spectrometer data
Primary fusion reactions	$D + D \rightarrow T (1.01 \text{ MeV}) + p (3.02 \text{ MeV})$ $\rightarrow n (2.45 \text{ MeV}) + {}^3\text{He} (0.8 \text{ MeV})$ $D + T \rightarrow \alpha (3.5 \text{ MeV}) + n (14.1 \text{ MeV})$ $D + {}^3\text{He} \rightarrow \alpha (3.6 \text{ MeV}) + p (14.7 \text{ MeV})$	T, p α α, p
Secondary fusion reactions	${}^3\text{He} (0.82 \text{ MeV}) + D \rightarrow \alpha (6.6\text{--}1.7 \text{ MeV}) + p (12.5\text{--}17.4 \text{ MeV})$ $T (1.01 \text{ MeV}) + D \rightarrow \alpha (6.7\text{--}1.4 \text{ MeV}) + n (11.9\text{--}17.2 \text{ MeV})$	
14.1-MeV neutron knock-ons	$n (14.1 \text{ MeV}) + p \rightarrow n' + p (\leq 14.1 \text{ MeV})$ $n (14.1 \text{ MeV}) + D \rightarrow n' + D (\leq 12.5 \text{ MeV})$ $n (14.1 \text{ MeV}) + T \rightarrow n' + T (\leq 10.6 \text{ MeV})$	D T
30.8-MeV tertiary reaction chain	$D + T \rightarrow \alpha (3.5 \text{ MeV}) + n (14.1 \text{ MeV})$ (step 1) $n (14.1 \text{ MeV}) + D \rightarrow n' + D (\leq 12.5 \text{ MeV})$ (step 2) $D (12.5 \text{ MeV}) + {}^3\text{He} \rightarrow \alpha + p (\leq 30.8 \text{ MeV})$ (step 3)	

^aIn this column, p = protons, D = deuterons, T = tritons, and α = alphas

*Massachusetts Institute of Technology, Cambridge, MA

**University of Rochester, Rochester, NY

escape the compressed fuel and can be exploited for diagnostic measurements. The reaction products include primary products, such as protons in deuterium–deuterium (DD) fusion at low areal density. As areal density increases, higher-energy neutron knock-on products or secondary reaction products can be detected. At still higher areal density, energetic tertiary protons with birth energies from 27 to 30.8 MeV will characterize the compressed fuel of igniting implosions. Areal density measurements in different directions can be made with multiple spectrometers to determine the symmetry of the final fuel configuration. Measurement of Doppler broadening of the spectra of these charged particles will provide information on the temperature of fusion reactants.

Diagnostic Technique

The challenge of determining the energy spectra of protons, deuterons, tritons, or alphas from an ICF target is that for every particle, there are two quantities to be measured: energy and mass. To determine these independent unknowns, two measurements must be made. The spectrometer resolves this degeneracy, with a 7.6-kG dipole magnet to disperse the particles in momentum before they are detected, enabling the position of the particle event in the detector plane to be used as one measurement and the strength of the detection signal as the second. For example 3-MeV protons, 1-MeV tritons, and 3-MeV alphas follow the same path through the magnetic field, but they deposit quite different energies in a charged-coupled-device (CCD) detector or make different-sized tracks

in CR-39 plastic film.² Thus, the two independent measurements necessary to determine mass and energy are provided. Figure 1 shows the layout of the proposed magnet and detector system.

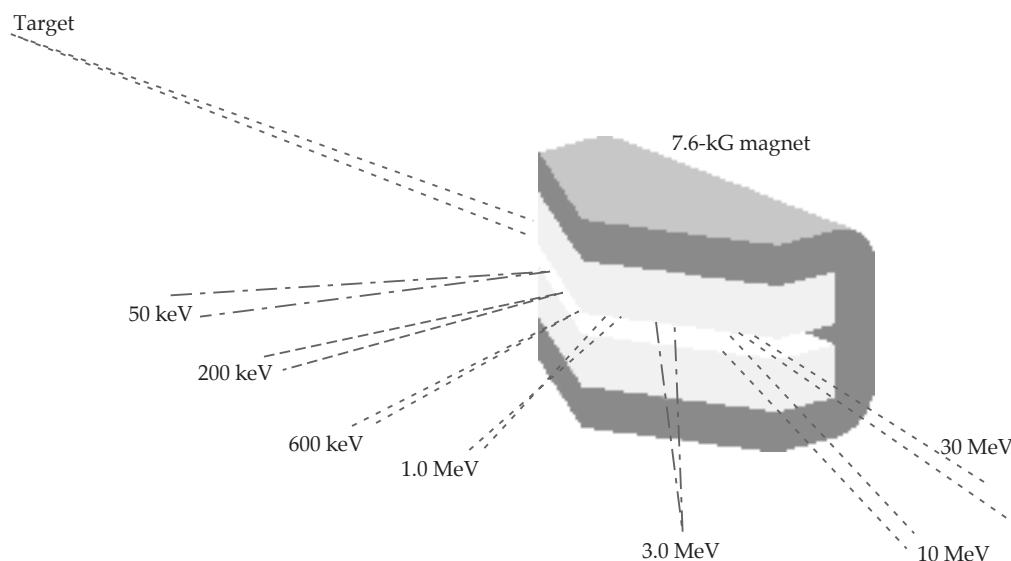
Spectrometer Design

The design of the magnet was driven by the need to view a particle spectrum from 1-MeV protons up to 10.6 MeV, to maximize the particle signal, and to be compatible with the UR Omega experimental facility. From such considerations, the 7.6-kG Nd–Fe–B dipole magnet shown in Figure 2 was constructed by Dexter Corporation.³ The pentagonal shape was necessary to allow the magnet to be positioned close to the target without obstructing the laser beams. The magnet has a 2-cm gap with better than 2% field uniformity in its central region. Use of 1.5-cm-thick shunts to smooth edge fields reduces fringing fields to 50 G at 7 cm from the magnet.

Instrumentation

Various detectors are being considered for the focal plane of the spectrometer. CR-39 track detectors are being used in the development of this diagnostic to establish its utility with minimum development effort and to obtain useful data in a radiation and electrically noisy environment. In parallel, a CCD array is being tested as an alternative focal plane detector. Preliminary data will be obtained by placing track detectors and one or two CCDs in the detector

FIGURE 1. Concept for charged-particle spectrometers (CPSs), showing how particles from a target implosion follow different trajectories through a magnet. The magnet separates particles according to momentum/charge. Particle detection and energy measurement (to uniquely identify the species and energy) are accomplished in spectrometer CPS-1 by CR-39 track detectors. CR-39 will also be used initially in a second spectrometer (CPS-2), but the detector will eventually be augmented by CCDs.
(08-00-1198-2441pb01)



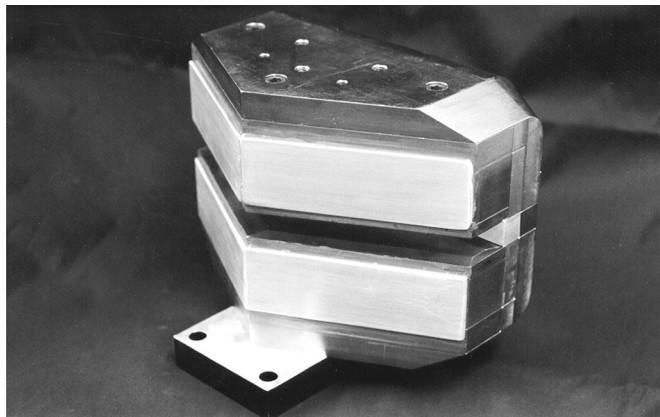


FIGURE 2. One of two identical 7.6-kG magnets fabricated for charged-particle spectrometers CPS-1 and CPS-2. The longest dimension of the magnet is 28 cm, and the gap width is 2 cm. This magnet weighs ~73 kg, and the force between the poles is 2900 kg. Although deployed in the Omega experiment, preliminary studies indicate that it is also suitable for a National Ignition Facility (NIF) charged-particle spectrometer. (08-00-1198-2439pb01)

plane of the magnet. Because the energy resolution of CR-39 film is poor (compared to that of CCDs), the track-based spectrometer will derive its energy resolution from the magnet. The presence of the magnet removes many of the limitations placed on CR-39 detectors in previous studies of knock-on, charged-particle spectra.

CCDs are extremely sensitive detectors of radiation and can easily detect individual charged particles in the MeV range, which deposit 10 to 100 times as much energy as x rays of a few keV. Unlike x rays, charged particles deposit their energy along their entire path through silicon, allowing them to be detected with 100% quantum efficiency. However, because the sensitive depth of a typical back-illuminated CCD is usually no more than 10 to 15 μm , and because light ions in the MeV range have a range of tens to hundreds of microns in silicon, only a fraction of the incident particle energy is recorded by the device. Nevertheless, through the use of well known stopping formulas, such as the Bethe-Bloch formula, and a known value for the sensitive depth, the energy recorded by the CCD is a direct measure of the incident particle energy for a given particle type.

The positioning of a particular CCD in the dispersed particle beam exiting the magnet determines the energy window that it will see, as shown in Figure 1. Within this restricted energy window, it is possible to uniquely attribute every particle event to a proton, deuteron, triton, or alpha at a specific

energy, breaking the degeneracies that existed without the magnet (where the detector would see all particles at all energies).

The Integrated System

Figure 3 is a diagram of the integrated magnet and CCD system. The support module mounted to the vacuum chamber wall allows the magnet entrance slit to be placed as close as 60 cm from the target. Much of the structure volume and region outside the structure, between the magnet and target, is filled with lead-impregnated, borated polyethylene (Pb-B-PE) to thermalize and capture a substantial fraction of the copious direct and scattered neutrons and gammas generated by the target. A beam dump is incorporated to minimize the number of scattered neutrons and gammas from the direct line of sight. For high-yield shots, the entire magnet and CCD system can be retracted, whereas for low-yield shots, the magnet entrance slit is adjustable up to 2 cm wide and 1 cm high. The slit is covered by a light-tight, 25- μm Be window to prevent laser and other light sources in the visible and near-visible range from flooding the detectors. In addition, this window (and other insertable windows) will allow the entire diagnostic system to maintain a vacuum separate from that of the target chamber, enabling easy access into the diagnostic area when maintenance is required. Seven 512×512 CCDs are placed in the exit plane, as shown, to cover the

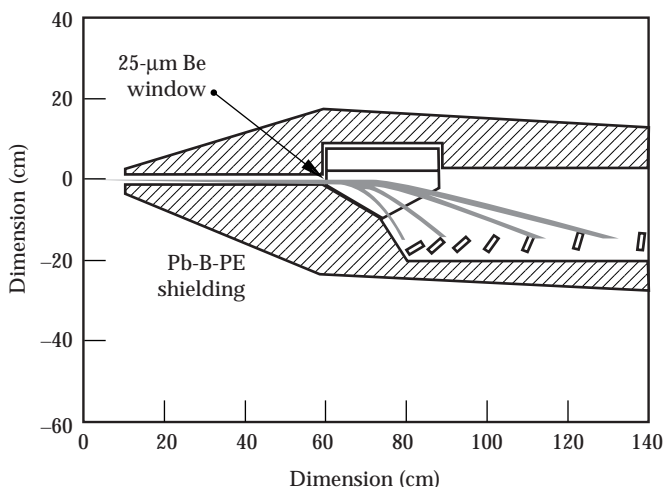


FIGURE 3. The CCD system, with approximate dimensions shown in centimeters. To minimize direct and scattered neutron and gamma noise, large amounts of Pb-B-PE shielding will be incorporated. (08-00-1198-2442pb01)

energy range from 1-MeV protons up to 10.6-MeV tritons. Each CCD is cooled to about -20°C using thermoelectric coolers. The CCDs and their electronics are custom configured to allow the arrays to be placed as close together as possible, minimizing dead space. Data is transferred via fiber-optic cables to minimize electronic pickup.

Predicted Performance

Energy Resolution

The energy resolution of this device may be determined by either the detectors or the magnet. A conservative estimate puts the total CCD resolution at better than 5%. For a slit width of 5 mm, the magnet resolution varies from 1% at low energies to 9% at high energies. For this and smaller slit widths, the magnet provides resolution comparable to that of the CCD. With CR-39 track detectors at the focal plane, the mass is well determined, but there is little energy information, so the magnet resolution dominates.

Operating Yield

For lower-yield experiments, the diagnostic will operate at 60 cm from the target with a 1-cm-high by 2-cm-wide entrance slit, giving a solid angle of 4.4×10^{-5} steradians. At a yield of 10^9 deuterium-tritium (DT) neutrons and a ρR of 10 mg/cm^2 , ~ 100 knock-ons will be detected. When the neutron yield is 10^{13} , a 1-cm-high by 1-mm-wide magnet entrance slit placed at the vacuum wall (160 cm from the target) will result in detection of 10^4 knock-ons when $\rho R = 10 \text{ mg/cm}^2$. This diagnostic can thus span four orders of magnitude in DT yield.

Signal-to-Noise Ratio

The main sources of noise in the system will be from the 14-MeV neutrons and their associated gammas—both direct and scattered. Because of the complex nature of the interactions of neutrons with the surrounding target chamber, it is extremely difficult to precisely predict the noise sensitivity of the CCD to this type of radiation environment. To obtain an estimate of the noise levels, however, the CCDs were exposed to 14-MeV neutrons from the MIT Cockcroft-Walton accelerator, and an “effective” neutron sensitivity of 2×10^{-3} was obtained. A simple calculation of the number of direct neutron interactions with the sensitive region of the CCD predicted a sensitivity lower by a factor of 20, and we believe that the discrepancy is

caused by neutron-induced gamma interactions. However, because most of these interactions produce a small response in the CCD, the events will fall below the charged-particle signal levels of interest, and they may be rejected.

Furthermore, the magnet provides an additional means of noise rejection. Because each CCD is restricted to viewing a narrow particle-energy window by virtue of its position in the dispersed particle beam, any noise events that occur outside the designated energy window can be discarded. Thus, a calculation of the instrument signal-to-noise ratio using the neutron data must take into account the spectral quality of neutron interactions, and not just the absolute sensitivity. In addition, Monte Carlo simulations and experimental measurements have indicated that 60 cm of Pb-B-PE shielding attenuates the neutron flux by more than a factor of 100.

From these considerations, the signal-to-noise ratio for a DT yield of 10^{11} and $\rho R = 10 \text{ mg/cm}^2$ with the $5\text{-mm} \times 1\text{-cm}$ magnet slit at 60 cm from the target can be calculated. For the 512×512 CCD in the high-energy part of the dispersed beam, 350 tritons (from 6.2 to 10.6 MeV) and 200 deuteron knock-ons (from 9.3 to 12.5 MeV) will be detected. The number of neutron and associated gamma events in these ranges, which were predicted on the basis of CCD neutron measurements, give signal-to-noise ratios of 160:1 for tritons and 400:1 for deuterons.

CCD Damage

While testing the response of 512×512 CCDs to protons, alphas, and neutrons, we have seen an increase in the dark-current level of individual pixels with irradiation levels of $\sim 10^9/\text{cm}^2$, probably due to single-hit damage. On a cooled device that is read out rapidly, the effects of such increased dark current are negligible. The levels of irradiation on the Omega chamber are expected to be much less than those to which the device has already been exposed.

For CR-39 plastic track detectors, noise and damage are minor concerns solved by care in handling and etching the material. This fact makes CR-39 a good choice for demonstrating the utility of the technique during the test phase.

Testing the Technique

During the charged-particle spectrometer’s design and construction, tests were conducted of the response of various components to charged particles produced in fusion reactions and the chamber environment of radiation and electrical noise. The first tests employed

small accelerators to produce the charge particles of interest. Both CR-39 and CCD detectors were exposed to protons in the range from 1 to 14 MeV. For CR-39, our tests helped in developing etching and imaging techniques, which gave good sensitivity and reliability for measuring track number and size distributions. The track size distributions were calibrated with particle energy, and automatic scanning, sizing, and counting algorithms were developed.⁴ Similar tests on CCDs established their utility for determining particle energy and mass. Tests on the CCD arrays provided confirmation of the calculated response to charged particles and calibrated them.⁵

Tests were then carried out on fusion implosion experiments, beginning with CR-39 exposed to DD and DT implosions at the LLNL Nova facility. Track sizes consistent with those obtained for accelerator exposures, as well as consistent with the yield observed in neutron diagnostics, gave us confidence in CR-39 as a detector. The DT exposures were dominated by neutron-induced tracks, which made clear the need for good shielding in the spectrometer design.⁴ Tests of the CCDs on fusion experiments were carried out at the UR Omega facility. These tests demonstrated that neutron-induced noise could be reduced by shielding

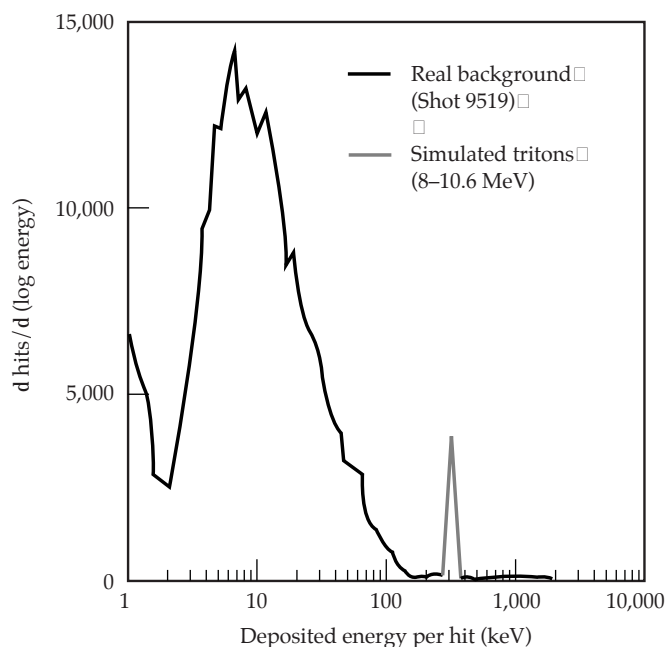


FIGURE 4. Simulated CCD spectra. To estimate what data may actually look like for various CCDs in the magnet-based spectrometer during real shots, calculated spectra for particles of interest were superposed on an actual noise spectrum taken during an Omega DT shot with neutron yield = 4.1×10^{11} . The plot represents the expected spectrum at an appropriate CCD position. (08-00-1198-2443pb01)

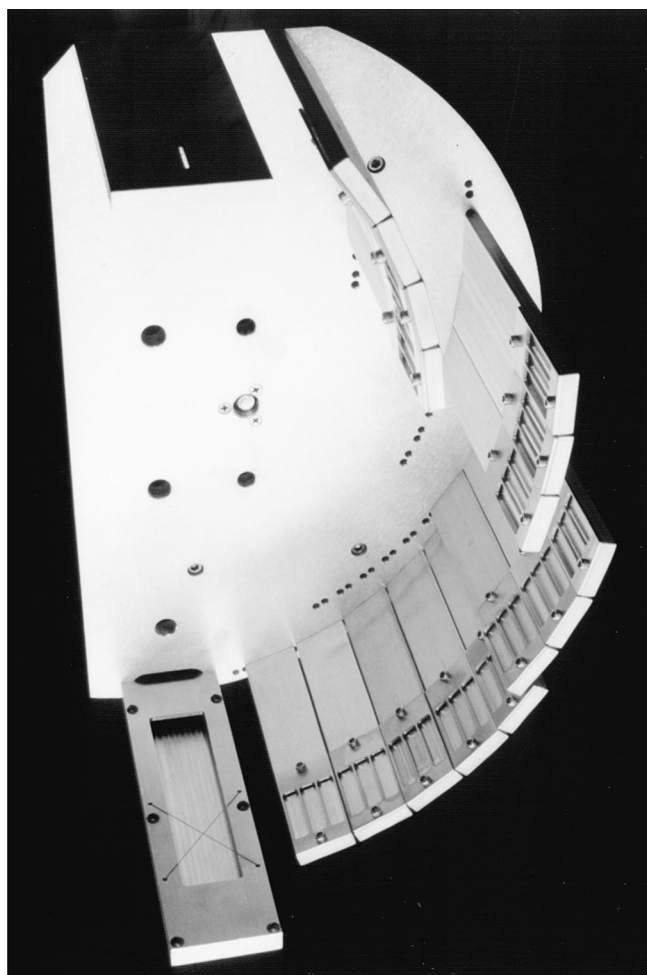


FIGURE 5. The CR-39 detector holder (seen from below) for CPS-1. Fifteen finger plates that support the CR-39 film are assembled in four rows. At the top of the picture is a small, adjustable entrance slit. On the bottom, a finger plate with crossed wires holds x-ray film used to monitor alignment. (08-00-1198-2444pb01)

that would fit within the space available between the laser beams. Detection of fusion charge particles in the presence of this background was simulated using the measured neutron-induced background and adding accelerator-produced, charged-particle data, as shown in Figure 4. The detection of charged particles from a fusion implosion must await the installation of CCDs in the focal plane of the spectrometer.

Full systems tests with two magnets have been carried out on the UR Omega facility using CR-39 as the focal plane detector. A holder shown in Figure 5, which permits easy and reproducible positioning of the CR-39 film in the focal plane of the magnet, was constructed. Exposures have been obtained with DD, D³He, and DT implosions. An example of the performance of the magnet and CR-39 in sorting out

the multiple species from a D^3He exposure is shown in Figures 6 and 7. In Figure 6, the mix of alphas, tritons, and protons can be seen in the different track sizes. The histogram in Figure 7 demonstrates identification and counting by the automated system. Typical DT α , DD p, DD t, D^3He p, and knock-on spectra from these tests are shown in Figure 8. Parameters such as yield, ion temperature, and areal density can be extracted from analyses of these spectra and compared with such parameters obtained by other techniques. The details of analyses and comparisons will be the subject of a future paper.

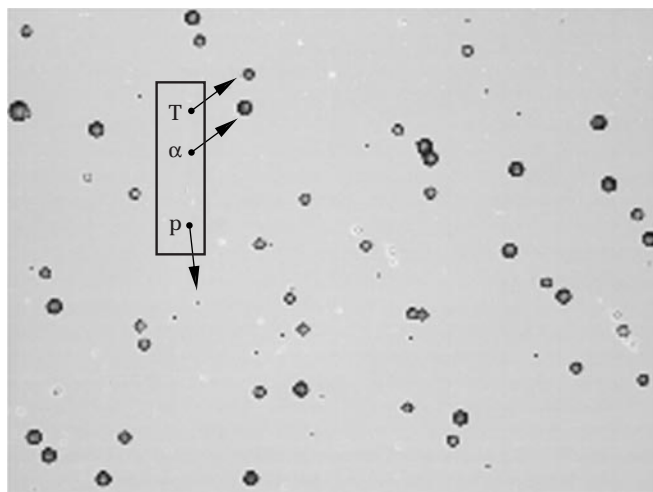


FIGURE 6. DD proton, DD triton, and D^3He alpha tracks in CR-39 from Shot 11585 with a D^3He target. This piece of CR-39 was positioned at finger D5 in the spectrometer, behind a $6\text{-}\mu\text{m}$ Al filter. The $\sim 3.3\text{-MeV}$ DD protons and $\sim 1.1\text{-MeV}$ DD tritons have the same position on the focal plane of the magnet. In addition, due to the energy spread of D^3He alphas (some having energies down to 3.3 MeV), all three types of particle actually appear at this position. However, each particle type can be distinguished easily by its diameter, which is a function of stopping power. This image emphasizes a key concept of the new spectrometer: different charged fusion products with the same magnetic paths have very different stopping powers, allowing unique particle identification.

(08-00-1198-2440pb01)

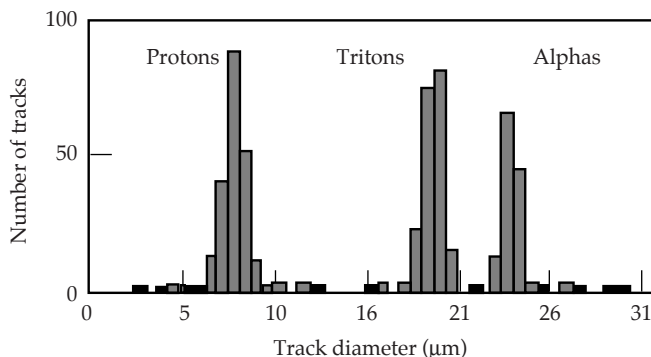


FIGURE 7. A track diameter histogram for the “triple degeneracy” position around the region shown in Figure 6. In this region, DD protons, DD tritons, and some lower-energy D^3He alphas all have the same magnetic paths. However, their differing stopping powers allow each particle type to be uniquely identified. At these energies (3.3 MeV for protons, 1.1 MeV for tritons, and 3.3 MeV for alphas), the alphas have the largest stopping power, and the protons the smallest. (08-00-1198-2445pb01)

Conclusions

A novel diagnostic for laser fusion implosions has been developed through a collaboration of LLNL, MIT, and UR scientists. The technique of charged-particle spectroscopy employs a permanent magnet spectrometer and permits the use of various detection techniques to measure the spectra of charged, energetic nuclear reaction products emitted during the fusion implosion. Properties of the fusion plasma, such as yield, areal density, temperature, and symmetry, may be inferred from the charged-particle spectra. Testing of the technique on fusion implosions has successfully demonstrated its utility as a diagnostic tool for these fusion parameters. Qualitative agreement with other yield measures has been demonstrated. Detailed analyses and comparisons will be the subject of a future paper.

Notes and References

1. R. D. Petrasso, et al., *Phys. Rev. Lett.* **77**, 2718 (1996).
2. A. P. Fews, *NIM* **B71**, 465–478 (1992).
3. Dexter Corporation, Magnetic Materials Division (PERMAG), 48460 Kato Rd., Fremont, CA, 94538.
4. T. W. Phillips et al., *Rev. Sci. Inst.* **68**, 596 (1997).
5. C. K. Li et al., *Rev. Sci. Inst.* **68**, 593 (1997).

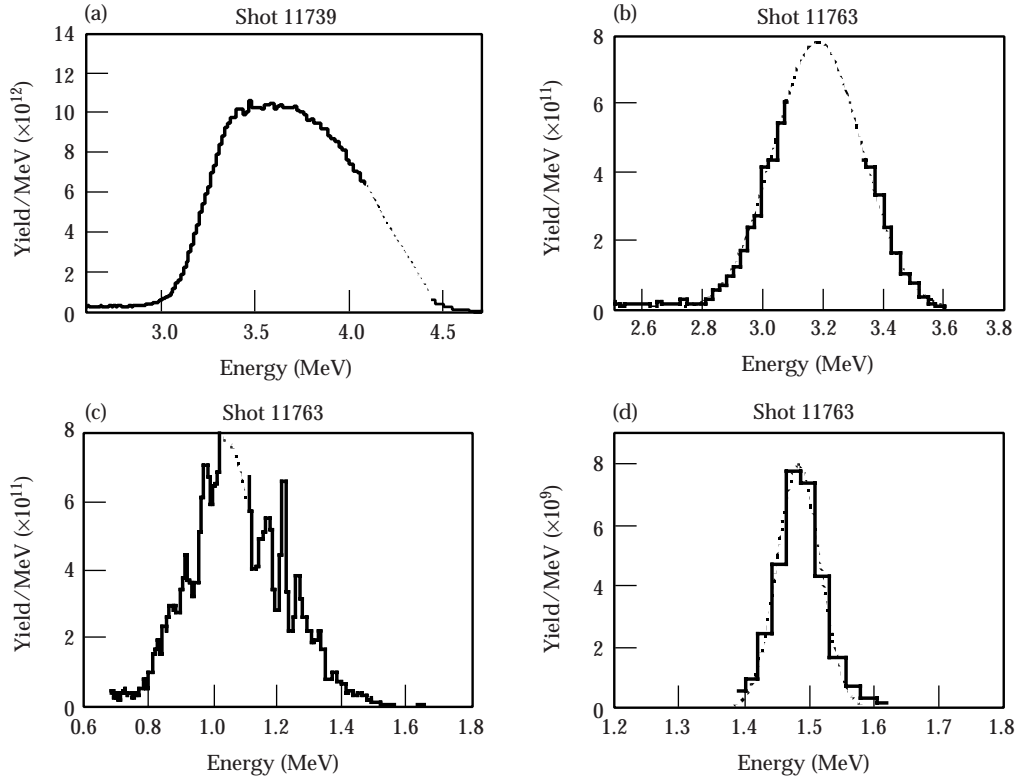


FIGURE 8. Typical spectra obtained from DT, DD, and D^3He shots on Omega with CR-39 detectors in the spectrometer focal plane. (a) DT alpha spectrum from shot 11739. From the Gaussian fit, the mean energy was 3.67 MeV ($\pm \sim 1\%$) with a width of 0.39 MeV, while the yield was 1.01×10^{13} ($\pm 15\%$). (b) DD proton spectrum from Shot 11763. From the Gaussian fit, the mean energy was 3.18 MeV ($\pm \sim 1\%$) with a standard deviation of 0.15 MeV, while the yield was 2.89×10^{11} ($\pm 15\%$). In this instance, the proton “line” happened to straddle the 3-mm dead space between finger positions D3 and D5, as indicated by the gap in the spectrum. (c) DD triton spectrum from Shot 11763. From the Gaussian fit, the mean energy was 1.08 MeV ($\pm \sim 1\%$) with a standard deviation of 0.15 MeV, while the yield was 2.55×10^{11} ($\pm 15\%$) (consistent with the proton yield). (d) D^3He proton spectrum from Shot 11763. From the Gaussian fit, the mean energy was 14.85 MeV ($\pm \sim 1\%$) with a standard deviation of 0.33 MeV. The yield was 6.57×10^9 . The width of the peak is slit-resolution-limited, because the physical width of this proton line (2 mm) is comparable to the slit width (1 mm). The protons were ranged through 1000 μm and 1100 μm of aluminum to make them easily detectable in CR-39. (08-00-1198-2446pb01)

FUDGE: A HIGH-BANDWIDTH FUSION DIAGNOSTIC FOR THE NATIONAL IGNITION FACILITY

M. J. Moran

Introduction

The fusion diagnostic gamma-ray experiment (FUDGE), essentially a magnetic Compton spectrometer combined with a Cherenkov detector, is a high-bandwidth fusion diagnostic for the National Ignition Facility (NIF). Nuclear diagnostics will play a critical role in the success of future inertial confinement fusion (ICF) experiments at the NIF. Diagnostics must go beyond measurement of fusion yield to characterizing details of the fusion burn. Imaging and temporal measurements are important because they provide data for comparison with theoretical predictions. The comparisons show how details of fusion behavior depend on target and experiment design. These data will serve as the basis of an iterative process of design and experiment that will lead to optimization of fusion performance.

Neutron and x-ray images are important for understanding how to compress an ICF target to the desired size and shape. Images provide a direct indication of the integrity of the compressed target during the fusion burn. Such data can give clear indications of high-quality performance and can also provide evidence of imperfect target compression in unsuccessful experiments. Image data go far beyond indications of success or failure by indicating how the spatial distributions of the source might be related to performance in experiments. These results can suggest specific approaches for improving performance for subsequent experiments.

Burn-history measurements of emission rate can serve as indicators of the instantaneous source temperature and other details of behavior that are not evident in time-integrated images. In addition to following the instantaneous reaction rate, the data are highly sensitive to instantaneous temperature (rate $\propto T^5$). When compared with images, the reaction rate can be used to

infer source temperature, or to provide independent indication of unexpected behavior. Again, as with images, time-dependent behavior can help to suggest approaches for improving system performance.

The NIF will require new burn-history diagnostics because the techniques that have been used traditionally will no longer be feasible. The relatively low fusion yields of previous experiments have made it possible to place detector components a few centimeters from the source, where temporal dispersion of neutron signals can be small.¹ In addition, streak cameras could be located a few tens of centimeters from the source without suffering serious radiation damage. At the NIF, physical constraints and high radiation doses in the target chamber will force diagnostic components to be located at distances of the order of meters from the source, where temporal broadening of neutron signals will mask the source pulse shape.

Gamma-Ray Diagnostics

One promising approach to burn-history measurements at the NIF is with diagnostics based on the 16.7-MeV γ ray associated with (D,T) fusion. This γ ray is ideal for measuring (D,T) fusion reaction rates because it is free of the temporal dispersion that frustrates neutron-based measurements. The presence of this γ ray is well known, although associated spectrum and "branching ratio" have proven difficult to measure accurately. The most recent measurement finds for ${}^3\text{H}(\text{d},\gamma){}^5\text{He}/{}^3\text{H}(\text{d},\alpha)\text{n}$ a branching ratio of 1.2×10^{-4} , with the γ rays in two broad lines at 11.5 (FWHM ≈ 7 MeV) and 16.7 (FWHM ≈ 2 MeV) MeV (Ref. 2). This result is within the range of 2×10^{-5} to 3×10^{-4} that had been reported in previous measurements. The rather small branching ratio means that γ -ray measurements of (D,T) fusion reaction rates are practical only for intense short-pulse experiments. For weaker sources, neutron

backgrounds make it extremely difficult to extract the desired γ -ray signal.

Several approaches have been used previously for designing a fusion γ -ray diagnostic. Filtered and heavily shielded scintillation detectors have been used in tokamak experiments.³ Cherenkov detectors and gas-Cherenkov detectors have been discussed, sometimes in tandem with magnetic Compton spectrometers.^{4,5,6} These attempts were often frustrated by small signals in the presence of large neutron backgrounds. With the large emission rates anticipated for NIF experiments, it becomes possible to choose a γ -ray diagnostic design having an excellent signal-to-background ratio with high-bandwidth signal recording.

Three basic considerations constrain the design of a fusion γ -ray diagnostic: (1) the instrument should provide sufficient energy discrimination to eliminate signals from lower-energy γ rays generated by $(n,n'\gamma)$ and other nuclear reactions; (2) the diagnostic also must feature some form of energy dispersion, as the spectral resolution must be achieved in single-shot measurements; and (3) the detector should be fast and have sufficient sensitivity to measure the rays. These requirements can be met by a magnetic Compton spectrometer with a Cherenkov detector (i.e., the FUDGE).

In a Compton spectrometer, γ rays scatter electrons from a (γ,e^-) converter target. The recoil electrons, after energy selection in a sector magnet, are detected in a high-gain, high-bandwidth Cherenkov detector. The three components—the (γ,e^-) converter, the sector magnet, and the Cherenkov detector—can be designed for optimum performance from the overall system.

The (γ,e^-) converter, although very simple, offers choices with respect to scattering cross section and type of material. At a first glance, the rather large total cross section associated with pair production would suggest that thin, high- Z targets be used as the converter (Z is the atomic number of the target material). However, multiple scattering, energy loss, and loss of spectral signature are significant disadvantages for pair production. Pair production increases with Z^2 , but so does multiple scattering. Energy loss in dense, high- Z materials compounds the undesirable effects of multiple scattering. The flat energy spectrum of electrons from pair production reduces the benefits that might be obtained from spectral resolution.

Compton Scattering

Compton scattering is a (γ,e^-) converter mechanism that, despite its smaller total cross section, lends itself nicely to a fusion- γ diagnostic. The differential cross section (i.e., the Klein–Nishina formula) peaks in the forward direction with an angular width of about $1/E\gamma$. For 16.7-MeV γ rays, the majority of the recoil electrons are in a narrow (width $\approx 3^\circ$), forward-directed cone

with energies near that of the original γ ray. Thick, low- Z Compton converters maximize the conversion efficiency while minimizing the effects of multiple scattering.

Figure 1 shows a comparison of (γ,e^-) conversion for 16.7-MeV photons in targets that optimize the efficiency for pair production and Compton scattering. The pair-production target is 0.5 mm of Pb, while the Compton target is 5 mm of Be. The distributions are calculated with the Gluckstern et al.⁷ formulation for pair production and the Klein–Nishina formula⁸ for Compton scattering. In the model used here, the targets are divided into about ten thin layers. Electrons scattered from individual layers are transported, with energy loss⁹ and multiple scattering¹⁰ used to estimate contributions to the overall conversion flux from the converter. The distribution has 0.5-MeV energy increments and 3° angular bins.

The results show that the larger total cross section of pair production produces a distribution that cannot be collected efficiently either in space or in energy. The total cross section for Compton scattering, although about 16 times smaller, is directed into a narrow beam with good energy definition. The forward-directed peak is about twice as intense as the pair-production peak. Thus, in a diagnostic where good energy discrimination and well defined trajectories are required, Compton scattering is the desirable choice.

Magnetic Analysis

The recoil electron beam must be collected and energy analyzed efficiently in order to achieve good performance. This function is accomplished with a

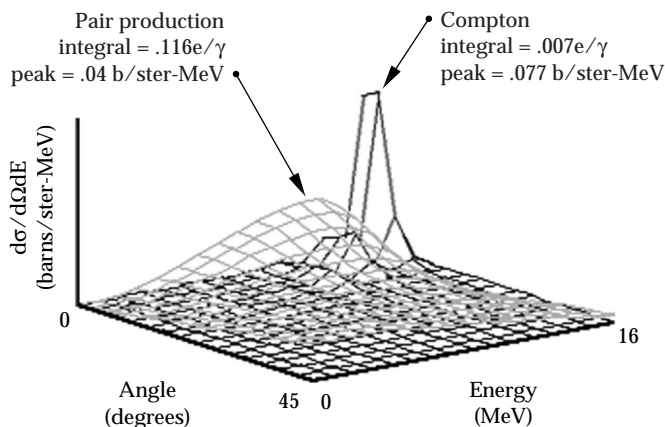


FIGURE 1. Scattered electron distribution from 0.5 mm of Pb compared with that from 5 mm of Be. The Pb, with higher Z , has a larger total cross section from pair production and greater elastic scattering. Compton scattering in the Be, with similar electron areal density, emphasizes forward scattering in a peak with good energy definition. (08-00-1198-2237pb01)

sector-magnet dipole.⁴ With a deflection angle of 30° , spectral dispersion can isolate the desired broad band at about 16 MeV. The deflection trajectories also function as a collecting lens. With slight non-normal incidence on the magnet, the magnet functions as a cylindrical lens in the vertical direction. Figure 2 illustrates the electron optics of the system.

This compact design has sufficient energy resolution to collect the desired electron energies, while rejecting lower-energy electrons strongly. Figure 2 shows that 8-MeV electrons will be very strongly deflected, and electrons with still lower energies will be unable to exit the magnet assembly. Because most of the photon background will have energies below 8 MeV, the magnet will be an effective background shield.

System Performance

The data in Figure 1 can be used to estimate the overall (γ, e^-) Compton conversion efficiency. Assuming a converter with an area of 2 cm^2 located 2.5 m from the source, the solid-angle fraction is 1.25×10^{-6} . The recoil electron distribution has a peak with widths of about 6° and 0.5 MeV, but the peak represents only about 15% of the total cross section. Thus, according to Figure 1, Compton conversion into the collimated peak has an efficiency of about $10^{-3} e^-/\gamma$. The sector magnet should be able to collect this beam with an efficiency greater than 10%. Combining these factors gives an overall

FIGURE 2. A simple 30° deflection sector dipole magnet can collect recoil electrons efficiently. The non-normal angle of incidence acts as an out-of-plane cylindrical lens to enhance electron collection. (08-00-1198-2238pb01)

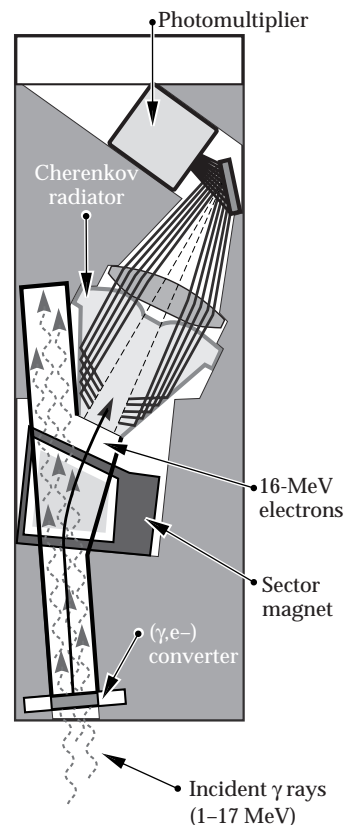
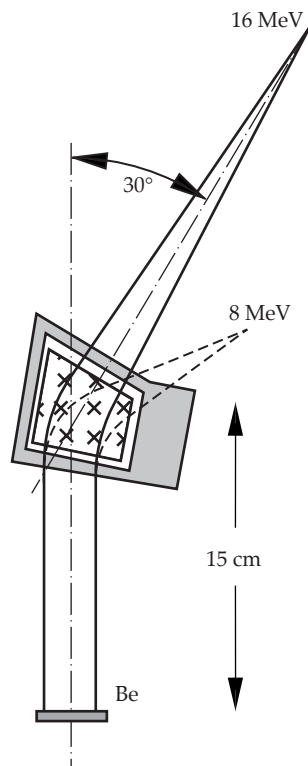


FIGURE 3. The overall FUDGE assembly can be compact. Here, a photomultiplier detects Cherenkov photons from energy-selected Compton electrons. The Cherenkov radiator is not exposed directly to the source, and “sees” only the deflected electrons. The photomultiplier is shielded heavily from the incident γ rays. (08-00-1198-2239pb02)

efficiency of about 1.25×10^{-10} electrons/16.7-MeV γ . This result can be used to determine the viability of the diagnostic. The system can produce a useful signal only if there is a statistically significant number of electrons. If we take 100 as the minimum number of electrons that can provide a measure of burn width, then the diagnostic is viable for (D,T) fusion neutron yields greater than about 10^{16} .

The nature of the signal depends on the method used to detect the electrons. A Cherenkov radiator optimized for electrons in this energy range can produce more than 500 visible photons per electron.¹¹ If the photons are detected with a fast MCP, then the signal will be a current pulse that can be recorded. Figure 3 illustrates a compact design for a FUDGE diagnostic with a microchannel plate (MCP) as the photodetector. With 100 electrons, an MCP gain of 10, a pulse width of 500 ps, the pulse will have a peak of about 2 A. This value seems very large for the signal, but it still represents only 100 initial Compton electrons. MCP response times today can be as short as 140 ps (Ref. 12), so burn widths of a few hundred picoseconds can be recorded with this approach.

Higher-bandwidth data can be recorded with a streak camera, at some possible expense in sensitivity. The challenge with this approach is to image enough of the Cherenkov photons onto the streak-camera slit to have a statistically significant measurement. We can

estimate the overall system efficiency: assuming a photocathode efficiency of 10%, approximately 1000 photons must be imaged onto the slit. The assumption above provides 5×10^4 photons from the Cherenkov radiator, so the Cherenkov image must have a transport efficiency of about 0.2%. This efficiency is feasible with a 50- μm streak camera slit, $f/3$ optics, and a 1-cm beam of electrons incident on the Cherenkov cone. Thus, incorporation of a streak camera might not compromise the overall system efficiency.

The estimate above only demonstrates the feasibility of designing a diagnostic for high-bandwidth recording of a fusion γ -ray signal. This is a compound system with multiple convolved distributions, so detailed predictions of system performance are difficult to calculate. This is a case where, ultimately, the performance of a FUDGE diagnostic must be calibrated on well characterized γ -ray sources.

Conclusion

FUDGE will bring together several kinds of issues that relate to ICF development at the NIF. The FUDGE method will use the high yields of NIF experiments to provide high-bandwidth measurements of fusion reaction history. When compared with fusion-neutron diagnostics, FUDGE data also will represent new measurements of absolute fusion cross sections and branching ratios. In this way, FUDGE will contribute to the

optimization of performance in ICF experiments and also will help advance our knowledge of the underlying fusion cross sections. These experiments should be excellent examples of doing science at the NIF.

Notes and References

1. R. A. Lerche, D. W. Phillion, and G. L. Tietbohl, *Rev. Sci. Instr.* **66**, 933 (1995).
2. J. E. Kammeraad, J. Hall, K. Sale, C. A. Barnes, S. E. Kellogg, T. R. Wang, et al., *Phys. Rev. C* **47**, 29 (1993).
3. S. S. Medley, A. L. Roquemore, and F. E. Cecil, *Rev. Sci. Instr.* **63**, 4857 (1992), and references therein.
4. M. J. Moran, *Rev. Sci. Instr.*, **56** 1067 (1985).
5. K. W. Wenzel, R. D. Petrasso, D. H. Lo, C. K. Li, J. W. Coleman, and J. R. Lierzer, *Rev. Sci. Instr.* **63**, 4840 (1992).
6. R. A. Lerche, M. D. Cable, and P. G. Dendooven, 12th International Conference on Laser Interaction and Related Phenomena, Osaka, Japan, (1995), and R. A. Lerche and M.D. Cable, *ICF Quarterly Report* **6**(3), 115, Lawrence Livermore National Laboratory, Livermore, CA, UCRL-LR-105821-96-3 (1996).
7. R. L. Gluckstern and M. H. Hull, Jr., *Phys. Rev.* **90**, 1030 (1953).
8. A. T. Nelms, *National Bureau of Standards Circular* 542 (1953).
9. L. Pages, E. Bertel, H. Joffre, and L. Sklavenitis, *Atomic Data* **4**, 1 (1972).
10. E. Segrè, *Experimental Nuclear Physics*, **1**, John Wiley & Sons (1953).
11. K.-P. Lewis, M. J. Moran, and J. Hall, *Rev. Sci. Instr.* **63**, 1988 (1992).
12. We have demonstrated this response time with measurements of a subpicosecond laser using a Hamamatsu 2566 MCP and Tektronix SCD5000 transient digitizer.

PROPAGATION OF REALISTIC BEAMS IN UNDERDENSE PLASMA

D. E. Hinkel

L. V. Powers

R. L. Berger

C. H. Still

A. B. Langdon

E. A. Williams

Introduction

The study of parametric instabilities¹ has long been a topic of interest in laser–plasma interactions. Reliable prediction of experimental results requires detailed knowledge of the plasma characteristics (density, temperature and flow profiles) as well as the laser beam structure (phase and intensity modulation information). Hydrocodes such as LASNEX² and experimental measurements^{3–5} and laser-beam propagation codes⁶ provide relevant information about beam characteristics.

In this article, we examine two physical mechanisms that demonstrate the effect of beam structure on its propagation through underdense plasma. First, we discuss the effect of transverse plasma flow on beam deflection. When there is plasma flowing across a beam, the density depressions created by the ponderomotive pressure of the light wave are swept downstream in the flow direction, and the light, which is refracted into the density depression, moves downstream as well.

We present a simple analysis of this problem, which shows that the beam deflection rate scales with the figure of merit $Q \equiv (v_0/v_e)^2 (n/n_c)(1 - n/n_c)^{-1}$, where v_0 (v_e) is the electron quiver (thermal) velocity, n is the electron plasma density, and n_c is the critical plasma density at which light reflects ($n/n_c = \omega_{pe}^2/\omega_0^2$, where ω_{pe} is the electron-plasma frequency and ω_0 is the light-wave frequency). In previous work by Ghosal and Rose,⁷ three different expressions for the beam deflection rate were derived—for the subsonic, near-sonic, and supersonic regimes of the transverse flow, respectively. We have derived a more general expression, valid for all transverse Mach numbers M as well as noncircular Gaussian beams, which reduces to the results of Ghosal and Rose⁷ in the three Mach number

regimes with circular beam cross sections. In the limits of subsonic $M < 1$, near-sonic $M \approx 1$, and supersonic $M > 1$ transverse flow, our expression for the beam deflection rate scales as $\bar{v}M/(1 - M^2)^{3/2}$, $1/\bar{v}^{1/2}$, and $1/[M(M^2 - 1)^{1/2}]$, respectively, where \bar{v} is the ion damping decrement.

Recent experiments in gas-filled hohlraums conducted on the Nova laser at Lawrence Livermore National Laboratory (LLNL) show that the laser spot on the hohlraum wall is effectively 150 μm closer to the laser entrance hole (LEH) than in empty hohlraum experiments.³ We show that this spot motion can be interpreted as beam deflection occurring near the LEH by simulating these experiments using F3D,⁸ a fully nonlinear, 3D fluid hydrodynamics code with paraxial light-wave propagation. A necessary component in effectively modeling the experiment is utilizing as input to F3D the beam structure of the unsmoothed Nova laser beams⁶ as well as realistic plasma profiles generated by LASNEX. Our modeling shows that an unsmoothed Nova beam undergoes beam deflection at the LEH, which results in an effective shift in the beam centroid toward the LEH. When the beam is spatially smoothed by applying random phase plates (RPPs),^{8,9} the centroid shift is reduced to within laser pointing accuracy. These results, which simulate the actual beam profiles at the wall, are in qualitative agreement with experiments, where the x-ray emission pattern was measured.

The second physical mechanism we address in this article is the effect of beam structure on channel formation by ultraintense laser light, a situation directly applicable to the hole-boring beam in the fast ignitor concept.¹⁰ We have modified F3D to include relativistic corrections and the effect of charge separation.¹¹ In 3D simulations of a Gaussian beam with peak intensity $5.7 \times 10^{17} \text{ W/cm}^2$ and a waist of 15 μm , or of an $f/3$ beam with the same amount of input power as the

Gaussian, the beam creates a channel through 1 mm of plasma with initially uniform density $n = 0.1n_c$ for the Gaussian beam or through 0.4 mm for the $f/3$ beam in a time $t = 15$ ps. However, when random phase aberrations are superposed on an $f/3$ laser beam, so that asymptotically the beam is $f/3$ but at best focus it is no longer diffraction limited (its spot size is $15 \mu\text{m}$), a channel does not form through $400 \mu\text{m}$ of plasma at density $n = 0.1n_c$ in a time $t = 30$ ps.

After this introduction, the second section of this article addresses beam deflection in two subsections: first we present our analysis, then the results of our modeling. The third section is devoted to channel formation of ultraintense laser light. In the fourth section, we conclude with a discussion of our results.

Laser-Beam Deflection by Transverse Plasma Flow

Beam deflection has been a topic of vigorous interest in the past few years because of its potential to degrade the implosion symmetry of targets in gas-filled hohlraums. In 1982, Short, Bingham, and Williams¹² analyzed the plasma dispersion relation with transverse flow, and showed that the spatial growth rate was enhanced and peaked at values of M less than about unity. A series of Nova gas-filled hohlraum experiments inspired H. A. Rose¹³ to suggest that transverse plasma flow could explain the observed deflection of backscattered light. Hinkel, Williams, and Still¹⁴ simulated beam deflection for laser beams with spatial (RPP) and temporal (SSD¹⁵) beam smoothing. They showed that RPP beams deflect both supersonically (by forward Brillouin scatter between different k -components of the RPP beam) and subsonically as well, and that SSD mitigates the deflection. In this present work, we extend our previous work by simulating unsmoothed beams, and by deriving an analytic expression that is valid for circular and elliptic Gaussian beams for all values of the transverse flow Mach number M . Our present work, in the appropriate limits, is in agreement with that of Ghosal and Rose,⁷ who performed a linear analysis of beam deflection. In addition to the gas-filled hohlraum experiments on Nova, there have been exploding foil experiments performed on Nova⁴ and on the Janus laser⁵ at LLNL that show an intensity-dependent beam deflection.

The equations of motion governing the coupling of the laser light to the density perturbation¹ in the paraxial approximation are

$$(2ik_0\partial_z + \nabla_\perp^2)\psi = (\omega_{pe}^2/c^2)\delta\bar{n}\psi \quad (1a)$$

and

$$\begin{aligned} & \left[(\partial_t + u\partial_x + v)(\partial_t + u\partial_x) - C_s^2\nabla_\perp^2 \right] \delta\bar{n} \\ &= \frac{1}{4} C_s^2 (v_0/v_e)^2 \nabla_\perp^2 |\psi|^2. \end{aligned} \quad (1b)$$

Here, ψ is the light-wave vector potential scaled to its peak value, $\delta\bar{n}$ is the fractional density perturbation, k_0 is the laser wave number, ω_{pe} is the electron-plasma frequency, c is the speed of light, v is the ion damping rate, u is the transverse plasma flow, C_s is the sound speed, v_0 is the electron quiver velocity in the peak light wave electric field, and v_e is the electron thermal velocity. An additional approximation, consistent with the paraxial approximation, is that density perturbations are transverse to the forward-propagating light wave.

Beam Deflection: Analysis

A simple 1D argument demonstrates that the plasma density response is downstream from the light wave when transverse flow is present. Assume that the light wave is legislated, i.e., that ψ is known and given. Then, in steady state, a 1D version of Eq. 1 takes the form

$$\begin{aligned} & \left[(u\partial_x + v)u\partial_x - C_s^2\partial_x^2 \right] \delta\bar{n} \\ &= \frac{1}{4} C_s^2 (v_0/v_e)^2 \partial_x^2 |\psi|^2. \end{aligned} \quad (2)$$

Eq. 2 can be integrated once (for constant u), giving

$$\left[\partial_x - \frac{uv}{C_s^2 - u^2} \right] \delta\bar{n} = -\frac{1}{4} \frac{C_s^2 (v_0/v_e)^2 \partial_x^2 |\psi|^2}{C_s^2 - u^2}. \quad (3)$$

A local density minimum means that $\partial_x(\delta\bar{n}) = 0$, and thus

$$\delta\bar{n}|_{\partial_x(\delta\bar{n})=0} = \frac{1}{4} \frac{C_s^2}{uv} \left(\frac{v_0}{v_e} \right)^2 \partial_x |\psi|^2. \quad (4)$$

In the absence of damping, the minimum of the density profile coincides with the maximum of the ponderomotive potential. Where the density has a local minimum and where $v > 0$ and $u > 0$, we have $\partial_x |\psi|^2 < 0$. Thus, the density well does not line up with the peak in the ponderomotive potential; rather, it is displaced downstream from the potential maximum where $\partial_x |\psi|^2 < 0$.

It now remains to show that the light wave is refracted into the displaced density well, thereby moving downstream as well. We obtain equations for the

beam centroid and the beam width by taking intensity-weighted moments of Eq. 1a,

$$\frac{\partial^2}{\partial z^2} \langle \mathbf{x}_\perp \rangle = \frac{\partial}{\partial z} \langle \tilde{\mathbf{k}}_\perp \rangle = -\frac{\omega_{pe}^2}{2(k_0 c)^2} \langle \nabla_\perp \delta \bar{n} \rangle, \quad (5a)$$

and

$$\begin{aligned} \frac{\partial^2}{\partial z^2} \langle (\mathbf{x}_\perp - \langle \mathbf{x}_\perp \rangle)^2 \rangle = \\ \times 2 \left\{ \left\langle (\tilde{\mathbf{k}}_\perp - \langle \tilde{\mathbf{k}}_\perp \rangle)^2 \right\rangle - \frac{\omega_{pe}^2}{(k_0 c)^2} \langle (\mathbf{x}_\perp - \langle \mathbf{x}_\perp \rangle) \cdot (\nabla_\perp \delta \bar{n}) \rangle \right\} \end{aligned} \quad (5b)$$

where $\langle \mathbf{x}_\perp \rangle \equiv \int d^2 x_\perp \psi^* \mathbf{x}_\perp \psi$,

$\langle \tilde{\mathbf{k}}_\perp \rangle \equiv \langle \mathbf{k}_\perp / k_0 \rangle = -(i/k_0) \int d^2 x_\perp \psi^* \nabla_\perp \psi$, etc.

Eq. 5a describes the beam centroid motion as a function of propagation distance. The transverse density gradient refracts the light to regions of lower electron density. Eq. 5b governs the beam width as a function of propagation distance. As the beam propagates through plasma, the beam width will increase if diffraction (first term on right-hand side of Eq. 5b) dominates self-focusing (second term on right-hand side of Eq. 5b), and it will decrease if self-focusing dominates diffraction.¹⁶

We envisage three regimes for beam deflection. Well below the critical power for self-focusing, where the beam width is not modified by ponderomotive effects, Eq. 5a can be integrated in the z direction using the unperturbed beam width. In this limit, test calculations using our code F3D show agreement with our analytic results. Approaching critical power, a self-consistent solution of Eqs. 5a and 5b is required to determine the beam deflection rate. Above critical power, a self-consistent solution for the beam width will determine the deflection rate up to the point where beam breakup occurs, beyond which a single-beam model no longer applies.

It is beyond the scope of this present work to self-consistently evolve the beam width. Therefore we shall legislate a beam width and focus our attention on solving Eq. 5a.

We outline the methodology for solving Eq. 5a by first solving for $\langle \delta \bar{n} \rangle$, where, again, the brackets denote an intensity-weighted average. By Fourier transforming Eq. 1b and solving for $\delta \bar{n}(\mathbf{k}_\perp)$, we find that¹⁴

$$\langle \delta \bar{n} \rangle = -\frac{1}{16\pi^2} \left(\frac{v_0}{v_e} \right)^2 \int \frac{d^2 k_\perp k_\perp^2 g(\mathbf{k}_\perp) g(-\mathbf{k}_\perp) / g(0)}{(1-M^2)k_x^2 + k_y^2 + i\bar{\nu} M k_\perp k_x}, \quad (6)$$

where $M \equiv u/C_s$ is the transverse Mach number (here we have assumed that the flow is in the x direction), $\bar{\nu} \equiv \nu/(k_\perp C_s)$ is the ion damping decrement, and $g(\mathbf{w})$ is the Fourier transform of $|\psi|^2$ evaluated at $\mathbf{k} = \mathbf{w}$. Similarly, when the Fourier transform of Eq. 1b is substituted into Eq. 5a, we obtain

$$\begin{aligned} \frac{\partial}{\partial z} \langle \tilde{\mathbf{k}}_\perp \rangle = \frac{i\omega_{pe}^2}{32\pi^2 (k_0 c)^2} \left(\frac{v_0}{v_e} \right)^2 \\ \times \int \frac{d^2 k_\perp k_\perp k_\perp^2 g(\mathbf{k}_\perp) g(-\mathbf{k}_\perp) / g(0)}{(1-M^2)k_x^2 + k_y^2 + i\bar{\nu} M k_\perp k_x}. \end{aligned} \quad (7)$$

Eqs. 6 and 7 can be integrated over angle for any wave field g that can be expanded in a Fourier-Bessel series. However, for definiteness, we assume

$$g(\mathbf{k}_\perp) = \pi \sigma_x \sigma_y \exp[-k_x^2 \sigma_x^2 / 4 - k_y^2 \sigma_y^2 / 4]$$

and

$$\psi(\mathbf{x}_\perp) = \exp[-x^2/(2\sigma_x^2) - y^2/(2\sigma_y^2)],$$

i.e., the beam field is a Gaussian in real space with beam width σ_x in the x -direction and σ_y in the y -direction.

It is then easy to perform the radial portion of the integrands of Eqs. 6 and 7, yielding

$$\langle \delta \bar{n} \rangle = -\frac{1}{8} \left(\frac{v_0}{v_e} \right)^2 \left\{ 1 + \frac{M^2}{2\pi} \frac{\sigma_y^2}{\sigma_x^2} \int_0^{2\pi} \frac{d\theta \cos^2 \theta [\tilde{\alpha}^2 - 1 - M^2 \bar{\nu}^2 (\sigma_x^2 / \sigma_y^2) / 2 - \epsilon^2 \bar{\nu}^2 \cos^2 \theta]}{[1 - (1 - \tilde{\alpha}^2) \cos^2 \theta]^2 + \tilde{\beta}^2 \cos^4 \theta} \right\} \quad (8)$$

and

$$\frac{\partial}{\partial z} \langle \tilde{k}_x \rangle = \frac{\sqrt{2}}{64\sqrt{\pi}} \left(\frac{v_0}{v_e} \right)^2 \frac{n}{n_c} \left(\frac{\omega_0}{k_0 c} \right)^2 \frac{M \bar{\nu} \sigma_y}{\sigma_x^2} \int_0^{2\pi} \frac{d\theta [1 + \epsilon^2 \cos^2 \theta]^{3/2}}{[1 - (1 - \tilde{\alpha}^2) \cos^2 \theta]^2 + \tilde{\beta}^2 \cos^4 \theta}, \quad (9)$$

where $\tilde{\alpha}^2 \equiv (\sigma_y^2/\sigma_x^2)[1 - M^2(1 - \bar{v}^2/2)]$ and $\tilde{\beta} \equiv (\sigma_y^2/\sigma_x^2)M^2\bar{v}$. The above expressions are valid through order \bar{v}^2 , i.e., corrections of order $(M^2\bar{v}^4)$ have been dropped. The beam eccentricity is measured by $\epsilon^2 \equiv \sigma_y^2/\sigma_x^2 - 1$. Note that in the above expression, the component of \mathbf{k}_\perp that is nonzero is that in the flow direction, i.e., \mathbf{k}_x .

If we use the identity $\cos^2 \theta = [1 + \cos(2\theta)]/2$, make the change of variable $\phi = 2\theta$, and integrate about the unit circle by setting $z = \exp(i\phi)$, the expression for $\langle \delta \bar{n} \rangle$ can be determined by summing over the residues inside the unit circle,

$$\langle \delta \bar{n} \rangle = -\frac{1}{8} \left(\frac{v_0}{v_e} \right)^2 \left\{ 1 + \frac{\frac{M^2 \sigma_y^2}{\sqrt{2} \sigma_x^2}}{\left[(1 - \tilde{\alpha}^2)^2 + \tilde{\beta}^2 \right]} \left\{ \left[\frac{\sigma_y^2}{\sigma_x^2} (1 - M^2) - 1 + \epsilon^2 \bar{v}^2 \right] \left\{ \sqrt{2} - \frac{\sqrt{\tilde{\alpha}^4 + \tilde{\beta}^2 + \tilde{\alpha}^2}}{\sqrt{\tilde{\alpha}^4 + \tilde{\beta}^2}} \right\} \right\} + \left[(\tilde{\alpha}^2 - 1) \left(\frac{M^2 \bar{v}^2 \sigma_y^2}{2 \sigma_x^2} - \epsilon^2 \bar{v}^2 \right) + \tilde{\beta}^2 \right] \frac{\sqrt{\tilde{\alpha}^4 + \tilde{\beta}^2 - \tilde{\alpha}^2}}{\tilde{\beta} \sqrt{\tilde{\alpha}^4 + \tilde{\beta}^2}} \right\} \right\}. \quad (10)$$

To determine the beam deflection rate, we perform the integration in Eq. 9 by expanding for small ellipticity, i.e., $|\epsilon|^2 \ll 1$. Then, along the unit circle, the second term in the square brackets of the numerator of Eq. 9 is small compared to the first, or $[1 + \epsilon^2 \cos^2 \theta]^{3/2} \approx 1 + (3/2)\epsilon^2 \cos^2 \theta$. Summing over the residues, we then obtain

$$\frac{\partial}{\partial z} \langle \tilde{k}_x \rangle = \frac{\sqrt{\pi}}{32} \left(\frac{v_0}{v_e} \right)^2 \frac{n}{n_c} \left(\frac{\omega_0}{k_0 c} \right)^2 \frac{M \bar{v}}{\sigma_x} \frac{\sigma_y}{\sigma_x} \left\{ \frac{\sqrt{\tilde{\alpha}^4 + \tilde{\beta}^2 - \tilde{\alpha}^2}}{\tilde{\beta} \sqrt{\tilde{\alpha}^4 + \tilde{\beta}^2}} + \frac{(3/2)\epsilon^2}{(1 - \tilde{\alpha}^2)^2 + \tilde{\beta}^2} \left[\sqrt{2} - \frac{\sqrt{\tilde{\alpha}^4 + \tilde{\beta}^2 + \tilde{\alpha}^2}}{\sqrt{\tilde{\alpha}^4 + \tilde{\beta}^2}} - (\tilde{\alpha}^2 - 1) \frac{\sqrt{\tilde{\alpha}^4 + \tilde{\beta}^2 - \tilde{\alpha}^2}}{\tilde{\beta} \sqrt{\tilde{\alpha}^4 + \tilde{\beta}^2}} \right] \right\}. \quad (11)$$

Figure 1 depicts $\langle \delta \bar{n} \rangle$ vs Mach number for both a circular beam (black curve), where $\sigma_y = \sigma_x$, and for an elliptic beam (gray curve), where $\sigma_y = 2\sigma_x$. In both cases, the density response near $M = 1$ is almost triple the response at $M = 0$. This demonstrates that the process of filamentation¹⁴ is enhanced by near-sonic transverse flow.

The density response of the elliptic beam is slightly greater than that of the circular beam for $\epsilon^2 > 0$ around the sonic surface. As σ_y becomes large compared to σ_x , we recover the 2D limit, where, for $M > 1$, the density response is positive, i.e., there is a density enhancement rather than a density cavity.

In the subsonic regime, for a circular beam, where $1 - M^2 \gg M \bar{v}$, $M < 1$, and $\epsilon = 0$, the expression for $\langle \delta \bar{n} \rangle$ as given by Eq. 10 reduces to

$$\langle \delta \bar{n} \rangle_{\text{subsonic}, \sigma_x = \sigma_y} \sim -\frac{1}{8} \left(\frac{v_0}{v_e} \right)^2 \frac{1}{\sqrt{1 - M^2}}. \quad (12)$$

For near-sonic flow, we evaluate Eq. 10 with $M = 1$ for a circular beam to find

$$\langle \delta \bar{n} \rangle_{\text{near-sonic}, \sigma_x = \sigma_y} \sim -\frac{1}{8} \left(\frac{v_0}{v_e} \right)^2 \frac{1}{2\bar{v}^{1/2}}, \quad (13)$$

i.e., the density response for near-sonic flow is a resonant response that is limited by the damping, or, in the limit of weak damping, would be limited by non-linear effects.¹⁷ For supersonic transverse flow, where $M^2 - 1 \gg M \bar{v}$, we find that Eq. 10 reduces to

$$\langle \delta \bar{n} \rangle_{\text{supersonic}, \sigma_x = \sigma_y} \sim -\frac{\bar{v}}{16} \left(\frac{v_0}{v_e} \right)^2 \frac{2M^2 - 1}{(M^2 - 1)^{3/2}}. \quad (14)$$

The density response of an elliptic beam is qualitatively different from that of a circular beam in the supersonic regime. When the beam is circular, the

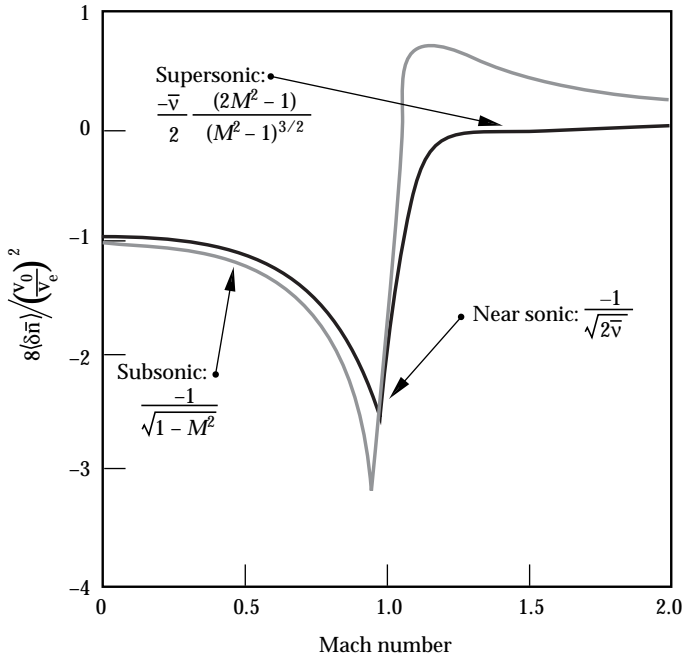


FIGURE 1. The average fractional density perturbation $\langle \delta \bar{n} \rangle$, normalized to $(v_0/v_e)^2/8$, vs Mach number when the ion damping decrement $\bar{v} = 0.1$. The black curve is for a circular beam, and the gray curve is for an elliptic beam, where $\sigma_y/\sigma_x = 2$. The average value of $\langle \delta \bar{n} \rangle$ is 2.5 times greater for the circular beam in near-sonic transverse flow than in the absence of transverse flow. (50-00-0898-1704pb01)

density response is always negative. However, when the beam is elliptic, such that $\sigma_y > \sigma_x$, i.e., the beam is narrower in the flow direction, the density response changes sign, becoming positive as it is in the $\sigma_x = 0$ limit of a line-focused beam.

In Figure 2, we plot the beam deflection rate vs Mach number for a circular beam (black curve) and an elliptic beam (gray curve). (In the circular beam limit, where $\sigma_y = \sigma_x \equiv \sigma$, only the first term in the large curly bracket of Eq. 11 survives.) The largest beam deflection rate occurs for near-sonic transverse flow. In the subsonic regime,

$$\begin{aligned} \frac{\partial}{\partial z} \langle \tilde{k}_x \rangle_{\text{subsonic}, \sigma_x = \sigma_y} \\ \sim \frac{1}{32} \sqrt{\frac{\pi}{2}} \left(\frac{v_0}{v_e} \right)^2 \left(\frac{n}{n_c} \right) \left(\frac{\omega_0}{k_0 c} \right)^2 \frac{1}{\sigma} \frac{M\bar{v}}{(1-M^2)^{3/2}}. \end{aligned} \quad (15)$$

Subsonically, the deflection rate scales linearly with the damping decrement and with Mach number, and increases as $M \rightarrow 1$.

In the near-sonic regime, for a circular beam, Eq. 11 reduces to

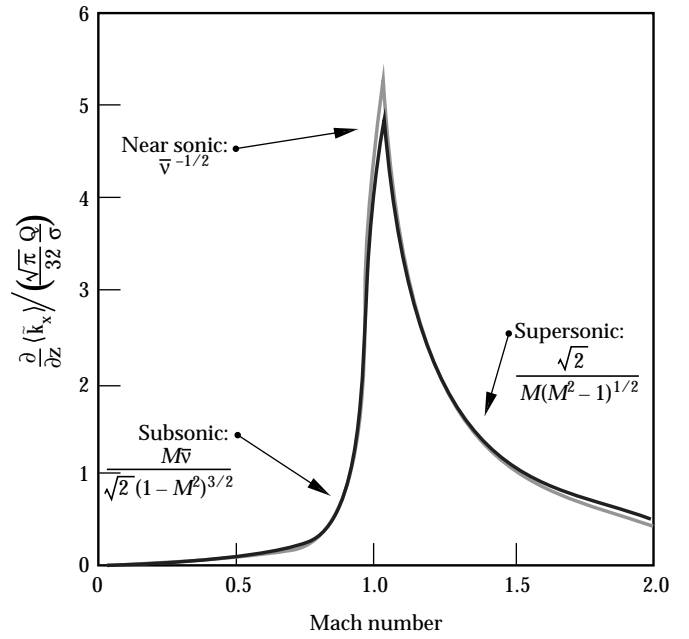


FIGURE 2. Beam deflection rate vs Mach number when the ion damping decrement $\bar{v} = 0.1$. The black curve is for a circular beam, and the gray curve is for a slightly elliptic beam, where $\sigma_y^2/\sigma_x^2 = 1.1$. The primary contribution to the beam deflection rate occurs when the transverse flow is nearly sonic. (50-00-0898-1705pb01)

$$\begin{aligned} \frac{\partial}{\partial z} \langle \tilde{k}_x \rangle_{\text{near-sonic}, \sigma_x = \sigma_y} \\ \sim \frac{\sqrt{\pi}}{32} \left(\frac{v_0}{v_e} \right)^2 \left(\frac{n}{n_c} \right) \left(\frac{\omega_0}{k_0 c} \right)^2 \frac{1}{\sigma \bar{v}^{1/2}}. \end{aligned} \quad (16)$$

As with the density response, the beam deflection rate exhibits resonant behavior near $M = 1$, which is limited by the inclusion of damping.

This expression can be integrated once when the density profile is constant, yielding

$$\langle \tilde{k}_x \rangle \sim \frac{\sqrt{\pi}}{32} \left(\frac{v_0}{v_e} \right)^2 \left(\frac{n}{n_c} \right) \left(\frac{\omega_0}{k_0 c} \right)^2 \frac{1}{\bar{v}^{1/2}} \frac{L}{\sigma}, \quad (17)$$

where $\langle \tilde{k}_x \rangle$ is the deflection angle in radians. If the hot spot length L_s , which for a Gaussian beam is the Rayleigh length, is long compared to the transverse-flow scale length L_w , then in the above equation, $L = L_w$, i.e., the transverse-flow scale length is the limiting length in the problem. If L_s is short compared to L_w , then L_s is the length in question. For an RPP beam, $\sigma \sim \hbar \lambda_0$ and $L_s \sim 8f^2 \lambda_0$, where f is the f -number of the optic, so

$$\langle k_x \rangle \sim \frac{\sqrt{\pi}}{32} \left(\frac{v_0}{v_e} \right)^2 \left(\frac{n}{n_c} \right) \left(\frac{\omega_0}{k_0 c} \right)^2 \frac{1}{\bar{v}^{1/2}} \frac{L_u}{f \lambda_0}, \quad L_u \ll L_s; \quad (18a)$$

and

$$\langle k_x \rangle \sim \frac{\sqrt{\pi}}{4} \left(\frac{v_0}{v_e} \right)^2 \left(\frac{n}{n_c} \right) \left(\frac{\omega_0}{k_0 c} \right)^2 \frac{f}{\bar{v}^{1/2}}, \quad L_s \ll L_u. \quad (18b)$$

This scaling does not account for multispeckle phenomena in an RPP beam, where light leaving one density depression can enter another density depression and continue to get swept downstream over a length longer than L_s .

Finally, in the supersonic regime, Eq. 11 takes the form

$$\begin{aligned} \frac{\partial}{\partial z} \langle \tilde{k}_x \rangle_{\text{supersonic}, \sigma_x = \sigma_y} \\ \sim \frac{\sqrt{2\pi}}{32} \left(\frac{v_0}{v_e} \right)^2 \left(\frac{n}{n_c} \right) \left(\frac{\omega_0}{k_0 c} \right)^2 \frac{1}{\sigma M} \frac{1}{(M^2 - 1)} \end{aligned} \quad (19)$$

For $M \gg 1$, the beam deflection rate scales as $1/M^2$, and is independent of the damping decrement. In all three regimes, the beam deflection rate scales with the figure of merit $Q \equiv (v_0/v_e)^2 (n/n_c) (\omega_0/k_0 c)^2$. In these limiting regions, our beam deflection rate results are in agreement with those of Ghosal and Rose.⁷

For a single Gaussian hotspot with circular cross section focused at $z = z_0$, Eq. 11 reduces to

$$\begin{aligned} \frac{\partial}{\partial z} \langle \tilde{k}_x \rangle_{\text{circular}} &= \frac{\sqrt{\pi}}{32} \left(\frac{v_0}{v_e} \right)^2 \left(\frac{n}{n_c} \right) \left(\frac{\omega_0}{k_0 c} \right)^2 \\ &\times \frac{M \bar{v}}{\sigma_0} \frac{1}{\left[1 + (z - z_0)^2 / (k_0^2 \sigma_0^4) \right]^{3/2}} \frac{\sqrt{\tilde{\alpha}^4 + \tilde{\beta}^2 - \tilde{\alpha}^2}}{\tilde{\beta} \sqrt{\tilde{\alpha}^4 + \tilde{\beta}^2}}. \end{aligned} \quad (20)$$

Here, v_0 and σ_0 are evaluated at the focus, $z = z_0$.

For constant density and flow, this expression can be integrated to give the total deflection of the Gaussian beam:

$$\begin{aligned} \langle \tilde{k}_x \rangle &= \frac{\sqrt{\pi}}{16} \left(\frac{v_0}{v_e} \right)^2 \frac{n/n_c}{1 - n/n_c} k_0 \sigma_0 \\ &\times \frac{M \bar{v}}{\tilde{\beta}} \frac{\sqrt{\tilde{\alpha}^4 + \tilde{\beta}^2 - \tilde{\alpha}^2}}{\sqrt{\tilde{\alpha}^4 + \tilde{\beta}^2}}. \end{aligned} \quad (21)$$

The above results, depicted in Figures 1 and 2, indicate that we should concentrate our simulation efforts near the $M = 1$ surface, where both $\langle \delta \bar{n} \rangle$ and the deflection rate peak.

In the weak damping limit, where a steady state is not reached, one would expect subsonic deflection from transient effects and self-induced bandwidth rather than from damping, and near $M = 1$, nonlinear effects¹⁷ would dominate the physics. In the experiments modeled in the next section, the plasma is composed of CH, with a damping decrement $\bar{v} \approx 0.1$. In this regime we anticipate subsonic and supersonic deflection with the $M = 1$ resonance limited by damping.

Beam Deflection: Modeling Results

As mentioned earlier in this article, gas-filled hohlraum experiments on the Nova laser³ show an effective spot motion of $150 \mu\text{m}$ toward the LEH that is reduced to $35 \mu\text{m}$ when RPPs are used on the laser beams. Near peak laser power, the plasma density and transverse flow profiles calculated by LASNEX² are depicted in Figure 3. The transverse flow profile is sheared, and is near sonic with a scale length of about $600 \mu\text{m}$ at the LEH. The plasma density is modeled as $n_e/n_c = .06 + .04 \tanh(z/\lambda_0)$, where $\lambda_0 = 0.351 \mu\text{m}$. Here, z is chosen such that $n_e/n_c = .01$, where $M = 1$. The corresponding electron temperature is $T_e \approx 3 \text{ keV}$.

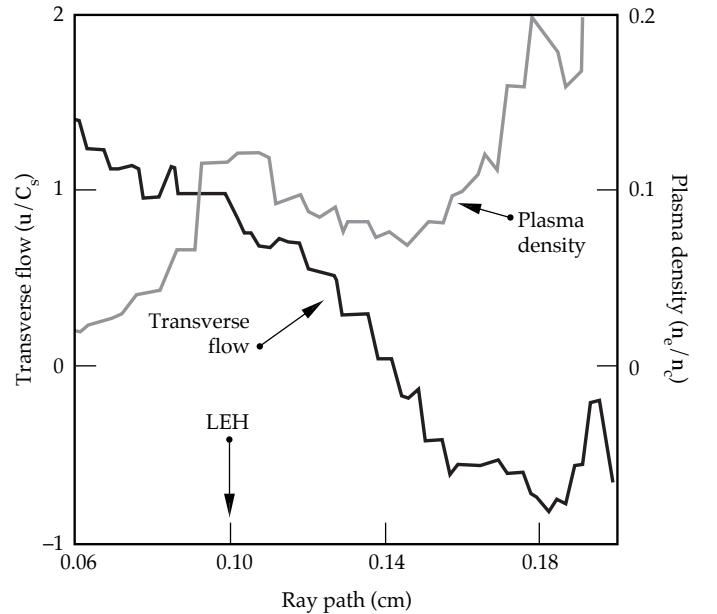


FIGURE 3. The transverse flow and plasma density profiles along a typical ray path in a methane-filled hohlraum near peak power on the Nova laser as calculated by LASNEX. The corresponding electron temperature is $T_e \approx 3 \text{ keV}$, and the laser light wavelength is $\lambda_0 = 0.351 \mu\text{m}$. (50-00-0898-1706pb01)

It remains to specify the beam structure. The simulated unsmoothed Nova beam⁶ 1 mm beyond best focus, which is the unsmoothed beam plane at the LEH, is markedly different in structure from the simulated RPP Nova beam^{6,8,9} at best focus, which is its beam plane at the LEH. Both beams are $f/4$ and have similar average peak intensities. The speckle statistics of the beams are the same, but the unsmoothed Nova beam contains large coherent pieces, as well as large voids, which give rise to sub-spot-scale intensity modulations upon which the speckle statistics are superposed.

The F3D code models the speckle statistics of a beam about a given average intensity. Computational limitations inhibit modeling of the entire beam in one simulation ($250\text{ }\mu\text{m} \times 250\text{ }\mu\text{m} \times 1000\text{ }\mu\text{m}$). Thus, we have taken the unsmoothed and RPP beams, and averaged the intensities in the initial beam cross section on a $28\text{ }\mu\text{m} \times 28\text{ }\mu\text{m}$ spatial scale. Each $28\text{ }\mu\text{m} \times 28\text{ }\mu\text{m}$ piece of the beam then has an average intensity at which a simulation is performed.

These spatially smoothed average intensities are plotted in Figure 4. The peak value for the RPP beam is $3 \times 10^{15}\text{ W/cm}^2$, as opposed to $1 \times 10^{16}\text{ W/cm}^2$ for the unsmoothed beam. An F3D simulation was performed at each spatially smoothed average intensity in the beam over a propagation distance of $350\text{ }\mu\text{m}$. At $z = 350\text{ }\mu\text{m}$,

each piece of the beam is placed back in its original beam position, and the entire beam is paraxially propagated through 1 mm of plasma at density $n = 0.1n_c$, roughly the distance from the LEH to the wall. The intensity distribution vs wall position of the RPP and unsmoothed beams is plotted in Figure 5. The peak of the RPP beam is located within $50\text{ }\mu\text{m}$ of where it was pointed, whereas the centroid of the unsmoothed beam is $\sim 100\text{ }\mu\text{m}$ closer to the LEH than it was pointed, in agreement with experimental results. Moreover, the general structure of the predicted laser intensity on the wall, of a wide “plateau” or “shoulder” in the flow direction, is in agreement with the x-ray emission profile measurements. Thus we see that it is the difference in the intensity distributions of the beams, i.e., the beam structure, that accounts for the change in effective wall position for unsmoothed vs RPP beams.

A secondary feature that also enhances the deflection of the unsmoothed beam arises from the focusing geometry. The unsmoothed $f/4$ Nova beam is focused 1 mm outside the LEH, and in the beam plane at the LEH, the hot spots in the beam are more accurately described by $f/6$ speckle statistics. Because an $f/6$ speckle is longer [by a factor of $(3/2)^2$] and wider [by a factor of $(3/2)$] than an $f/4$ speckle, the spatial region of a given hot spot over which beam deflection can occur is larger, thus yielding more beam deflection.

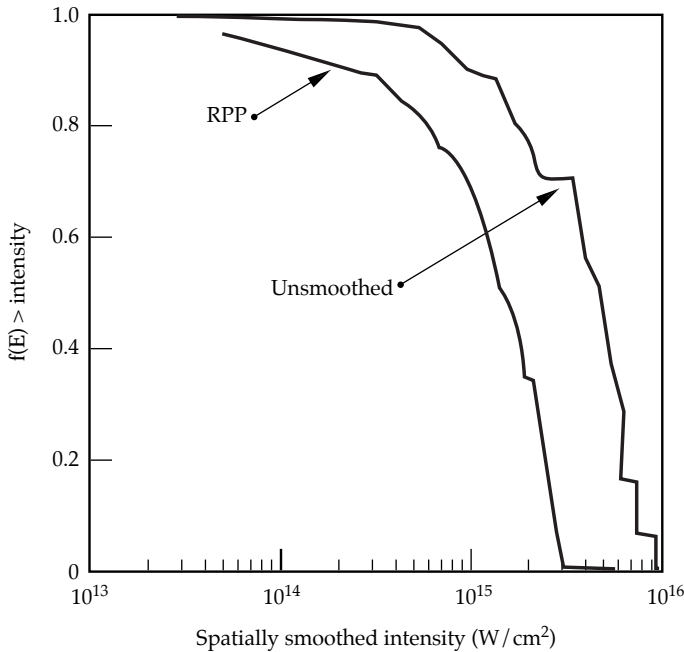


FIGURE 4. The running sum of the intensity distributions of RPP and unsmoothed Nova beams vs intensity when the intensity is spatially averaged on a $28\text{ }\mu\text{m} \times 28\text{ }\mu\text{m}$ scale. The RPP beam has a peak spatially averaged intensity of $3 \times 10^{15}\text{ W/cm}^2$, whereas the unsmoothed beam peaks at $1 \times 10^{16}\text{ W/cm}^2$. (50-00-0898-1707pb01)

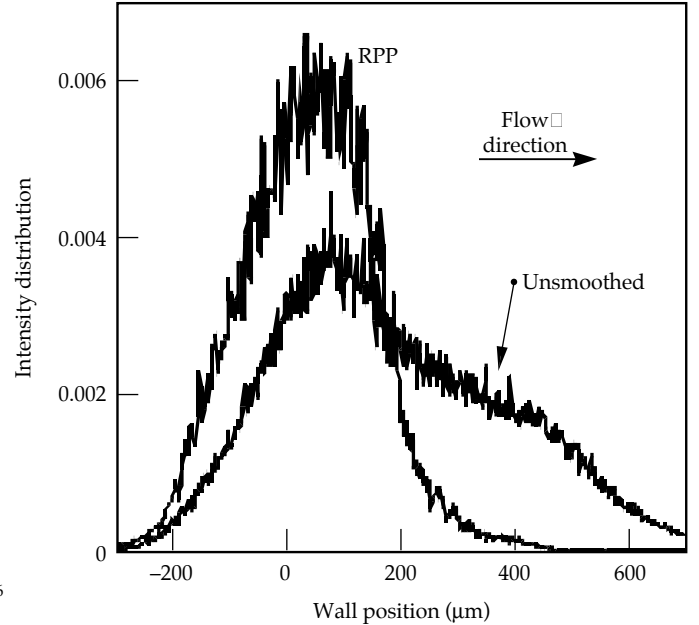


FIGURE 5. The intensity distribution vs wall position of the RPP and unsmoothed Nova beams near peak power. The peak of the RPP beam is located within $50\text{ }\mu\text{m}$ of where it was pointed, whereas that of the unsmoothed beam is $100\text{ }\mu\text{m}$ closer to the LEH than pointed. The unsmoothed beam also has a high shoulder off the peak in the flow direction. (50-00-0898-1708pb01)

Channel Formation by Ultraintense Laser Light

Channeling of intense laser light is crucial to the fast ignitor concept,¹⁰ where light must reach the over-dense regime. Prior to channeling the intense laser light, a channel must be *created* by the “hole-boring” pulse. We have begun to examine and analyze beam propagation in underdense plasma in an effort to better understand the channel formation process.

We utilize a relativistic form of F3D¹¹ to study channeling. In this form, the index of refraction in the light-wave equation has been modified according to the replacement $n_e \rightarrow n_e / \gamma$, where $\gamma \equiv (1 + u_0^2 / c^2)^{1/2}$, with $u_0 \equiv eA_0 / (m_e c)$. [Here, A_0 is the RMS value of the vector potential of the light wave.] This accounts for relativistic corrections to the electron mass. We have modified the ponderomotive drive in the momentum equation by making the replacement $\nabla u_0^2 / 2 \rightarrow c^2 \nabla \gamma$, so that momentum is conserved. At very high intensities, the ponderomotive drive then scales as $c \nabla u_0$ rather than as $\nabla u_0^2 / 2$ as it does at moderate intensities where $\gamma \approx 1$. Finally, we have implemented a charge-separation model similar to that of Sun et al.,¹⁸ where $n_e = \max[0, Z n_i + (m_e c^2) / (4\pi e^2) \nabla_{\perp}^2 \gamma]$. Here, n_i is the ionic density, m_e is the electronic mass, Z is the ionic charge, and e is the electronic charge. This charge-separation model permits the electrons to be blown out of the channel by the ponderomotive force on very short (sub-picosecond) time scales, inducing a charge separation that then draws the ions out of the channel as well. On the time scale of the simulations presented below (30 ps), the charge-separation term has negligible effect, as the ions have had time to move.

This fluid model does not include such effects as Raman forward scatter (RFS), plasma heating, or

thermal filamentation. RFS and plasma heating, which are included in PIC simulations,¹⁹ would act to deplete the pump and create hot electrons in the channel, thereby limiting the ability to create a channel. Thus, these fluid simulations place an upper bound on the channel depth, and hence on the ability to create a channel.

We have propagated a 30-ps FWHM (full width at half maximum) Gaussian beam with peak intensity $5.7 \times 10^{17} \text{ W/cm}^2$ and a waist of $15 \mu\text{m}$ at best focus through 1 mm of underdense plasma at density $n_e = 0.1 n_c$ and electron temperature $T_e = 2 \text{ keV}$. The beam filaments into several pieces, and the main (central) filament contains 65 to 70% of the intensity. The laser beam has self-focused by an order of magnitude in intensity, because of both relativistic and ponderomotive effects. The central filament plasma density is at about $n_e = 0.01 n_c$, and a channel forms through the entire 1 mm of plasma. We find that this process occurs for a range of FWHM spot sizes from 3 to $15 \mu\text{m}$.

Figure 6 depicts the $x = 0$ slice of the laser amplitude (Figure 6a) and the plasma density (Figure 6b) for an unaberrated, super-Gaussian $f/3$ laser beam. Clearly, a channel has formed through $400 \mu\text{m}$ of $n_e = 0.1 n_c$ plasma after 15 ps. We have ascertained that channel formation occurs for a wide range of cone angles, from $f/3$ to $f/10$.

We have also simulated beams with both random phase aberrations and spherical aberrations. Figure 7 shows the $x = 0$ slice of the laser amplitude (Figure 7a) and the plasma density (Figure 7b) for an $f/3$ laser beam with random phase aberrations, which expand the spot size at best focus to $15 \mu\text{m}$. In Figure 7a, we observe 3 hot spots near best focus, located at $z = 180 \mu\text{m}$, which have self-focused and thereby increased the intensity by a factor of 2. In

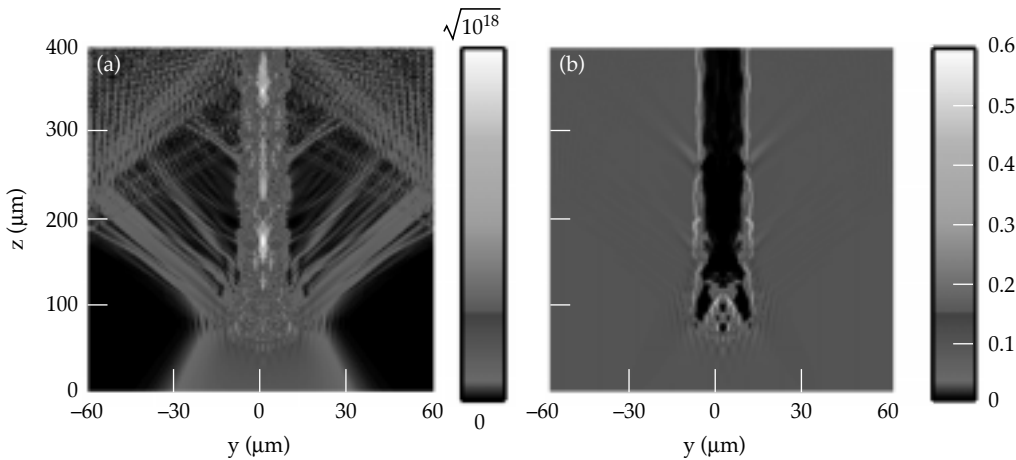


FIGURE 6. The laser amplitude and plasma density for an unaberrated, super-Gaussian $f/3$ laser beam with $\sim 3 \text{ TW}$ of input power. After 15 ps, the beam has created a channel through $400 \mu\text{m}$ of plasma at density $n_e = 0.1 n_c$. (50-00-0898-1709pb01)

FIGURE 7. The laser amplitude and plasma density for a phase-aberrated $f/3$ beam with a spot size of $15\ \mu\text{m}$ at best focus and with $\sim 3\ \text{TW}$ of input power. After 30 ps, the beam has failed to channel through $400\ \mu\text{m}$ of plasma at density $n_e = 0.1n_c$ whereas a diffraction-limited $f/3$ beam creates an evacuated channel within 15 ps. (50-00-0898-1710pb01)

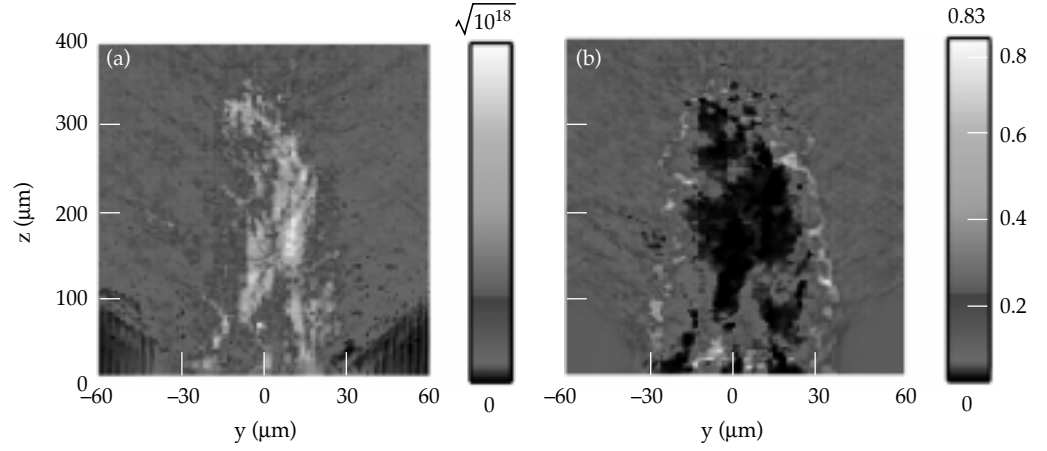


Figure 7b, plasma has been pushed out of the regions where the beam is most intense. The beam structure, i.e., the presence of multiple hot spots, locally increases the intensity, but not globally. Thus relativistic and ponderomotive self-focusing is limited to the hot-spot regions, from which plasma density is expelled. With either random phase or spherical aberrations, a channel does not form through $400\ \mu\text{m}$ of $n_e = 0.1n_c$ plasma in 30 ps, even though the beam contained the same amount of power ($\sim 3\ \text{TW}$) as the diffraction-limited beam. We thus conclude that aberrated beams do not channel as effectively as diffraction-limited beams.

Conclusions

In summary, we have shown that a predictive capability requires a model that contains the important beam-structure characteristics. We have presented two examples where the beam structure was essential.

In the first example, we studied beam deflection caused by transverse flow. We derived a global formula for the steady-state density response and beam deflection rate, valid for all Mach numbers. In the weak damping limit, when a steady state may not be reached, the effective damping decrement $\bar{\nu}$ can be estimated by the magnitude of the transient density response $\partial_t(\delta\bar{n})/\delta\bar{n}$. In practice, the $\bar{\nu} \rightarrow 0$ limit is never achieved because of residual time-dependent effects such as transients, self-induced bandwidth, and background evolution. Also, in the weak damping limit, nonlinear effects become important in the near-sonic regime. In the subsonic regime, the beam deflection rate scales linearly with the damping decrement and with Mach number, and scales inversely with $(1 - M^2)^{3/2}$. The density response is independent of the damping decrement in this regime, and scales inversely as $(1 - M^2)^{1/2}$. Around $M = 1$, damping limits

the resonant response, and both the beam deflection rate and the density response scale as $\bar{\nu}^{-1/2}$. In the supersonic regime, the beam deflection rate is independent of the damping decrement, and scales as $1/[M(M^2 - 1)^{1/2}]$. Here, the density response is proportional to the damping decrement, and scales as $1/(M^2 - 1)^{3/2}$. Such analysis can be used to formulate a reduced description in models where laser propagation is not treated in detail.²

We have used this information to focus our modeling efforts where the transverse flow is near-sonic, which, in gas-filled hohlraums, is around the LEH. When the marked difference in the intensity distributions of the unsmoothed and RPP beams is folded into our modeling, we find that the intense portions of the unsmoothed beam deflect more (in agreement with our figure-of-merit scaling), thereby moving the wall spot centroid of the unsmoothed beam closer to the LEH than that of the RPP beam. Our results agree with the x-ray emission data in gas-filled hohlraum experiments.³

In our second example, we studied the effect of beam structure on channeling of intense laser beams. We determined that an idealized beam, containing only one hot spot with a peak intensity at $5.7 \times 10^{17}\ \text{W}/\text{cm}^2$, successfully creates a channel through underdense plasma at density $n = 0.1n_c$. However, if a more realistic beam model is used, such as one containing random phase aberrations but with the same input power as that of the idealized beam, we find that a channel does not form. Plasma density is expelled from the regions where the beam has hot spots, but builds up between the hot spots. This work has set in place the required framework to perform further analysis, such as determining the intensity threshold as a function of beam structure above which channel formation occurs.

Acknowledgments

We acknowledge valuable input from H. A. Rose, M. D. Rosen, R. L. Kauffman, S. G. Glendinning, L. J. Suter, B. F. Lasinski, K. G. Estabrook, and M. H. Key.

Notes and References

1. J. F. Drake et al., *Phys. Fluids* **17**, 778 (1974); D. W. Forslund, J. M. Kindel, and E. L. Lindman, *ibid.* **18**, 1002 (1975); *Advances in Plasma Physics*, edited by A. Simon and W. B. Thompson (Wiley, New York, 1976), Vol. 6.
2. G. Zimmerman and W. L. Kruer, *Comments Plasma Phys. Control. Fusion* **2**, 85 (1975).
3. L. V. Powers et al., *Advances in Laser Interaction with Matter and Inertial Fusion*, edited by J. M. Martinez-Val, E. Minguez, and J. M. Perlado (World Scientific, 1996); N. Delamater et al., *Phys. Plasmas* **3**, 2022 (1996).
4. J. D. Moody et al., *Phys. Rev. Lett.*, **77**, 1294 (1996).
5. P. E. Young et al., *Phys. Rev. Lett.* **81**, 1425 (1998).
6. S. N. Dixit et al., *Appl. Opt.* **32**, 2543 (1993); S. N. Dixit, M. D. Feit, M. D. Perry, and H. T. Powell, *Opt. Lett.* **21**, 1715 (1996).
7. S. Ghosal and H. A. Rose, *Phys. Plasmas* **4**, 2376 (1997).
8. R. L. Berger et al., *Phys. Fluids B* **5**, 2243 (1993).
9. Y. Kato and K. Mima, *Appl. Phys. B* **29**, 186 (1982).
10. M. Tabak et al., *Phys. Plasmas* **1**, 1626 (1994).
11. A. B. Langdon, D. E. Hinkel, B. F. Lasinski, and C. H. Still, *Bull. Am. Phys. Soc.* **42**, 1940 (1997).
12. R. W. Short, R. Bingham, and E. A. Williams, *Phys. Fluids* **25**, 2302 (1982).
13. H. A. Rose, Los Alamos National Laboratory, Los Alamos, NM, private communication, LLNL, 1995.
14. D. E. Hinkel, E. A. Williams, and C. H. Still, *Phys. Rev. Lett.* **77**, 1298 (1996).
15. S. Skupsky et al., *J. Appl. Phys.* **66**, 3456 (1989).
16. C. E. Max, *Phys. Fluids* **1**, 74 (1976); M. V. Goldman, K. Rypdal, and B. Hafizi, *ibid.* **23**, 945 (1980); J. J. Rasmussen and K. Rypdal, *Phys. Scr.* **3**, 481 (1986).
17. W. L. Kruer and J. H. Hammer, *Comments Plasma Phys. Control. Fusion* **18**, 85 (1997).
18. G.-Z. Sun, E. Ott, Y. C. Lee, and P. Guzdar, *Phys. Fluids* **30**, 526 (1987); M. D. Feit, J. C. Garrison, and A. M. Rubenchik, *Phys. Rev. E* **56**, 2394 (1997).
19. D. W. Forslund et al., *Phys. Rev. Lett.* **54**, 558 (1985); W. B. Mori et al., *ibid.* **60**, 1298 (1988); K. C. Tzeng, W. B. Mori, and C. D. Decker, *ibid.* **76**, 3332 (1996).

NOVA/BEAMLET/NIF UPDATES

APRIL–JUNE 1998

R. Ehrlich/P. Wegner/S. Kumpan

Nova Operations

Nova Operations performed 229 experiments during this quarter. These experiments supported efforts in ICF, Defense Sciences, university collaborations, Laser Science, and Nova facility maintenance. At the beginning of June, the operation of Nova expanded back to a full two shifts per day, with 2.5 hours of overlap between shifts. Nova now operates four days per week continuously from 6:30 a.m. to 12:30 a.m. This will allow the operations group to achieve the goal of 900 experiments in FY 1998.

Several new systems and diagnostics were added to Nova. The temporary installation of the $f/8.5$ lens system on one beamline was successful. Experiments were successfully performed utilizing this system both with and without an array of wedged KDP crystals for studying the effect of a polarization smoothing technique on the backscatter levels of various targets. New diagnostics, such as a driven wave Thomson scattering measurement system, were fielded. Another new system was added in the laser bay, which allows beamline 10 to be used as a backlighter. This increases the number of beamlines that can propagate the separate backlighter pulse to four.

Many improvements were made to the Petawatt system. Beginning in April, the first full-power target experiments were performed with the Petawatt deformable mirror. Using the sensor packages, it was determined that there are ~ 4 waves of static distortion in the Nova chain and several waves of thermal distortion due to heating of the amplifier disks. The mirror successfully corrects for these distortions by running a probe beam through the chain to the Hartmann sensor, and actively correcting the wavefront up to ~ 20 minutes before a shot. Averaging software was developed to keep the mirror from overcorrecting for turbulence occurring on a fast time scale. Pump-induced distortions are on the order of 1.8 waves

peak-to-valley, and are corrected for by creating a pre-correct file from the previous shot, which is applied immediately before the system shot. Because the cumulative wavefront correction is applied early in the amplifier chain, it was necessary to increase the diameter of the spatial filter pinholes early in the amplifier chain to avoid clipping. This allows high spatial frequencies to propagate through the chain, generating small-scale modulation in the near-field irradiance. This modulation causes a significant fraction of the beam energy to scatter outside the central focal spot.

Prior to using the wavefront control system, the focal spot at target chamber center was many times diffraction limited, with multiple hot spots within the central peak due to thermal distortion of the amplifier disks. With the deformable mirror, a single hot spot $\sim 10\text{ }\mu\text{m}$ in diameter (full-width-half-maximum) is reproducibly delivered on target. This spot typically contains $\sim 28\%$ of the total energy in the central peak, corresponding to a maximum intensity of $\sim 4 \times 10^{20}\text{ W/cm}^2$ to date.

Beamlet Operations

During the third quarter of FY 1998, Beamlet continued to provide a testbed for validating the laser physics and engineering foundations of the National Ignition Facility (NIF). We completed a total of 128 full-system shots, 72 of which were dedicated to testing prototype NIF frequency converters, 25 to testing prototype fused-silica final optics at high 3ω fluence, and 16 to completing high-power, high-B-integral 1ω beam propagation experiments with angularly dispersed bandwidth as required for 1D smoothing by spectral dispersion (SSD). At the end of the quarter, we began a series of experiments for the French Commissariat d'Énergie Atomique (CEA) and completed a 15-shot campaign to measure thresholds for 3ω filamentation and damage in high-quality fused silica.

The frequency conversion work on Beamlet involved extensive testing of NIF production crystals, both conventional growth and rapid growth, in a 37-cm-aperture final optics cell (FOC) in the NIF-like vacuum environment of the Beamlet final-optics-assembly test mule. The purpose of the work was to validate the design of the NIF frequency converter and verify the physics models on which a detailed error analysis of its performance is based. As part of these tests, we measured (1) the second-harmonic conversion efficiency of a converter incorporating the first rapidly grown 37-cm type-I KDP doubler, (2) the third-harmonic conversion efficiency of a converter consisting of conventionally grown crystals from NIF production boules, and (3) the third-harmonic conversion efficiency of a converter consisting of the rapid-growth doubler and the first rapid-growth 37-cm tripler. Maximum efficiencies (whole beam, time integrated) were 70.5%, 75%, and 73% respectively measured at drive irradiances of between 3.6 and 3.9 GW/cm² in 1.5-ns square pulses. In each case, the measured efficiencies were within a few percent of modeling, assuming values for component transmissions measured prior to the experiments.

A small number of additional frequency conversion experiments were done to evaluate the effects of increased bandwidth with angular dispersion on 3 ω efficiency, under conditions relevant to beam smoothing. Tests with 80 GHz (3Å) of 1 ω bandwidth critically dispersed and 135 GHz (5Å) of bandwidth critically dispersed and 3 \times the critical dispersion condition showed reductions in efficiency to be less severe by ~30 to 40% than what was expected based on 2D modeling. The importance of choosing the correct dispersion direction was also demonstrated by reversing the sign of the dispersion along the tripler optic axis and measuring a corresponding reduction in efficiency of as much as 5%.

Tests to measure the effects of increased bandwidth and dispersion on 1 ω beam quality in the laser amplifier were more extensive. The purpose of the measurements was to determine how the conditions for SSD reduce the operating margin against B-integral induced-beam breakup. The tests were conducted with 500-ps pulses using 167- μ rad pinholes in the cavity spatial filter and with no pinhole in the transport spatial filter. The pulses were propagated through unpumped booster amplifiers to produce the high B-integrals expected at the end of a long, saturating ignition pulse. At B integrals in the booster amplifiers up to ~25% higher than the NIF limit of 1.8 rad, no difference in near-field beam quality was observed for the baseline SSD condition of 80 GHz critically dispersed, for which the divergence is ± 7.5 μ rad. Onset of beam degradation was observed when the divergence reached ± 25 μ rad, at which point the near-field irradiance contrast

measured at a B of 2.1 rad was equivalent to the contrast measured at 2.3 rad without SSD, suggesting a reduction in operating margin of ~10%.

Full-aperture tests of high-damage-threshold silica components were also conducted for the first time this quarter. The goal of the campaign was to test a NIF-like FOC and debris shield at average 3 ω fluences of 6 J/cm² in 3-ns square pulses for 20 shots. The initial shot sequence consisted of a five-shot ramp and eight shots at 6 J/cm², with only the FOC containing frequency conversion crystals and a final focus lens installed in the test mule. Optics condition during this part of the campaign was quite good. After installation of a debris shield and seven additional shots at 6 J/cm², extensive damage occurred on the output surface of the tripler and the input surface of the lens. Evidence suggests that the damage was related to a back reflection from the debris shield, which was misdirected onto the Al wall of the FOC.

The first of the French CEA campaigns was completed this quarter. The purpose of the campaign was to test fused silica windows with a large-aperture, high-quality 3 ω beam to determine thresholds for filamentation and damage that could be extrapolated to the target chamber vacuum windows on the LMJ. Two parts were tested (Suprasil 312 and Herasil 1SV) in the test mule vacuum chamber at a plane 2 m downstream of the $f/20$ 3 ω focus, which was spatial filtered. Onset of filamentation occurred at an aperture-averaged intensity-length product of between 25 and 30 GW/cm as measured at a pulse duration of 200 ps. High-fluence testing up to aperture-averaged fluences of 13 J/cm² in 3-ns produced damage that was significantly less than expected from off-line tests.

National Ignition Facility

Overall progress on the NIF Project remains satisfactory for the third quarter of FY98. NIF Conventional Facilities construction made good progress, and a total of eight DOE/OAK Performance Measurement Milestones were completed. In June, Walsh Pacific (CSP-3) finished its major concrete work in the Target Building and Switchyards essentially on schedule. Nielsen Dillingham's (CSP-4) steelwork in the Laser Bays started in April, about six weeks later than originally planned. This delay was anticipated during the bid period for CSP-9, Laser Building Finish & Central Plant, so the milestones were adjusted by four to six weeks to compensate. The critical path for Conventional Facilities, which runs through CSP-9, is delayed by roughly two to four weeks, but the fourth quarter 03 Project completion date is being held.

In Special Equipment, 89% of the Mid-Title II (65%) design reviews, and 24% of the Title II (100%) final design reviews have been completed. Design reviews continue to be successfully held, and

drawing production continues, although at a rate slower than planned. Some reviews and the follow-on procurement activities are now beginning to lag the schedule dates, which reduces the available schedule float for these activities. Efforts are now under way to streamline the review process to maintain the FY98 Title II completion schedule. The Beam Transport Vessels and Enclosures procurement was awarded early in June, and the Target Chamber contract is on schedule.

In Optics, facilitization is moving well at all NIF vendors as they prepare for pilot production in late FY98 or in FY99. Zygo and Corning will both begin pilot production in the fourth quarter in portions of their facilities while they complete facilitization tasks in other areas. Schott, Hoya, and Tinsley will begin their pilots in the first quarter of 1999. KDP rapid growth and finishing pilots have already started at LLNL, and the external-vendor rapid-growth pilots are set to begin in early FY99 at Cleveland Crystal and Inrad. Facilitization at the University of Rochester Laboratory for Laser Energetics and Spectra-Physics is on schedule to begin their pilots later in FY99. The longest lead substrate material, polarizer substrates, has already been received for pilot. The first NIF production optics orders were awarded to Schott and Ohara for the polarizer substrates, and to Ohara and Pilkington for LM3 mirror BK7 substrates.

Key Assurance activities during the third quarter to support the Project included Assurances safety support and QA surveillance of major concrete pours including the initiation of shielding concrete pours. Litigation activities included litigation support to the DOE for the settlement of 60(b)—Agreement to prepare a Programmatic Environmental Impact Study supplement analysis and to conduct specific evaluations and surveillance of potential buried hazardous materials—and the overall litigation against the Stockpile Stewardship Program's *Programmatic Environmental Impact Statement*; the NIF Construction Safety Program; interface with the Institutional surveillance for buried hazardous/toxic and/or radioactive materials; Risk Management Plans; the *Final Safety Analysis Report*; assurance surveillances and audits; and support of environmental permits. All are on schedule.

There were no Level 0, 1, 2, 3 milestones due during the third quarter. There were 26 DOE/OAK Performance Measurement Milestones due, and 21 were accomplished. There was a total of 56 milestones due through the end of the third quarter, and 52 have been accomplished, for an overall variance of 4. This is based upon DOE/OAK's concurrence with Rev. c of the FY98 Milestones, which was effective May 1, 1998.

The current assessment of Project status remains similar to that stated at the end of the second quarter; that there will be no change to the fourth quarter 01 Level 2 milestone for the End of Conventional

Construction, nor to the fourth quarter 03 Project Completion date. However, it is still anticipated that there could be a three- to six-week impact to the fourth quarter 01 Level 4 milestone for the start-up of the first bundle. Due to the status of Laser Bay steel erection, the current assessment is that there may be a four- to six-week impact to other internal milestones for construction. The Project Office is working with Nielsen Dillingham to determine how best to accelerate the steel work early in the fourth quarter. The Integrated Project Schedule is also being reviewed to find potential work-arounds to minimize impact to the first bundle.

Site & Conventional Facilities

NIF Conventional Facilities construction made good progress during the third quarter and completed a total of eight DOE/OAK Performance Measurement Milestones. Of these, five of six due in the third quarter plus two remaining from the second quarter were completed, and one due in the fourth quarter was completed early. In June, Walsh Pacific (CSP-3) finished their major concrete work in the Target Building and Switchyards essentially on schedule (plus nine rain days), as a result of several months of accelerated double shift work (see Figure 1). Nielsen Dillingham's (CSP-4) steelwork in the Laser Bays started about six weeks late in April, was delayed by rain in early May, then began to accelerate in late May and early June. However, efforts to further accelerate the schedule in June did not materialize. Therefore, due to the lack of progress on CSP-4 steelwork in the Laser Building, there is approximately a four to six



FIGURE 1. Switchyard 1 concrete pour. (40-60-0598-1213#7pb01)

week lag in the completion of internal milestones for this subcontract. This delay was anticipated during the bid period for CSP-9, so the milestones were adjusted by four to six weeks in CSP-9 to compensate for the delays coming from CSP-4. However, the critical path for Conventional Facilities that runs through CSP-9 is delayed by roughly two to four weeks. In addition, the field team is closely watching progress to ensure that the facility will be essentially dried-in by the start of the rainy season. Efforts to accelerate roofing activities under CSP-4 may be undertaken to ensure the dry-in of the facility.

June was generally a positive month for the NIF Conventional Facilities construction effort; clear weather allowed work to proceed at full speed. Walsh Pacific (CSP-3) completed its work and demobilized from the site. Nielsen Dillingham (CSP-6/10) began work in the Target Area, Switchyards and Diagnostics Building, and has made excellent progress to date. Although access to the work area was delayed for Nielsen Dillingham for CSP-6/10 due to Walsh's late departure, the team anticipates full recovery of the schedule. Work in the Optics Assembly Building (OAB) made good progress in the third quarter. The erection of structural steel began several weeks early, placing the work on the OAB slightly ahead of schedule. The site utility work is progressing at a fairly slow pace; multiple prime contractors on the site are creating some challenges to the team's ability to open excavations that do not choke the site circulation. The work has not progressed per the initial schedule, however, there has not yet been an impact to the critical path of the Conventional Facilities work. Significant, visible progress has resulted from field efforts in June.

Three FY98 DOE/OAK Performance Measurement Milestones were achieved on the NIF site in April: the issuance of the Notice to Proceed for CSP-6/10, the start of Laser Bay Core Structural Steel Erection (see Figure 2),



FIGURE 2. Looking north from Switchyard 1. (40-60-0598-1007#3pb02)

and the completion of Laser Bay Footings. One DOE/OAK milestone, the completion of Storm & Sanitary Sewer Lines, was delayed until October. This adjustment does not affect the critical path on either Conventional Facilities or the Project. One milestone, Switchyard Mat Slabs Pour, was achieved in May. Four milestones were achieved in June: Start Concrete F/R/P/C East Wall for Switchyard 2, achieved with the erection of forms; Start Overhead Platform Set-up for Laser Bay 2, achieved with delivery and staging of the platform materials; Start Concrete F/R/P/C for Target Bay Cylinder, achieved with erection of forms; and OAB Start Structural Steel Erection, originally scheduled for July, also achieved in June. The milestone not achieved was the Complete Structural Steel Erection for the Laser Bays, currently estimated for completion in August, seven weeks later than originally planned.

- All contract work by Walsh Pacific, CSP-3, was completed in June except for the curbs that sit on top of the footings between grids 28 and 30 (between the Laser Building and the OAB). This work was removed from CSP-3 and added to CSP-5 to allow for better access between the Laser Building and the OAB. The total concrete placed was 6872 yards during the third quarter. This contract is considered to be 100% complete.
- Steel erection of the Laser Building Core by Nielsen Dillingham, CSP-4, was completed in June, and bolting and plumbing is approximately 25% complete. Erection of Laser Bay 2 is approximately 75% complete, but bolting and plumbing has not started.
- Four isolation pads, slab on grade, and return walls bordering the OAB equipment pads were placed in three separate pours by Nielsen Dillingham, CSP-5. The Special Equipment granite slab was placed on the spatial filter tower alignment pad.
- Work began in earnest for Nielsen Dillingham, CSP-6/10, during June. The formwork for the Target Bay 18-in. and 30-in. columns was put in place with rebar. The first concrete pour for the columns was completed utilizing a 52-m pump truck and the 5000-psi shielded concrete. The second pour for the remaining columns in the Target Bay was also completed. All of the first three pours were completed to the -22.75-ft level.
- The majority of work performed in June by Hensel Phelps, CSP-9, was related to the site utilities. Material for the overhead platform to be used in the Laser Bays was received, and staging began in June. Site utility work is continuing, including installation of mechanical utility bundles at the East side of the site up to the Central Plant and installation of chilled water piping, hydronic piping, domestic water, and sewer lines around the OAB.

Special Equipment

Design reviews continue to be successfully held, and drawing production continues, although at a rate slower than expected. Procurement packages are being reviewed, revised, and released. Detail planning for FY99 is well under way, and reviews of the FY99 Cost Account Plans have been started.

Mid Title II (65%) design reviews were held for the Final Optics Damage Inspection System, the Pulse Synchronization System, the Laser Injection, and for the Operations Special Equipment Control System Supervisory Controls. Final (100%) design reviews were held for the Target Chamber Vessel, the Line Replaceable Unit (LRU) Assembly Verification System, the Vacuum System, the Supervisory Control (Applications), Target Area Auxiliary Systems, and the Communications/Environment Monitor System. In addition, Final Documentation and Procurement Reviews were held for the Beam Transport Enclosures for the structural supports for the Transport Spatial Filter (TSF), Cavity Spatial Filter (CSF), and Preamplifier Module Support Structure (PASS). Design review reports were prepared and released for the Supervisory Control (Framework) 100%, the Final Optics 65%, the Computer Systems 100%, and the Target Area 65% reviews. Changes to the required content for the 100% design reviews are being considered to reduce the amount of preparation and presentation time. This is based on the successful completion of most of the 65% reviews focusing on the design, and intent to focus the 100% reviews on the procurement readiness and design basis book completion for that subsystem.

Laser Systems. The Laser Systems detailed designs are progressing roughly according to plan. Drawings are being completed at a rapid pace, and manufacturing prototypes or first-article prototypes of various assemblies are being procured and tested. The emphasis of prototype testing has shifted from optical performance to more engineering-like concerns such as cleanliness, vibration, installation, assembly, and kinematic mounting.

- During the third quarter, the Preamplifier Module (PAM) prototype was assembled, and testing began. The electronics bay was installed and tested, and the regenerative amplifier was activated. Alignment of the multipass amplifier is in progress in preparation for energy extraction tests. This prototype will be used during the next quarter to validate the PAM design relative to the system requirements. Numerous technical issues with the design of the Master Oscillator Room (MOR) hardware were also addressed. Stability issues with the baseline oscillator design motivated the identification of several commercially available alternative oscillators. The most promising of these have been ordered to validate their performance relative to their specifications. The

FM-to-AM conversion noted during the last quarter motivated a change in the fiber used in the MOR design from a polarization-maintaining fiber to a polarizing (PZ) fiber. The PZ fiber has been specified and a test-run ordered from 3M for testing. The prototype arbitrary waveform generator system was coupled with the electro-optic modulator to produce the baseline Haan optical pulse from the MOR system (see Figure 3). Alignment testing of the prototype PAM was completed during the past quarter. The procedure was defined, and the rails were successfully aligned. Maxwell Physics International presented a successful design review for the PAM power-conditioning unit.

- During the past quarter, four tiger teams were established to analyze and interpret amplifier performance data collected using the AMPLAB prototype. Computer codes for reducing AMPLAB gain and wavefront data were revised and tested. Much of the wavefront data were reduced and compared with model predictions. Reduction of the gain data is under way. Additional thermal recovery experiments were performed on the AMPLAB after insulation was applied to the outside surfaces of the amplifier, beam tubes, and mirror towers, to improve thermal stability; this data is being analyzed. Detailed hardware designs are proceeding at a rapid pace, and a prototype amplifier Frame Assembly Unit was ordered and is being fabricated. The slab holder design was modified to address slab abrasion and assembly difficulties experienced on the prototype. A management review was conducted for the conversion of Building 381W into the Frame Assembly Unit Assembly Area. The plan was approved, and the Program will cover the costs for the conversion, including the clean room.

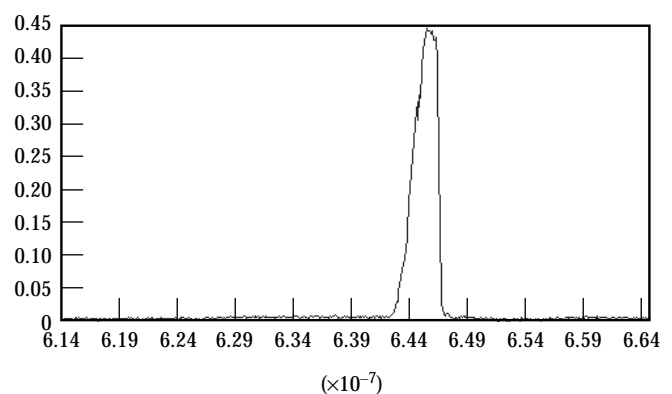


FIGURE 3. Optical pulse with a contrast ratio of 175:1.
(40-60-1198-2258pb01)

- The Plasma Electrode Pockels Cell (PEPC) prototypes underwent numerous mechanical and optical tests during the third quarter to validate the design. The kinematic mount design was tested to demonstrate adequate repeatability, capture range, and reliable operation of the mechanisms. The design performed very well overall, and minor modifications were noted for the production hardware. Vibration testing was completed to provide data for system stability performance models. A detailed tolerance analysis was completed for the PEPC, accounting for insertion/removal, alignment, structure and manufacturing tolerances. Optical performance of the cell under nominal conditions demonstrated that the design exceeds requirements for both “on” and “off” states. The design of the PEPC assembly fixture was completed, and the drawings are being reviewed. The PEPC front-end processor (FEP) prototype was deployed in the PEPC Lab to test compatibility of the controls with the harsh EMI environment of the PEPC.
- The Power Conditioning System Mid-Title II (65%) design review was held in April, and the design was commended by the review committee. A full prototype of the Power Conditioning System module was completed with the procurement of parts for the first-article module. Actual procurement of the first-article components will provide for firm cost estimates for production. Nearly all components arrived during the past quarter, and assembly and installation has begun. A variety of critical fault modes were simulated using the prototype module, including capacitor and bus faults. The system performed as expected and minimal damage to the hardware was sustained. Most notably, the 1.4-mega-ampere bus fault validated the performance of the module enclosure, blast doors, and fire prevention strategy. The ST-300 switch testing was completed in May. Testing of the ST-300E at greater than 540 kA indicates that switch lifetime will be in excess of 1500 shots.

Beam Transport System. In this quarter, all major structural and vessel packages for upcoming procurements were finalized and reviewed. The majority of laser bay steel structures were issued for bid. Contracts for the laser bay steel-mill order and the fabrication of spatial filter vacuum vessels were awarded. Shipment of 1000 tons of stainless vessel plate was initiated. Over 500 drawings were completed and released under Configuration Management. Much progress was made in streamlining the submittal process to facilitate the timely release of procurement packages. Construction

Planning activities developed into focus groups for the PASS, the War Zone (i.e., the optical system in the TSF optical plane area), Periscope (the structure that supports the PEPC, polarizer, laser mirrors LM2 and LM3), and Switchyards to establish more detailed links in the Integrated Project Schedule.

- Production of the spatial filter stainless plate is near completion with final product completion slipped to July and final invoicing anticipated by the end of August. Shipment of plate material to vessel fabricators is in progress and approximately 60% complete. Title II procurement review was completed for the spatial filter vacuum vessels, including approval of end vessel and center vessel engineering safety notes. Contracts were released in June for vacuum vessel fabrication.
- The detailed drawings for the Switchyard Beam Tubes are 95% complete. The horizontal quads remain to be detailed and should be completed by early July.
- The Roving Mirror Diagnostic Enclosure design is proceeding. Substantial progress was made incorporating updated interfacing structures and assemblies into the Pro-E model. The updated assembly details allow for development of part details based on real fit and dimensional constraints.
- Design development was concentrated on the large interstage components consisting of docking frames at the spatial filter end vessels and at the Switchyard wall to ensure fabrication and delivery do not impact critical path closure of facility openings. Planning and preliminary development of options and methods for cleaning beam tube enclosures is progressing.
- During this quarter the Spatial Filter Vacuum System Title II 100% Design Review was completed.
- The Switchyard #2 structure drawing package was completed and submitted into Configuration Management. The Title II Procurement Review for SY#2 was scheduled for early July, and the draft Statement of Work and fabrication specification were distributed for comment.
- The Power Amplifier, Main Amplifier, Laser Mirror 1, and Periscope support structure design drawings were completed. The Laser Bay Support Structures Fabrication Specification is completed. The CSF Optical Bench, TSF Optical Bench, Injection Structure, and PASS design calculations were completed. Thermally sprayed aluminum was chosen to coat the interior of the Laser Mirror 1 and the Periscope after examining many paints, ceramic, and thermal metallic

applications. The aluminum coating will be mechanically finished to a 125-rms finish to accommodate cleaning.

- A review of thermal analysis in the Laser Bays was presented. A significant conclusion was that the fluorescent lights under the Laser Bay beam cavities will adversely affect the wavefront of the laser. The solution was to provide motion detectors to power these lights only when needed, minimizing the thermal effects. In addition, a laser alignment control system override may be needed to shut lights off on demand to allow the structures to thermally stabilize.
- The 100% Title II review for the LRU Assembly Verification System was presented in May. The comments received were helpful and did not reveal any major issues.
- Good progress was made in developing and demonstrating an acceptable transport mirror attachment design. At an internal review in April, it was recommended to proceed with two concepts—an expansion arbor and an undercut. These have been tested at subscale. The results for both were very encouraging, with mirror surface deformations less than 20 nm.
- Testing of actuators is producing useful information for final design. The reliability, availability, and maintainability (RAM) testing of the harmonic drive actuators is well under way (>2 million cycles) and is showing that design to be robust. Testing of the friction drive actuator, planned for use on the periscope LRU, has revealed that there is some slippage between bearings and races that is load dependent. This error is being quantified to determine whether the controller can accommodate it or whether a design change will be necessary (i.e., use the harmonic drive actuator).
- Testing of prototype hardware continued. The shutter/beamdump (shown in Figure 4, below left) tests indicated that a design modification is needed to prevent the gate valve from binding during operation. Linear bearings will be used. RAM testing of this LRU will begin in July. The LM4 (switchyard mirror, below right) LRU is undergoing modal testing to confirm the finite element analysis of the individual mirror mounts, the frame assembly, and the kinematic mounts.



FIGURE 4. The shutter/beamdump testing, shown at left, and the LM4 switchyard mirror, shown on the right.
(40-60-1198-2259pb01)
(40-60-1198-2404pb01)

Integrated Computer Control System. Title II design progress is satisfactory. Five out of eight scheduled 100% reviews have been completed. Three reviews were completed in the third quarter: the Video Distribution System, a prototype of which was demonstrated at the review; the Supervisory Software, followed by two weeks of advanced training in object-oriented software engineering (construction of the first phase of the Production Prototype for demonstration in October 1998 has started); and the Communications System and Facility Environmental Monitor, also projected to meet deployment cost goals.

- Title II work is complete for computer systems. Installations of the NIF Testbed server computer, network diagnostic equipment, and numerous software items were completed in June, including graphical user interface tools, network management software, and security upgrades. Significant upgrades to the capability of the Rational Ada-95 compiler and ORBexpress object request broker for Solaris supervisory and FEP systems were successfully delivered as a result of outstanding collaboration between the vendors.
- The design for the first Production Prototype of the NIF Computer Control System software was featured at the 100% review. The prototype will be implemented during the fourth quarter to be demonstrated and submitted for testing in October 1998.
- Prototype testing of the t-1 Abort System on the programmable logic controller platform was performed. The system was simulated for one laser bay, and the terminal-to-terminal response time of the system was measured to be 1.8 ms. Although an additional 5 to 15 ms is expected when all overhead is accounted for, these results are well within the 70-ms real-time processing requirement of the system. The Industrial Controls Requirements and Design Description document was revised to reflect the final design, and the detailed failure modes and effects analysis was completed for the t-1 Abort System.
- Optics damage inspection data was generated from Beamlet experiments, locating an optic containing a broad spectrum of flaws at several positions in the beamline that was imaged repeatedly with various pinhole configurations, camera integration times, and other system configuration variations.
- A deployment model of the Control System software framework was created that allocates computer processes and key framework objects among the generic FEP, supervisory workstation, file server computers, and control points.

A specific deployment model of the first production prototype was then created that depicts the vertical slices (i.e., the subsystem architecture from FEP level to supervisory level) to be built for all supervisory applications and participating FEPs.

Optomechanical Systems Management. Title II design activity is moving towards completion in several areas. The LRU Assembly Verification System completed its 100% design review, and the drawing package was released under Configuration Management (CM). Optical design prepared for its upcoming 100% review. Internal reviews of subsystems in final optics resolved lingering, detailed design questions. The final optics assembly (FOA) prototype hardware (full-scale) was assembled, and integrated testing began. The shutter beamdump hardware was received for validation testing, and the transport mirror assembly was assembled and underwent modal testing.

Optical Design

- The final optics damage inspection system design was modified to use only fused silica components. This reduces the susceptibility of the system to damage due to background radiation (neutron-activated) in the target chamber. The design was further improved to reduce the sensitivity to element decenter and tilts. The optical design of the final optics damage-inspection system was presented at the 65% review for that system with no optical design issues identified.
- The final optical design detail for the transport mirrors was described in a memo. Target area mirrors LM6 to LM8 should be offset slightly to maximize use of the mirrors' clear aperture. This information was communicated to mechanical design groups in optical mounts and target area structures for inclusion in their detailed Pro-E models.
- Ghost workshop #3 was held in May to discuss the extensive analysis that has been performed on stray light in the FOA. Numerous threatening ghosts near the mechanical structures have been identified, their fluences estimated, and areas for absorbing materials or baffles identified.
- Optical fabrication drawings for the transport mirrors were released (blank, finished, and coated). The fused silica blank drawings were revised based on a request from Optics Manufacturing. Thus, 60 drawings needed for large optics manufacturing are under CM. The release of the six KDP crystal drawings needed for Title II is being paced by resolution of detailed specifications and associated metrology for the doubler and tripler.

Optical Components. The first NIF production optics order has been placed with the awarding of polarizer and LM3 mirror BK7 substrates. Due to long lead times, polarizer substrates for pilot production were ordered more than a year ago from Schott and Ohara. Mirror BK7 substrates were awarded to Ohara and Pilkington for pilot production with fixed price annual options for all of production.

- Mirror substrate blank drawings have been revised and released based on final dimensions and specifications. Firm fixed price contracts were awarded in June for mirror substrates for the NIF mirror pilot, with firm fixed price annual options for production of all the glass required for the NIF. Competitive bids were received from four glass companies, and awards were made to two vendors: Ohara and Pilkington. Each received a contract in June for one-half of the pilot quantity of mirror substrates.
- The polarizer substrate blank drawing was revised and released based on final dimensions and specifications. Firm fixed price contracts were awarded to Schott and Ohara in June for polarizer substrates for the first half of NIF production, with firm fixed price options for the remaining half of production to be awarded in FY01.
- Extensive testing of a variety of materials by laser exposure, flashlamp exposure, and cleaning has shown that burnished, thermally sprayed aluminum meets all performance requirements for the interior of the laser by a wide performance margin.

Laser Control. The last of the 65% design reviews were completed in May, and Laboratory activity supporting prototype testing continued to increase.

- The 65% design reviews for Alignment Systems, Final Optics Damage Inspection, and Pulse Synchronization were presented during the third quarter for a total number of 22 Beam Control reviews during Title II. All remaining reviews will be at the 100% level.
- Initial measurements of optics transmission degradation in vacuum and in static nitrogen or argon environments suggest that parts in static gas are less vulnerable to outgassing than those in vacuum, and that the specification for outgassing in vacuum enclosures may have to be tightened.
- Most of the input sensor optical component drawings have been released and are being sent out for prototype fabrication. Mechanical fabrication will take less time, and most mechanical drawings are in checking. Some prototype mechanical parts are already on order, including the two-position shutter and optics insertion

device that will also be used in other locations.

- The first prototype light source unit was assembled for the LM3 centering location. It will provide two pairs of 1.05- μ m beams for comparison with similar reference sources at LM1 and the FOA.
- The optical configuration drawing for the Output Sensor was completed. Assembly of the prototype Output Sensor was begun early in the quarter and is now complete. The test stand for the sensor package was also completed, and the package and test stand are now undergoing integrated testing.
- The lab setup for integrated testing of all power measurement components including Output Sensor fiber launch optics, fiber bundles, fiber bundle-to-photodiode coupler optics, photodiode, signal dividing transformer, and transient digitizer was assembled in the Optical Sciences Laboratory.
- A prototype local-energy node board including the latest dynamic range enhancements was prepared for use with the Preamplifier Module prototype. Its performance will be verified by calibrated test equipment available in Nova.
- The Raytheon deformable mirror prototype was delivered and is ready for testing in the NIF Wavefront Systems Laboratory. The ThermoTrex deformable mirror prototype has not been delivered, but the acceptance tests at ThermoTrex were completed. Finite-element models of both vendor mirrors were generated at Livermore to calculate influence functions for inclusion in the wavefront correction modules of the NIF propagation codes.
- The completeness of the NIF beamline aberration model was improved by the addition of mounting and gravity sag aberration estimates. The LLNL-developed finite-element model influence functions for the Raytheon mirror were put in proper form for use in the adaptive optics part of the propagation code, and actual calculations incorporating these changes have recently begun.

Target Experimental Systems

- The Target Chamber Final Design Review was successfully completed in May. Comments from that review have been collected and initial replies issued. The majority of the 18-sphere plate sections have had the weld joint configuration machined at Precision Component Company. The first three plates were shipped to Pitt-Des Moines in Pittsburgh for a trial fit to evaluate the effectiveness of the shipping cradles, fitting gear, handling procedures, and

overall matching of the three plates that will form the bottom of the target chamber.

- Construction work on the target chamber temporary enclosure, built on the E7 parking lot, continues with the completion of the 60-ft-diam, 62-ft-high enclosure. The enclosure is similar to an oil storage tank. It is made from 0.25" steel plates, seven courses high. A polar crane, HVAC, insulation, lights, and a removable roof will be added.
- The prototype beamdump was placed on Nova, and samples changed out weekly for three weeks of mostly gas-bag shots. An additional fused silica optic was added to the samples for off-line laser damage studies. The beamdump survived without excessive stainless steel ablation. Then, the prototype beamdump was placed back on Nova for a week of hohlraum shots. After a week of high-yield shots, the beamdump will be removed from the chamber and additional analysis performed.
- The investigation of the trade-offs between increased protective disc sizes for the target positioner and the need to clad some portion of the cryostat itself has been carried forward. Although a larger protective disc, which can completely shield the cryostat, gives rise to more ablation than the combined ablation from a smaller disc and the cryostat, the difference may not be enough to warrant periodic recoating of the cryostat; as the total ablation of relatively benign B_4C is still less than the amount of debris from the target assembly and the first wall. It now appears that a sufficient quantity of cryogenics for several days' holding can be accommodated in a cryostat of a geometry that can be completely shielded from target x rays.
- A web page has been developed to share diagnostic design information with representatives from LLNL, LANL, SNL, LLE, and AWE. The web page is still under review for content and organization and will soon be password accessible by diagnostic users.
- A design review for the NIF Grounding and Shielding Plan review was conducted in April, and no significant problems were identified in the review. The new draft of the NIF Electrical Grounding, Shielding & Isolation Plan has been entered into Project Database Management for review. A detailed analysis of electrical noise induced in cables in the Target Bay was conducted, and the design for the Target Chamber Ground Monitor System is being developed using commercial ground fault monitor/alarm systems.
- As a result of revised calculations performed by CSA for the seismic loads applied to the top of the pedestal and the target chamber to floor restraints, there has been some concern that the loads may exceed cited loads that were given to Parsons in an interface control document (ICD) in August 1997. Considerable design and analysis effort has been expended to resolve the differences between the existing calculations.
- A revised tritium usage projection for NIF has modified plans for implementation of the tritium-related systems. The schedule for implementation of all environmental protection elements has been extended.
- The 100% Design Review for Target Area Utilities & Cable Trays was held in June. No significant design action items were identified. All Title II deliverables have been completed and submitted to the Project Office.

Final Optics Assembly

- Significant progress was made in understanding and projecting the frequency conversion performance for the NIF final optics design. At a scientific review held in April, the converter design, its requirements, and error budget were presented. Requirements from this budget have since been flowed down to metrology equipment, crystal fabrication, coating performance, and mount tolerances.
- As a result of the intensive Beamlet experiments and the change-out/testing of different optical components, the single prototype final-optics cell has been assembled and disassembled many times. This heavy use has proven the robustness of the mechanical design and led to development of very detailed procedures for clean assembly.
- Major pieces of prototype hardware were assembled in the high bay of Building 432: the vacuum isolation valve, the calorimeter chamber, debris shield modules, four optics modules (one manufactured as a welded assembly and three by a casting process), and the large test stand. The integrated testing of the full-scale assembly began. The orientation of the FOA shown in Figure 5 simulates installation on the bottom half of the target chamber. Planned tests include mechanical fit-up and handling, vacuum pumping rates, cleanliness evaluations, and in-situ operation of debris shield cassette.
- The first round of debris shield cassette testing for cleanliness was completed. Preliminary results indicate that some minor design modifications are needed to eliminate sag and "walk" problems as the slide exits the Nylatron edge guides.

- The design progress toward final, detailed FOA design drawing packages was good for several subsystems. The final optics cell is in excellent shape, the vacuum isolation valve is nearly complete, and the alignment fiducial arm design drawings are in checking.
- Good progress was made on CAVE (crystal alignment and verification equipment). The “first light” milestone was met in April. Semi-automated measurements of frequency conversion of a doubling crystal (2 ω rocking curve) were completed in May. The control software for fully automated, full-aperture scanning measurements is proceeding well and will be operational next quarter. Detailed, engineering subsystem verifications (e.g., stability of mounts, performance of autocollimators) are under way.

Operations Special Equipment

Title II design progress is proceeding well. Hardware prototyping continues to increase in volume and in data collected. Several internal key milestones were accomplished this quarter.

- An integrated 3D model of the Laser and Target Area Building (LTAB), OAB, and corridor is in progress for a Material Flow design review. The process to bring manageable-size files together
- and maintain a high level of detail has been developed by using a series of benchmark tests, resulting in a process that allows the designers to use Intergraph files with 3D Studio, gain a huge time savings, and maintain a high level of detail for modeling.
- The detailed design in the bottom loading (BL), top loading (TL), side loading (SL), switchyard, and target area delivery systems is progressing well. The docking structure for the BL system has been initiated and will be used for the canister docking as well as for the insertion testing of the PEPC, Spatial Filter, and Periscope LRUs.
- The Final Design Review for the Laser Bay Transport System with RedZone Robotics/AGV Products was completed this quarter.
- The assembly and testing of the prototype hardware is progressing well. All components are in for the flashlamp cover removal mechanism and assembly was started in May. Load testing of the permanent carriage for the BL universal system was completed in May, and some redesign is expected due to the results. A vacuum cover removal operation was completed with the TL scissors/latching mechanism as well, and the system performed flawlessly.
- The OAB hardware designs and the simulations continue to progress well. All ICDs with optical mounts, amplifier, and alignment systems groups are revised and signed. A top-level assembly model for the OAB was completed this quarter, and the docking station and assembly stand concepts are complete for the amplifier and the generic docking ports.
- The Supervisory Controls team has made excellent progress, completing the Mid-Title II (65%) Review in June, with strong project endorsement and interactions. The software requirements specification and rational rose model for the supervisory server was completed. A prototype implementation of the supervisory server framework and event services, integrated with the FEP control software, is in progress.

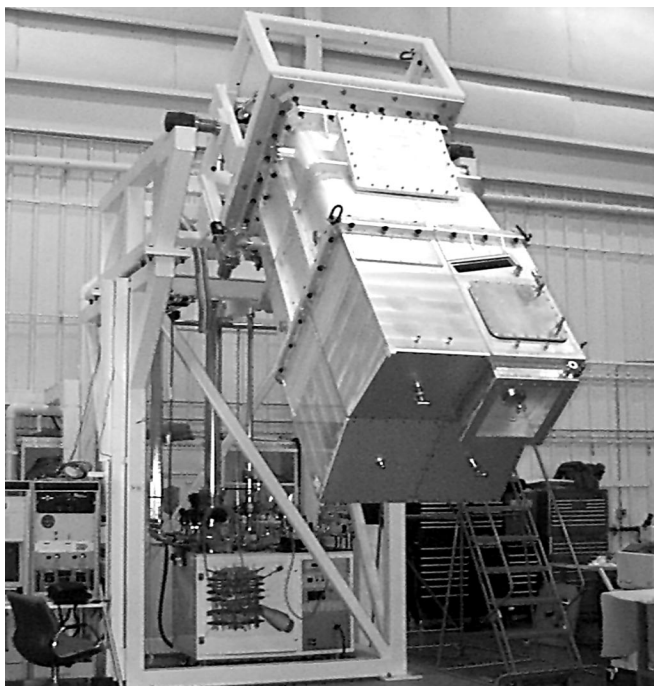


FIGURE 5. Prototype FOA hardware being assembled in the high bay of Building 432. (40-60-1198-2260pb01)

Start-Up Activities

- The month-end June status of the Integrated Project Schedule showed no impact to Level 0–3 milestones. Work continues with the Conventional Facilities group to establish a baseline for CSP-9 and CSP-6/10. Once baselines are established, Project Milestone dates and definitions will be adjusted.
- As part of the FY99 CAP planning process, Start-Up has completed definition of the FY99 workplan to develop the present First Bundle

Operational Test Plan into a complete set of Operational Test Procedures. Additionally, the Start-Up Preliminary Staffing Plan for the First Bundle was completed in detail. A detailed list of activities for the Start-Up group was laid out for FY00 and FY01. The composition of the Start-Up Laser Operations teams was defined, in addition to the scientific support staff, who will provide expert assistance and handle data processing and evaluation of the operational test data.

- Optics Processing is the first of 12 to 15 functional areas to work with Start-Up in preparing operations training materials following a performance-based training method. A schedule driven by Project milestone dates and Title II 100% design review dates has been developed to determine the order in which Start-Up will work with various groups to prepare training materials and operations procedures.
- Start-Up staff has been working on the conceptual design of a metrology station to measure wavefront errors in mounted optics. This continued through May and June with the goal of a conceptual review held the first week in June. A solid concept was developed to test LM4, LM5, LM6, LM7, LM8, amplifiers, and PEPC.
- A plan has been developed laying out all NIF operational readiness requirements through the end of the project and beyond. This plan is presently being reviewed internally and will be discussed with DOE within a few months.

Optics Technology

Facilitization is moving well at all NIF vendors as they prepare for pilot production in late FY98 or in FY99. Zygo and Corning will both begin their pilots in the fourth quarter in portions of their facilities while they complete facilitization tasks in other areas. Schott, Hoya, and Tinsley will begin their pilots in the first quarter of 1999. KDP rapid growth and finishing pilots have already started at LLNL, and the external-vendor rapid-growth pilots are set to begin in early FY99 at Cleveland Crystal and Inrad. Facilitization at LLE and Spectra-Physics is in good shape to begin their pilots later in FY99. The longest lead substrate material, polarizer substrates, has already been received for pilot production, and orders are in place for mirror and polarizer substrate production.

- The last two crystal growth stations at LLNL became fully operational, went through their first validation tests, and are now being used for growth runs. Coating development at LLNL was completed and the first convex aluminum platform was coated with the improved process. Six tanks are now running as part of the LLNL pilot.
- Fabrication of the Finishing Diamond Flycutting

Machine by the Moore Tool Company in Bridgeport, Connecticut, is progressing well. Moore Tool plans to ship the machine by the end of July 1998, after debugging the major mechanical and control systems. The flycutter design and most major assembly are complete. LLNL site preparations for accepting the Moore machine are also complete.

- LLNL has agreed to Corning's proposed plan to accelerate pilot and production of fused silica in FY99 to take advantage of the current world slump in the fused silica market, driven by a drop in the semiconductor industry. Corning will be ready to ship pilot glass in October, matching the original schedule and eliminating a previously expected slip of three months. Corning demonstrated a new inspection technique that will allow them to detect solid inclusions much smaller than their current 80- μ m limit. If required, this technique may be used as a factory quality control tool to ensure 3 ω glass meets the proposed new 3 ω inclusion specification.
- Tinsley is making excellent progress on their NIF Lenses and Windows Finishing Facility building. Although the new NIF building will not be completed until November, pilot production of NIF optics will begin in October (completing a DOE/OAK Performance Measurement Milestone). High-volume demonstration runs will be carried out in the current facility using NIF equipment and NIF processes to fabricate lenses for the NIF. Production of pilot optics will switch to the new building when available midpilot.
- Initial acceptance testing of the cleaning line equipment for Zygo's facility was done at the equipment manufacturer, Forward Technology. Installation at Zygo is approximately 80% complete. Zygo has been evaluating cleaning detergents on small material samples with their existing equipment.
- Facilitization at Spectra-Physics is proceeding on schedule. The interferometer isolation pad was poured and is curing. Interestingly, NIF construction has delayed availability of concrete at Spectra-Physics. Walls for the metrology labs are in construction as are air-handling systems. Facilitization at LLE is proceeding on schedule. Construction has begun on conditioning labs, and the contract was awarded for the 1 ω interferometer at LLE. The counter rotating planetary hardware at LLE has also been assembled and cleaned.
- A WYKO white light microinterferometer was installed and performance verified during June. The unit is being used to verify the etch depth of samples from etch monitor development. Modifications are being made to enable this

instrument to also provide roughness and power spectral density waviness II measurements for mirrors, lenses, windows, crystals, and amplifier slabs.

Upcoming Major Activities

During the fourth quarter of FY98, Conventional Facilities will complete the CSP-4 erection of the Laser Building steel and much of the roofing and siding. In

the Target Building, the concrete walls for the switchyards and the Target Bay cylinder will begin to rise. The OAB steel work will be completed, and the building will be dried-in. In Special Equipment, the majority of the 65% and 100% design reviews will be completed, and procurements will continue to be initiated for Beam Transport items such as the Laser Bay Structures. In Optics, preprocurement reviews will be held for the major components, and the vendor facilitization activities will continue.

PUBLICATIONS AND PRESENTATIONS

APRIL–JUNE 1998

A

Amendt, P., Turner, R. E., Landen, O., Glendinning, S. G., Kalantar, D., Cable, M., Decker, C., Suter, L. J., Wallace, R., and Hammel, B. A., *High-Convergence Indirect-Drive Implosions on OMEGA: Design and Simulations*, Lawrence Livermore National Laboratory, Livermore, CA, UCRL-JC-130677 ABS. Prepared for 28th Annual Anomalous Absorption Conf, Bar Harbor, ME, Jun 14, 1998.

Anderson, O. A., and Logan, B. G., *Low Emittance Beam Extraction from Laser-Driven Multicharged Ion Sources*, Lawrence Livermore National Laboratory, Livermore, CA, UCRL-JC-131120-DR. Prepared for 6th European Particle Accelerator Conf, Stockholm, Sweden, Jun 23, 1998.

B

Balkcum, A. J., McDermott, D. B., Phillips, R. M., and Luhman Jr., N. C., "High-Power Coaxial Ubitron Oscillator: Theory and Design," *IEEE Trans. Plasma Sci.* **26** (3), 548–555 (1998).

Berger, R. L., Cohen, B. I., Langdon, A. B., MacGowan, B. J., Rothenberg, J., Still, C. W., Williams, E. A., Lefebvre, E., and DuBois, D. F., *3D Model for the Growth, Saturation, and Competition of Filamentation, SBS and SRS*, Lawrence Livermore National Laboratory, Livermore, CA, UCRL-JC-130349 ABS. Prepared for 28th Annual Anomalous Absorption Conf, Bar Harbor, ME, Jun 14, 1998.

Berger, R. L., Rothenberg, J. E., Still, C. H., Langdon, A. B., MacGowan, B. J., Williams, E. A., and Lefebvre, E., *Polarization and Spectral Dispersion Smoothing: Effects on SBS, SRS, and Filamentation*, Lawrence Livermore National Laboratory, Livermore, CA, UCRL-JC-130578 ABS. Prepared for 28th Annual Anomalous Absorption Conf, Bar Harbor, ME, Jun 14, 1998.

Berger, R. L., Still, C. H., Williams, E. A., and Langdon, A. B., *On the Dominant and Subdominant Behavior of Stimulated Raman and Brillouin Scattering Driven by Nonuniform Laser Beams*, Lawrence Livermore National Laboratory, Livermore, CA, UCRL-JC-129673 Rev 1. Submitted to *Phys. of Plasmas*.

Bernat, T. P., *National Plan for Ignition*, Lawrence Livermore National Laboratory, Livermore, CA, UCRL-JC-130325 ABS. Prepared for Target Fabrication Mtg '98, Jackson Hole, WY, Apr 19, 1998.

Bodner, S. E., Colombant, D. G., Gardner, J. H., Lehmberg, R. H., Obenschain, S. P., Phillips, L. S., Schmitt, A. J., Sethian, J. D., McCrory, R. L., Seka, W., Verdon, C. P., Knauer, J. P., Afeyan, B. B., and Powell, H. T., *Direct-Drive Laser Fusion: Status and Prospects*, Lawrence Livermore National Laboratory, Livermore, CA, UCRL-ID-129418; *Phys. Plasmas* **5** (5), SI:1901–1918 (1998).

Bradley, D. K., Delettrez, J. A., Epstein, R., Town, R. P. J., Verdon, C. P., Yaakobi, B., Regan, S., Marshall, F. J., Boehly, T. R., Knauer, J. P., Meyerhofer, D. D., Smalyuk, V. A., Seka, W., Haynes Jr., D. A., Gunderson, M., Junkel, G., Hooper Jr., C. F., Bell, P. M., Ognibene, T. J., and Lerche, R. A., "Measurements of Core and Pusher Conditions in Surrogate Capsule Implosions on the OMEGA Laser System," *Phys. Plasmas* **5** (5), SI:1870–1879 (1998).

Budil, K. S., Remington, B. A., Gold, D. M., Estabrook, K., Kane, J., Bell, P. M., Pennington, D., Brown, C., Key, M. H., and Perry, M. D., *Blast Wave Diagnostic for the Petawatt Laser System*, Lawrence Livermore National Laboratory, Livermore, CA, UCRL-JC-130955. Prepared for 12th Topical Conf on High-Temperature Plasma Diagnostics, Princeton, NJ, Jun 7, 1998.

Budil, K. S., Remington, B. A., Gold, D. M., Estabrook, K., Lerche, R., Bell, P. M., Koch, J. A., Kane, J. O., Pennington, D., and Brown, C., *Diagnosis of the Propagation of a Blast Wave Generated by the Petawatt Laser System*, Lawrence Livermore National Laboratory, Livermore, CA, UCRL-JC-130324 ABS. Prepared for 28th Annual Anomalous Absorption Conf, Bar Harbor, MA, Jun 15, 1998.

C

Celliers, P. M., Collins, G. W., Da Silva, L. B., Gold, D. M., Cauble, R., Wallace, R. J., and Foord, M. E., *Shock Transformation of Deuterium from Molecular Fluid Insulator to Liquid Metal*, Lawrence Livermore National Laboratory, Livermore, CA, UCRL-JC-130339 Rev 1. Submitted to *Phys. Rev. Lett.*

Celliers, P. M., Estabrook, K. G., Wallace, R. J., Murray, J. E., Da Silva, L. B., MacGowan, B. J., Van Wonterghem, B. M., and Manes, K. R., "Spatial Filter Pinhole for High-Energy Pulsed Lasers," Lawrence Livermore National Laboratory, Livermore, CA, UCRL-JC-124029; *Appl. Opt.* **37**(12), 2371–2378 (1998).

Chang, J. J., Dragon, E. P., and Bass, I. L., *315 W Pulsed-Green Generation with a Diode-Pumped Nd:YAG Laser*, Lawrence Livermore National Laboratory, Livermore, CA, UCRL-JC-130462 ABS&SUM. Prepared for Conf on Lasers and Electro Optics '98, San Francisco, CA, May 3, 1998.

Chang, J. J., Warner, B. E., Dragon, E. P., and Martinez, M., *Precision Micromachining with Pulsed Green Lasers*, Lawrence Livermore National Laboratory, Livermore, CA, UCRL-JC-130826. Submitted to *J. of Laser Applications*.

Chang, J., Martinez, M., Cochran, C., Dingus, C., and Kuklo, T., *Precision Laser Machining with Advanced Solid-State Lasers*, Lawrence Livermore National Laboratory, Livermore, CA, UCRL-ID-130458.

Collins, G. W., Celliers, P., Da Silva, L. B., Cauble, R., Gold, D., Foord, M., Budil, K. S., Stewart, R., Holmes, N. C., and Ross, M., *Equation of State Measurements of Hydrogen Isotopes up to 3 Mbar*, Lawrence Livermore National Laboratory, Livermore, CA, UCRL-JC-130611 ABS. Prepared for 28th Annual Anomalous Absorption Conf, Bar Harbor, ME, Jun 14, 1998.

Collins, G. W., Celliers, P., Da Silva, L. B., Cauble, R., Gold, D., Foord, M., Budil, K. S., Stewart, R., Holmes, N. C., Ross, M., Hammel, B. A., Kilkenny, J. D., Wallace, R. J., and Ng, A., *Equation of State Measurements of Hydrogen Isotopes on Nova*, Lawrence Livermore National Laboratory, Livermore, CA, UCRL-JC-129033; *Phys. Plasmas* **5**(5), SI:1864–1869 (1998).

Correll, D., *Monthly Highlights*, April 1998, Lawrence Livermore National Laboratory, Livermore, CA, UCRL-TB-128550-98-7.

Crane, J. K., Wilcox, R. B., Hopps, N., Browning, D., Martinez, M. D., Moran, B., Penko, F., Rothenberg, J. E., Henesian, M., and Dane, C. B., *Optical Pulse Generation System for the National Ignition Facility*, Lawrence Livermore National Laboratory, Livermore, CA, UCRL-JC-130953 ABS. Prepared for 1998 American Nuclear Society Annual Mtg, Nashville, TN, Jun 7, 1998.

D

Dane, C. B., Hackel, L. A., Daly, J., and Harrison, J., "Shot Peening With Lasers," *Advanced Materials & Processes*, 37–38 (1998).

De Yoreo, J. J., Yan, M., Runkel, M. J., Woods, B. W., Ryon, R. W., Carman, L., Zaitseva, N. P., Rek, Z. U., Liou, L. W., and Demos, S. G., *Characterization of Optical Performance and Defect Structures in Rapidly-Grown Crystals of KDP and DKDP*, Lawrence Livermore National Laboratory, Livermore, CA, UCRL-JC-130623 ABS. Prepared for 16th Conf on Crystal Growth and Epitaxy, Fallen Leaf Lake, CA, Jun 7, 1998.

Decker, C. D., London, R. A., Harte, J. A., Powers, L. V., and Trebes, J. E., *Electron Density Measurements in Hohlraums Using Soft X-Ray Deflectometry*, Lawrence Livermore National Laboratory, Livermore, CA, UCRL-JC-130678. Submitted to *Phys. Rev. E*.

Decker, C., Hinkel, D. E., Berger, R. L., Williams, E. A., Suter, L. S., MacGowan, B. J., Kirkwood, R. K., and Lours, L., *Surrogate Target Designs for Emulating NIF Plasma Conditions*, Lawrence Livermore National Laboratory, Livermore, CA, UCRL-JC-130579 ABS. Prepared for 28th Annual Anomalous Absorption Conf, Bar Harbor, ME, Jun 14, 1998.

E

Estabrook, K., Drake, R. P., Remington, B., Glendinning, G., Budil, K., Munro, D. H., Suter, L. J., Harte, J. H., Zimmerman, G. B., and Bailey, D. S., *LAS-NEX Simulations of Astrophysical Phenomena: Supernova Shocks, Plasma Jet, Micrometeor Cratering and Blast Wave on the Nova Laser*, Lawrence Livermore National Laboratory, Livermore, CA, UCRL-JC-130344 ABS. Prepared for 28th Annual Anomalous Absorption Conf, Bar Harbor, ME, Jun 14, 1998.

Estabrook, K., Drake, R. P., Remington, B., Glendinning, G., Budil, K., Stone, J., Farley, D., Wood-Vasey, M., Munro, D. H., and Suter, L. J., *LASNEX Simulations of Astrophysical Phenomena: Supernova Shocks, Plasma Jet, Micrometeor Cratering and Blast Wave on the Nova and Petawatt Laser*, Lawrence Livermore National Laboratory, Livermore, CA, UCRL-JC-130983-EXT-A. Prepared for 28th Annual Anomalous Absorption Conf, Bar Harbor, ME, Jun 14, 1998.

Estabrook, K., Glenzer, S., Back, C. A., Rozmus, W., Zimmerman, G. B., Lee, R. W., MacGowan, B., De Groot, J. S., Griem, H., and Harte, J. A., *LLNL Nova Laser Irradiated Gold Disk Experiments Compared to LASNEX Simulations*, Lawrence Livermore National Laboratory, Livermore, CA, UCRL-JC-130343 ABS. Prepared for 28th Annual Anomalous Absorption Conf, Bar Harbor, ME, Jun 14, 1998.

Estabrook, K., Glenzer, S., Back, C. A., Rozmus, W., Zimmerman, G. B., De Groot, J. S., Lee, R. W., Wilson, B., MacGowan, B., and Griem, H., *LLNL Nova Laser Irradiated Gold Disk Experiments Diagnosed with Thomson Scattering Compared to LASNEX Simulations*, Lawrence Livermore National Laboratory, Livermore, CA, UCRL-JC-130984-EXT-A. Prepared for 28th Annual Anomalous Absorption Conf, Bar Harbor, ME, Jun 14, 1998.

F

Feit, M. D., Komashko, A. M., Musher, S. L., Rubenchik, A. M., and Turitsyn, S. K., "Electron Cavitation and Relativistic Self-Focusing in Underdense Plasma," Lawrence Livermore National Laboratory, Livermore, CA, UCRL-JC-127909; *Phys. Rev. E* 57(6), 7122–7125 (1998).

Feit, M. D., Rubenchik, A. M., Kim, B. M., and Da Silva, L. B., "Physical Characterization of Ultrashort Laser Pulse Drilling of Biological Tissue," Lawrence Livermore National Laboratory, Livermore, CA, UCRL-JC-127269; *Appl. Surface Sci.* **129**, 869–874 (1998).

Feit, M., and Rubenchik, A. M., *Statistical Properties of Surface Laser Damage Thresholds*, Lawrence Livermore National Laboratory, Livermore, CA, UCRL-ID-130577.

G

Geddes, C. G. R., Kirkwood, R. K., Glenzer, S. H., Estabrook, K. G., Joshi, C., and Wharton, K. B., *Study of the Saturation of Stimulated Raman Scattering by Secondary Decays*, Lawrence Livermore National Laboratory, Livermore, CA, UCRL-JC-130328 ABS. Prepared for 28th Annual Anomalous Absorption Conf, Bar Harbor, ME, Jun 14, 1998.

Genin, F. Y., Salleo, A., and Campbell, J. H., *Nano-Second Laser Drilling in Fused Silica*, Lawrence Livermore National Laboratory, Livermore, CA, UCRL-JC-130690 ABS. Prepared for Gordon Research Conf, Andover, NH, Jun 7, 1998.

Glenzer, S. H., Weiland, T. L., Bower, J., MacKinnon, A. J., and MacGowan, B. J., *High-Energy 4ω Probe Laser for Laser-Plasma Experiments at Nova*, Lawrence Livermore National Laboratory, Livermore, CA, UCRL-JC-129603. Prepared for 12th Topical Conf on High-Temperature Plasma Diagnostics, Princeton, NJ, Jun 7, 1998.

H

Haan, S. W., *Hydrodynamic Instabilities in Indirect-Drive ICF*, Lawrence Livermore National Laboratory, Livermore, CA, UCRL-JC-130341 ABS. Prepared for 28th Annual Anomalous Absorption Conf, Bar Harbor, ME, Jun 14, 1998.

Hartemann, F. V., "High-Intensity Scattering Processes of Relativistic Electrons in Vacuum," Lawrence Livermore National Laboratory, Livermore, CA, UCRL-JC-130021; *Phys. Plasmas* 5(5), SI:2037–2047 (1998).

Hatchett, S. P., Wilks, S. C., and Perry, M. D., *Modeling Laser Driven Radiography*, Lawrence Livermore National Laboratory, Livermore, CA, UCRL-JC-130532 ABS. Prepared for 28th Annual Anomalous Absorption Conf, Bar Harbor, ME, Jun 14, 1998.

Hinkel, D. E., and Haan, S. W., *Work-in-Progress: the 350 eV NIF Target*, Lawrence Livermore National Laboratory, Livermore, CA, UCRL-JC-130350 ABS. Prepared for 28th Annual Anomalous Absorption Conf, Bar Harbor, ME, Jun 14, 1998.

Hinkel, D. E., Berger, R. L., Williams, E. A., Langdon, A. B., Lasinski, B. F., and Still, C. H., *Stimulated Brillouin Backscatter in the Presence of Transverse Plasma Flow*, Lawrence Livermore National Laboratory, Livermore, CA, UCRL-JC-130345 ABS. Prepared for 28th Annual Anomalous Absorption Conf, Bar Harbor, ME, Jun 14, 1998.

Hinkel, D. E., Berger, R. L., Williams, E. A., Langdon, A. B., Still, C. H., and Lasinski, B. F., *Stimulated Brillouin Backscatter in the Presence of Transverse Plasma Flow*, Lawrence Livermore National Laboratory, Livermore, CA, UCRL-JC-130345. Submitted to *Phys. of Plasmas*.

Hinkel, D. E., Williams, E. A., Berger, R. L., Powers, L. V., Langdon, A. B., and Still, C. H., "Propagation of Realistic Beams in Underdense Plasma," Lawrence Livermore National Laboratory, Livermore, CA, UCRL-JC-129025; *Phys. Plasmas* 5(5), SI:1887–1894 (1998).

Ho, D. D.-M., Harte, J. A., and Tabak, M., "Two Dimensional Simulations of a Radiation Driven Target with Two Sided Illumination for Heavy Ion Fusion," Lawrence Livermore National Laboratory, Livermore, CA, UCRL-JC-128287; *Nucl. Fusion* **38**(5), 701-709 (1998).

Hopps, N. W., Wilcox, R. B., Hermann, M. R., Martinez, M. D., Padilla, E. H., and Crane, J. K., *Optimisation of the Alignment Sensitivity and Energy Stability of the NIF Regenerative Amplifier Cavity*, Lawrence Livermore National Laboratory, Livermore, CA, UCRL-JC-130961 ABS. Prepared for 3rd Intl Conf on the Solid-State Lasers for Applications (SSLA) to Inertial Confinement Fusion (ICF), Monterey, CA, Jun 7, 1998.

J

Jones, O. S., Speck, D. R., Haan, S. W., and Suter, L. J., *NIF Power Balance*, Lawrence Livermore National Laboratory, Livermore, CA, UCRL-JC-130582 ABS. Prepared for 28th Annual Anomalous Absorption Conf, Bar Harbor, ME, Jun 14, 1998.

K

Kalantar, D. H., Chandler, E. A., Colvin, J. D., Lee, R., Remington, B. A., Weber, S. V., Wiley, L. G., Failor, B. H., Hauer, A., and Wark, J. S., *Transient X-Ray Diffraction Used to Diagnose Shock Compressed Si Crystals on the Nova Laser*, Lawrence Livermore National Laboratory, Livermore, CA, UCRL-JC-129861 DR. Prepared for 12th Topical Conf on High-Temperature Plasma Diagnostics, Princeton, NJ, Jun 7, 1998.

Kalantar, D. H., Chandler, E. A., Colvin, J. D., Mikaelian, K., Remington, B. A., Weber, S. V., Wiley, L. G., Hauer, A. A., Wark, J. S., Meyers, M. A., and Ravichandran, G., *Transient X-Ray Diffraction of Shock Compressed Crystals Using the Nova Laser*, Lawrence Livermore National Laboratory, Livermore, CA, UCRL-JC-129270 ABS Rev. Prepared for The Minerals, Metals, and Materials Society Fall Mtg, Rosemont, IL, Oct 11, 1998.

Kalantar, D. H., Chandler, E. A., Colvin, J. D., Mikaelian, K., Remington, B. A., Weber, S. V., Wiley, L. G., Wark, J. S., Hauer, A. A., and Failor, B., *High Pressure Solid State Hydrodynamic Instability Growth Experiments on the Nova Laser*, Lawrence Livermore National Laboratory, Livermore, CA, UCRL-JC-130588 ABS. Prepared for 28th Annual Anomalous Absorption Conf, Bar Harbor, ME, Jun 14, 1998.

Kalantar, D. H., Remington, B. A., Chandler, E. A., Colvin, J. D., Weber, S. V., Wiley, L. G., Wark, J. S., Hauer, A. A., and Meyers, M. A., *High Pressure Solid State Experiments on the Nova Laser*, Lawrence Livermore National Laboratory, Livermore, CA, UCRL-JC-129810 DR. Prepared for 1998 Hypervelocity Impact Symp, Huntsville, AL, Nov 16, 1998.

Kane, J. O., Arnett, D., Remington, B. A., Glendinning, S. G., Wallace, R., Rubenchik, A., and Fryxell, B., *Supernova Experiments on the Nova Laser*, Lawrence Livermore National Laboratory, Livermore, CA, UCRL-JC-129000. Prepared for Second Oakridge Symp on Atomic and Nuclear Astrophysics, Oak Ridge, TN, Dec 2, 1998.

Kane, J. O., Drake, R. P., and Remington, B. A., *Evaluation of the Richtmyer-Meshkov Instability in Supernova Remnant Formation*, Lawrence Livermore National Laboratory, Livermore, CA, UCRL-JC-130957. Submitted to *Astrophys. J.*

Kauffman, R. L., Powers, L. V., Dixit, S. N., Glendinning, S. G., Glenzer, S. H., Kirkwood, R. K., Landen, O. L., MacGowan, B. J., Moody, J. D., Orzechowski, T. J., Pennington, D. M., Stone, G. F., Suter, L. J., Turner, R. E., Weiland, T. L., Richard, A. L., and Bain, M. A., "Improved Gas-Filled Hohlraum Performance on Nova with Beam Smoothing," Lawrence Livermore National Laboratory, Livermore, CA, UCRL-JC-128004; *Phys. Plasmas* **5**(5), SI:1927-1934 (1998).

Kauffman, R., *Monthly Highlights*, May 1998, Lawrence Livermore National Laboratory, Livermore, CA, UCRL-TB-128550-98-8.

Key, M. H., Cable, M. D., Cowan, T. E., Estabrook, K. G., Hammel, B. A., Hatchett, S. P., Henry, E. A., Hinkel, D. E., Kilkenny, J. D., Koch, J. A., Kruer, W. L., Langdon, A. B., Lasinski, B. F., Lee, R. W., MacGowan, B. J., MacKinnon, A., Moody, J. D., Moran, M. J., Offenberger, A. A., Pennington, D. M., Perry, M. D., Phillips, T. J., Sangster, T. C., Singh, M. S., Stoyer, M. A., Tabak, M., Tietbohl, G. L., Tsukamoto, M., Wharton, K., and Wilks, S. C., "Hot Electron Production and Heating by Hot Electrons in Fast Ignitor Research," Lawrence Livermore National Laboratory, Livermore, CA, UCRL-JC-129251; *Phys. Plasmas* **5**(5), SI:1966-1972 (1998).

Key, M. H., Wolfrum, E., Rose, S. J., Kalantar, D. H., Barbee, T. W., Demir, A., Kim, S., Lewis, C. L. S., Lin, J., and MacPhee, A., *Increase in the XUV Opacity of Al due to Shock Compression*, Lawrence Livermore National Laboratory, Livermore, CA, UCRL-JC-125446. Submitted to *Phys. Rev. Lett.*, May 19, 1998.

Kim, B. M., Feit, M. D., Rubenchik, A. M., and Mammini, B. M., "Optical Feedback Signal for Ultrashort Laser-Pulse Ablation of Tissue," Lawrence Livermore National Laboratory, Livermore, CA, UCRL-JC-128614; *Appl. Surface Sci.* **129**, 857-862 (1998).

Kirkwood, R. K., Glenzer, S. H., MacGowan, B. J., Estabrook, K. G., Berger, R. L., Williams, E. A., Moody, J. D., and Decker, C., *Scaling of SRS with Electron Temperature in Large Scale Plasmas*, Lawrence Livermore National Laboratory, Livermore, CA, UCRL-JC-130330 ABS. Prepared for 28th Annual Anomalous Absorption Conf, Bar Harbor, ME, Jun 14, 1998.

Koch, J. A., Back, C. A., Brown, C., Estabrook, K., Hammel, B. A., Hatchett, S. P., Key, M. H., Kilkenny, J. D., Landen, O. L., Lee, R. W., Moody, J. D., Offenberger, A. A., Pennington, D., Perry, M. D., Tabak, M., Yanovsky, V., Wallace, R. J., Wharton, K. B., and Wilks, S. C., "Time-Resolved X-Ray Spectroscopy of Deeply Buried Tracer Layers as a Density and Temperature Diagnostic for the Fast Ignitor," Lawrence Livermore National Laboratory, Livermore, CA, UCRL-JC-126309; *Laser and Particle Beams* **16**(1), 225–232 (1998).

Koch, J. A., Hatchett, S. P., Lee, R. W., Key, M. H., Landen, O. L., Brown, C., Hammel, B. A., Moody, J. D., Pennington, D., and Perry, M. D., *X-Ray Emission Spectroscopy of Deeply Buried Tracer Layers as a Deep-Heating Diagnosis for Fast Ignition Experiments*, Lawrence Livermore National Laboratory, Livermore, CA, UCRL-JC-130329 ABS. Prepared for 28th Annual Anomalous Absorption Conf, Bar Harbor, ME, Jun 14, 1998.

Koch, J. A., Landen, O. L., Barbee, T. W., Celliers, P., Da Silva, L. B., Glendinning, S. G., Hammel, B. A., Kalantar, D. H., Brown, C., and Seely, J., *High-Energy, High Resolution X-Ray Imaging Applications and Techniques for the National Ignition Facility*, Lawrence Livermore National Laboratory, Livermore, CA, UCRL-JC-129869-DR. Prepared for 12th Topical Conf on High-Temperature Plasma Diagnostics, Princeton, NJ, Jun 7, 1998.

Kruer, W. L., Campbell, E. M., Decker, C. D., Wilks, S. C., Moody, J., Orzechowski, T., Powers, L., Suter, L. J., Afeyan, B., and Dague, N., *Strongly-Driven Laser Plasma Coupling*, Lawrence Livermore National Laboratory, Livermore, CA, UCRL-JC-130610. Prepared for 1998 Intl Congress on Plasma Physics, Prague, Czech Republic, Jun 29, 1998.

Kruer, W. L., *Strongly-Driven Regimes of Laser Plasma Coupling*, Lawrence Livermore National Laboratory, Livermore, CA, UCRL-JC-130610 ABS. Prepared for 1998 Intl Congress on Plasma Physics, Prague, Czech Republic, Jun 29, 1998.

L

Landahl, E. C., Hartemann, F. V., Le Sage, G. P., White, W. E., Baldis, H. A., Bennett, C. V., Heritage, J. P., Luhmann Jr., N. C., and Ho, C. H., "Phase Noise Reduction and Photoelectron Acceleration in a High-Q RF Gun," Lawrence Livermore National Laboratory, Livermore, CA, UCRL-JC-130929; *IEEE Trans. Plasma Sci.* **26**(3), 814–824 (1998).

Langdon, B., MacGowan, B., Berger, R., Dixit, S., Feit, M., Hendrix, J., Hinkel, D., Kirkwood, R., Manes, K., and Miller, J., *Significance of Stimulated Brillouin and Raman Backscatter from the Target as a Source of Optics Damage in NIF/LMJ Lasers*, Lawrence Livermore National Laboratory, Livermore, CA, UCRL-JC-130526 ABS. Prepared for 28th Annual Anomalous Absorption Conf, Bar Harbor, ME, Jun 14, 1998.

Langer, S. H., *Comparison of the Floating Point Performance of Current Computers*, Lawrence Livermore National Laboratory, Livermore, CA, UCRL-JC-130869. Submitted to *Computers in Phys.*

Langer, S. H., Scott, H. A., Marinak, M. M., and Landen, O. L., *Modeling ICF Capsule Line Emission in 3 Dimensions*, Lawrence Livermore National Laboratory, Livermore, CA, UCRL-JC-130332 ABS. Prepared for 28th Annual Anomalous Absorption Conf, Bar Harbor, ME, Jun 14, 1998.

Lasinski, B. F., Langdon, A. B., Tabak, M., and Key, M. H., *PIC Simulations of Hole-Boring for Fast Ignitor Applications*, Lawrence Livermore National Laboratory, Livermore, CA, UCRL-JC-129304 ABS Rev. Prepared for 28th Annual Anomalous Absorption Conf, Bar Harbor, ME, Jun 14, 1998.

Latkowski, J. F., and Vujic, J. L., "Inertial Fusion Energy: A Clearer View of the Environmental and Safety Aspects," Lawrence Livermore National Laboratory, Livermore, CA, UCRL-JC-128089; *Fusion Technology* **33**(3), 298–340 (1998).

Latkowski, J. F., and Vujic, J. L., *Neutronics Issues and Inertial Fusion Energy: a Summary of Findings*, Lawrence Livermore National Laboratory, Livermore, CA, UCRL-JC-129625. Prepared for 1998 American Nuclear Society Annual Mtg, Nashville, TN, Jun 7, 1998.

Le Sage, G. P., Bennett, C. V., White, W. E., Landahl, E. C., Luhmann Jr., N. C., Hartemann, F. V., Ho, C. H., Layu, W. K., and Yang, T. T., "A High Brightness, X-Band Photoinjector for the Production of Coherent Synchrotron Radiation," Lawrence Livermore National Laboratory, Livermore, CA, UCRL-JC-130445; *Phys. Plasmas* **5**(5), SI:2048–2054 (1998).

Lowdermilk, W. H., *Abstracts of the 3rd Intl Conf on the Solid-State Lasers for Application to Inertial Confinement Fusion*, Lawrence Livermore National Laboratory, Livermore, CA, CONF-980653-ABSTS. Prepared for 3rd Intl Conf on the Solid-State Lasers for Application (SSLA) to Inertial Confinement Fusion (ICF), Monterey, CA, Jun 7, 1998.

M

- MacGowan, B. J., Berger, R. L., Cohen, B. I., Decker, C. D., Dixit, S., Glenzer, S. H., Hinkel, D. E., Kirkwood, R. K., Langdon, A. B., and Lasinski, B. F., *New Beam Smoothing Experiments at the Nova Laser*, Lawrence Livermore National Laboratory, Livermore, CA, UCRL-JC-130527 ABS. Prepared for 28th Annual Anomalous Absorption Conf, Bar Harbor, ME, Jun 14, 1998.
- Marinak, M. M., Glendinning, S. G., Wallace, R. J., Remington, B. A., Budil, K. S., Haan, S. W., Tipton, R. E., and Kilkenny, J. D., *Nonlinear Rayleigh–Taylor Evolution of a Three-Dimensional Multimode Perturbation*, Lawrence Livermore National Laboratory, Livermore, CA, UCRL-JC-129257; *Phys. Rev. Lett.* **80** (20), 4426–4429 (1998).
- Marinak, M. M., Haan, S. W., Dittrich, T. R., Tipton, R. E., and Zimmerman, G. B., *A Comparison of Three-Dimensional Multimode Hydrodynamic Instability Growth on Various National Ignition Facility Capsule Designs with HYDRA Simulations*, Lawrence Livermore National Laboratory, Livermore, CA, UCRL-JC-128862; *Phys. Plasmas* **5**(4), 1125–1132 (1998).
- Marshall, C. D., Beach, R. J., Bibeau, C., Ebberts, C. A., Emanuel, M. A., Honea, E. C., Krupke, W. F., Payne, S. A., Powell, H. T., Schaffers, K. I., Skidmore, J. A., and Sutton, S. B., *Next-Generation Laser for Inertial Confinement Fusion*, Lawrence Livermore National Laboratory, Livermore, CA, UCRL-JC-128084 Rev 2; *Laser Physics* **8**(3), 741–745 (1998).
- McEachern, R., and Alford, C., *Evaluation of Boron-Doped Beryllium as an Ablator for NIF Targets*, Lawrence Livermore National Laboratory, Livermore, CA, UCRL-JC-130530 ABS. Prepared for Target Fabrication Mtg '98, Jackson Hole, WY, Apr 19, 1998.
- McEachern, R., and Yamada, I., *Ion Cluster Beam Polishing for Inertial Confinement Fusion Target Capsules*, Lawrence Livermore National Laboratory, Livermore, CA, UCRL-JC-130683 ABS. Prepared for 12th Intl Conf on Ion Implantation Technology, Kyoto, Japan, Jun 22, 1998.
- McEachern, R., Matsuo, J., and Yamada, I., *Cluster Ion Beam Polishing for Inertial Confinement Fusion Target Capsules*, Lawrence Livermore National Laboratory, Livermore, CA, UCRL-JC-130683. Prepared for 12th Intl Conf on Ion Implantation Technology, Kyoto, Japan, Jun 22, 1998.
- Meier, W. R., *Systems Modeling and Analysis of Heavy Ion Drivers for Inertial Fusion Energy*, Lawrence Livermore National Laboratory, Livermore, CA, UCRL-JC-130954. Prepared for 1998 American Nuclear Society Annual Mtg, Nashville, TN, Jun 7, 1998.
- Michlitsch, K., *Laser-Induced Damage Initiated on the Surface of Particle Contaminated Fused Silica Optics at 1064 nm*, Lawrence Livermore National Laboratory, Livermore, CA, UCRL-LR-130583.
- Moir, R. W., *Inertial Fusion Energy Power Plants Based on Laser or Ion Beams*, Lawrence Livermore National Laboratory, Livermore, CA, UCRL-JC-129241. Prepared for 9th Intl Conf on Emerging Nuclear Energy Systems, Tel-Aviv, Israel, Jun 28, 1998.
- Montgomery, D. S., Afeyan, B. B., Cobble, J. A., Fernandez, J. C., Wilke, M. D., Glenzer, S. H., Kirkwood, R. K., MacGowan, B. J., Moody, J. D., Lindman, E. L., Munro, D. H., Wilde, B. H., Rose, H. A., Dubois, D. F., Bezzerides, B., and Vu, H. X., "Evidence of Plasma Fluctuations and Their Effect on the Growth of Stimulated Brillouin and Stimulated Raman Scattering in Laser Plasmas," *Phys. Plasmas* **5**(5), SI:1973–1980 (1998).
- Moody, J. D., MacGowan, B. J., Afeyan, B. B., Glenzer, S. H., Kirkwood, R. K., Pollaine, S. M., Schmitt, A. J., and Williams, E. A., *Measurements of Near Forward Scattered Laser Light in a Large ICF Plasma*, Lawrence Livermore National Laboratory, Livermore, CA, UCRL-JC-129774. Prepared for 12th Topical Conf on High-Temperature Plasma Diagnostics, Princeton, NJ, Jun 7, 1998.
- Moody, J. D., MacGowan, B. J., Afeyan, B. B., Glenzer, S. H., Kirkwood, R. K., Kruer, W. L., Pollaine, S. M., Schmitt, A. J., and Williams, E. A., *Measurements of Density Fluctuations and Beam-Spray in a Large Scalelength Nova Gasbag Plasma Using Near Forward Laser Scattering*, Lawrence Livermore National Laboratory, Livermore, CA, UCRL-JC-130334 ABS. Prepared for 28th Annual Anomalous Absorption Conf, Bar Harbor, ME, Jun 14, 1998.
- Moon, S. J., *Inner-Shell Photoionized X-Ray Lasers*, Lawrence Livermore National Laboratory, Livermore, CA, UCRL-LR-131000.
- Moran, M. J., *Fudge: a High-Bandwidth Fusion Diagnostic of the NIF*, Lawrence Livermore National Laboratory, Livermore, CA, UCRL-JC-129972. Prepared for 12th Topical Conf on High-Temperature Plasma Diagnostics, Princeton, NJ, Jun 7, 1998.
- Murphy, T. J., Wallace, J. M., Delamater, N. D., Barnes, C. B., Gobby, P., Hauer, A. A., Lindman, E. L., Magelssen, G., Moore, J. B., Oertel, J. A., Watt, R., Landen, O. L., Amendt, P., Cable, M., Decker, C., Hammel, B. A., Koch, J. A., Suter, L. J., Turner, R. E., Wallace, R. J., Marshall, F. J., Bradley, D., Craxton, R. S., Keck, R., Knauer, J. P., Kremens, R., and Schnittman, J. D., "Indirect Drive Experiments Utilizing Multiple Beam Cones in Cylindrical Hohlraums on OMEGA," *Phys. Plasmas* **5**(5), SI:1960–1965 (1998).

Murray, J., *ICF Quarterly Report 7* (3), Lawrence Livermore National Laboratory, Livermore, CA, UCRL-LR-105821-97-3 (1997).

P

Pennington, D. M., Perry, M. D., Britten, J. A., Brown, C. G., Herman, S., Miller, J. L., Stuart, B. C., Tietbohl, G., and Yanovsky, V., *Petawatt Class Laser System for Laser-Matter Interactions*, Lawrence Livermore National Laboratory, Livermore, CA, UCRL-JC-130872 ABS. Prepared for *3rd Intl Conf on the Solid-State Lasers for Application (SSLA) to Inertial Confinement Fusion (ICF)*, Monterey, CA, Jun 7, 1998.

Phillips, T. W., Cable, M. D., Cowan, T. E., Hatchett, S. P., Henry, E. A., Key, M. H., Perry, M. D., Sangster, T. C., and Stoyer, M. A., *Diagnosing Hot Electron Production by Short Pulse, High Intensity Lasers Using Photonuclear Reactions*, Lawrence Livermore National Laboratory, Livermore, CA, UCRL-JC-129813. Prepared for *12th Topical Conf on High-Temperature Plasma Diagnostics*, Princeton, NJ, Jun 7, 1998.

Pollaine, S. M., Glendinning, S. G., Amendt, P., Delamater, N. D., Klare, K. A., Murphy, T. J., Oertel, J. A., Wallace, J. M., Bradley, D., and Craxton, S., *Symmetry Measurements of Tetrahedral Hohlraums*, Lawrence Livermore National Laboratory, Livermore, CA, UCRL-JC-130676 ABS. Prepared for *28th Annual Anomalous Absorption Conf*, Bar Harbor, ME, Jun 14, 1998.

Powell, H. T., Paisner, J. A., and Payne, S. A., *Possible Driver Path from the National Ignition Facility to Inertial Fusion Energy*, Lawrence Livermore National Laboratory, Livermore, CA, UCRL-JC-130616 ABS. Prepared for *17th Intl Atomic Energy Agency Fusion Energy Conf*, Yokohama, Japan, Oct 19, 1998.

R

Rashkovich, L. N., *Effect of pH on the Growth of KDP*, Lawrence Livermore National Laboratory, Livermore, CA, UCRL-CR-122742-1, May 19, 1998.

Rothenberg, J. E., *Polarization Smoothing for Inertial Confinement Fusion with Megajoule Class Lasers*, Lawrence Livermore National Laboratory, Livermore, CA, UCRL-JC-130609 ABS. Prepared for *28th Annual Anomalous Absorption Conf*, Bar Harbor, ME, Jun 14, 1998.

Rubenchik, A. M., Feit, M. D., Perry, M. D., and Larsen, J. T., "Numerical Simulation of Ultra-Short Laser Pulse Energy Deposition and Bulk Transport for Material Processing," Lawrence Livermore National Laboratory, Livermore, CA, UCRL-JC-127279; *Appl. Surface Sci.* **129**, 193-198 (1998).

Ryutov, D., Drake, R. P., Kane, J., Liang, E., Remington, B. A., and Wood-Vasey, W. M., *Similarity Criteria for the Laboratory Simulation of Supernova Hydrodynamics*, Lawrence Livermore National Laboratory, Livermore, CA, UCRL-JC-130956 DR. Submitted to *Astrophys. J.*

S

Shestakov, A. I., and Milovich, J. L., *Parallelization of an Unstructured Grid, Hydrodynamic-Diffusion Code*, Lawrence Livermore National Laboratory, Livermore, CA, UCRL-JC-130862. Prepared for *Fifth Intl Symp on Solving Irregularly Structured Problems in Parallel*, Berkeley, CA, Aug 9, 1998.

Shestakov, A. I., and Milovich, J. L., *Parallelization of ICF3D, an Unstructured Grid, Hydrodynamic-Diffusion Code*, Lawrence Livermore National Laboratory, Livermore, CA, UCRL-JC-130699 ABS. Prepared for *Fifth Intl Symp on Solving Irregularly Structured Problems in Parallel*, Berkeley, CA, Aug 9, 1998.

Shestakov, A. I., *Simulation of Two Point Explosion/Heat Conduction Problems with a Hydrodynamic-Diffusion Code*, Lawrence Livermore National Laboratory, Livermore, CA, UCRL-JC-130700. Submitted to *Physics of Fluids*.

Shestakov, A., Milovich, J. L., and Kershaw, D. S., *Parallelization of a 3D, Unstructured Grid, Hydrodynamic-Diffusion Code*, Lawrence Livermore National Laboratory, Livermore, CA, UCRL-JC-130988. Submitted to *J. of Scientific Computing*.

Solarz, R. W., Emanuel, M. A., Skidmore, J. A., Freitas, B. L., and Krupke, W. F., "Trends in Packaging of High Power Semiconductor Laser Bars," Lawrence Livermore National Laboratory, Livermore, CA, UCRL-JC-128083; *Laser Physics* **8**(3), 737-740 (1998).

Still, C. H., Berger, R. L., Langdon, A. B., Williams, E. A., and Langer, S. H., *Large-Scale Filamentation Simulations with YF3D*, Lawrence Livermore National Laboratory, Livermore, CA, UCRL-JC-130346 ABS. Prepared for *28th Annual Anomalous Absorption Conf*, Bar Harbor, ME, Jun 14, 1998.

Suter, L. J., Dattalo, E., Dague, N., Decker, C. D., Glenzer, S., Jadaud, J. P., Landen, O. L., Monteil, M.-C., Turner, R. E., and Blain, M. A., *Advances in Diagnosing, Understanding and Controlling X-Radiation Flux in ICF Hohlraums*, Lawrence Livermore National Laboratory, Livermore, CA, UCRL-JC-130581 ABS. Prepared for *28th Annual Anomalous Absorption Conf*, Bar Harbor, ME, Jun 14, 1998.

Suter, L. J., Landen, O. L., and Cohen, D. H., *Fluorescence Based Visualization/Diagnosis of Laser Driven Radiation-Hydrodynamics Experiments*, Lawrence Livermore National Laboratory, Livermore, CA, UCRL-JC-130580 ABS. Prepared for 28th Annual Anomalous Absorption Conf, Bar Harbor, ME, Jun 14, 1998.

Suter, L. J., Landen, O. L., Koch, J. I., and Cohen, D., *Prospects for Fluorescence Based Imaging/Visualization of Hydrodynamic Systems on the National Ignition Facility*, Lawrence Livermore National Laboratory, Livermore, CA, UCRL-JC-130980. Prepared for 12th Topical Conf on High-Temperature Plasma Diagnostics, Princeton, NJ, Jun 7, 1998.

T

Tabak, M., and Callahan-Miller, D., "Design of a Distributed Radiator Target for Inertial Fusion Driven from Two Sides with Heavy Ion Beams," Lawrence Livermore National Laboratory, Livermore, CA, UCRL-JC-128366; *Phys. Plasmas* 5(5), SI:1895–1900 (1998).

Tabak, M., Callahan-Miller, D., Ho, D. D.-M., and Zimmerman, G. B., "Design of a Distributed Radiator Target for Inertial Fusion Driven from Two Sides with Heavy Ion Beams," Lawrence Livermore National Laboratory, Livermore, CA, UCRL-JC-128366; *Nuclear Fusion* 38(4), 509–513 (1998).

Turner, R. E., Amendt, P. A., Glendinning, S. G., Kalantar, D. H., Landen, O. L., Wallace, R. J., Bradley, D., Morse, S., Pien, G., and Seka, W., *X-Ray Drive Symmetry for Indirectly Driven High Convergence Targets on OMEGA*, Lawrence Livermore National Laboratory, Livermore, CA, UCRL-JC-130337 ABS. Prepared for 28th Annual Anomalous Absorption Conf, Bar Harbor, ME, Jun 14, 1998.

Turner, R. E., Landen, O. L., Bell, P., Costa, R., and Hargrove, D., *Achromatically Filtered Diamond Photoconductive Detectors for High Power Soft X-Ray Flux Measurements*, Lawrence Livermore National Laboratory, Livermore, CA, UCRL-JC-129713. Prepared for 12th Topical Conf on High-Temperature Plasma Diagnostics, Princeton, NJ, Jun 7, 1998.

W

Weber, S. V., Colvin, J. D., Kalantar, D. H., Mikaelian, K. O., Remington, B. A., Wiley, L. G., Failor, B., Hauer, A., Kane, J. O., and Meyers, M. A., *Laser-Driven Rayleigh–Taylor Instability Experiments for Materials with Strength*, Lawrence Livermore National Laboratory, Livermore, CA, UCRL-JC-130531 ABS. Prepared for 28th Annual Anomalous Absorption Conf, Bar Harbor, ME, Jun 14, 1998.

Wharton, K. B., Kirkwood, R. K., Glenzer, S. H., Estabrook, K. G., Afeyan, B. B., Cohen, B. I., Moody, J. D., and Joshi, C., *Observation of Energy Transfer between Identical-Frequency Laser Beams in Flowing Plasmas*, Lawrence Livermore National Laboratory, Livermore, CA, UCRL-JC-129856 Rev 1; *Phys. Rev. Lett.* 81 (11), 2248–2251 (1998).

Wilks, S. C., Kruer, W. L., Cowan, T., Hatchett, S., Key, M., Langdon, A. B., Perry, M. D., Tabak, M., and Wharton, K., *Absorption of Ultra-Short, Ultra-Intense Laser Light by Solids and Over-Dense Plasmas*, Lawrence Livermore National Laboratory, Livermore, CA, UCRL-JC-130347 ABS. Prepared for 28th Annual Anomalous Absorption Conf, Bar Harbor, ME, Jun 14, 1998.

Wilks, S. C., Kruer, W. L., Cowan, T., Hatchett, S., Key, M., Langdon, A. B., Perry, M. D., Tabak, M., and Wharton, K., *Absorption of Ultra-Short, Ultra-Intense Laser Light by Solids and Over-Dense Plasmas*, Lawrence Livermore National Laboratory, Livermore, CA, UCRL-JC-130347 ABS Rev. Prepared for 9th Conf on Laser Optics, St. Petersburg, Russia, Jun 22, 1998.

Williams, E. A., Hinkel, D. E., Berger, R. L., Langdon, A. B., and Still, C. H., *Flow Induced Bending of Laser Beams Smoothed by FM-SSD*, Lawrence Livermore National Laboratory, Livermore, CA, UCRL-JC-130348 ABS. Prepared for 28th Annual Anomalous Absorption Conf, Bar Harbor, ME, Jun 14, 1998.

Wilson, D. C., Bradley, P. A., Hoffman, N. M., Swenson, F. J., Smitherman, D. P., Chrien, R. E., Margevicius, R. W., Thoma, D. J., Foreman, L. R., Hoffer, J. K., Goldman, S. R., Caldwell, S. E., Dittrich, T. R., Haan, S. W., Marinak, M. M., Pollaine, S. M., and Sanchez, J. J., "The Development and Advantages of Beryllium Capsules for the National Ignition Facility," *Phys. Plasmas* 5(5), SI1953–1959 (1998).

Z

Zaitseva, N. P., Atherton, L. J., De Yoreo, J. J., Carman, M. L., Torres, R., and Yan, M., *Growth and Optical Quality of Large (55 cm) KDP and DKDP Crystals*, Lawrence Livermore National Laboratory, Livermore, CA, UCRL-JC-130959 ABS. Prepared for *16th Intl Conf on Coherent and Nonlinear Optics 1998*, Moscow, Russia, Jun 29, 1998.

Zaitseva, N. P., *Large KDP and DKDP Crystals: Recent Results on Growth and Optical Quality*, Lawrence Livermore National Laboratory, Livermore, CA, UCRL-JC-130958 ABS. Prepared for *9th Conf of Laser Optics*, St. Petersburg, Russia, Jun 22, 1998.

Ze, F., Landen, O. L., Bell, P. M., Turner, R. E., Tutt, T., Alvarez, S. S., and Costa, R. L., *Investigation of X-Ray Quantum Efficiencies in Multilayered Photocathodes for Micro Channel Plate (MCP) Applications*, Lawrence Livermore National Laboratory, Livermore, CA, UCRL-JC-129620. Prepared for *12th Topical Conf on High Temperature Plasma Diagnostics*, Princeton, NJ, Jun 7, 1998.